

University of Windsor

Scholarship at UWindor

Electronic Theses and Dissertations

Theses, Dissertations, and Major Papers

2011

INTERFACE PHENOMENA IN PROTON EXCHANGE MEMBRANE FUEL CELLS

Simo Kang
University of Windsor

Follow this and additional works at: <https://scholar.uwindsor.ca/etd>

Recommended Citation

Kang, Simo, "INTERFACE PHENOMENA IN PROTON EXCHANGE MEMBRANE FUEL CELLS" (2011).
Electronic Theses and Dissertations. 5389.
<https://scholar.uwindsor.ca/etd/5389>

This online database contains the full-text of PhD dissertations and Masters' theses of University of Windsor students from 1954 forward. These documents are made available for personal study and research purposes only, in accordance with the Canadian Copyright Act and the Creative Commons license—CC BY-NC-ND (Attribution, Non-Commercial, No Derivative Works). Under this license, works must always be attributed to the copyright holder (original author), cannot be used for any commercial purposes, and may not be altered. Any other use would require the permission of the copyright holder. Students may inquire about withdrawing their dissertation and/or thesis from this database. For additional inquiries, please contact the repository administrator via email (scholarship@uwindsor.ca) or by telephone at 519-253-3000ext. 3208.

**INTERFACE PHENOMENA IN PROTON EXCHANGE MEMBRANE
FUEL CELLS**

by
Simo Kang

A Thesis
Submitted to the Faculty of Graduate Studies
Through
Mechanical Engineering
in Partial Fulfillment of the Requirements for
the Degree of Master of Applied Science at the
University of Windsor

Windsor, Ontario, Canada

2011

© 2011 Simo Kang

Interface phenomena in proton exchange membrane fuel cells

By
Simo Kang

APPROVED BY:

Dr. Xiaobu Yuan, Outside Reader
School of Computer Science

Dr. Andrzej Sobiesiak, Program Reader
Department of Mechanical, Automotive & Materials Engineering

Dr. Biao Zhou, Advisor
Department of Mechanical, Automotive & Materials Engineering

Dr. Jennifer Johrendt, Chair of Defense
Department of Mechanical, Automotive & Materials Engineering

Declaration of Co-Authorship / Previous Publication

I. Co-Authorship Declaration

I hereby declare that this thesis incorporates material that is result of joint research, as follows:

This thesis also incorporates the outcome of a joint research undertaken in collaboration with Chin-Hsiang Cheng, Huan-Ruei Shiu and Chun-I Lee and under the supervision of professor Biao Zhou. The collaboration is covered in Chapter 4 of the thesis. In all cases, the key ideas, primary contributions, experimental designs, data analysis and interpretation, were performed by the author, and the contribution of co-authors was primarily through the provision of financial support and participate in the discussion of modeling results.

I am aware of the University of Windsor Senate Policy on Authorship and I certify that I have properly acknowledged the contribution of other researchers to my thesis, and have obtained written permission from each of the co-author(s) to include the above material(s) in my thesis.

I certify that, with the above qualification, this thesis, and the research to which it refers, is the product of my own work.

II. Declaration of Previous Publication

This thesis includes one original paper that has been previously published for publication in peer reviewed journals, as follows:

Thesis Chapter	Publication title/full citation	Publication status*
Chapter 4	<i>Liquid water flooding in a proton exchange membrane fuel cell cathode with an interdigitated design, S Kang, B Zhou, C Cheng, H Shiu, C Lee, Liquid water flooding in a proton exchange membrane fuel cell cathode with an interdigitated design, Int. J. Energy Res. (2011), DOI: 10.1002/er.1858</i>	<i>Published</i>

I certify that I have obtained a written permission from the copyright owner(s) to include the above published material(s) in my thesis. I certify that the above material describes work completed during my registration as graduate student at the University of Windsor.

I declare that, to the best of my knowledge, my thesis does not infringe upon anyone's copyright nor violate any proprietary rights and that any ideas, techniques, quotations, or any other material from the work of other people included in my thesis, published or otherwise, are fully acknowledged in accordance with the standard referencing practices. Furthermore, to the extent that I have included copyrighted material that surpasses the bounds of fair dealing within the meaning of the Canada Copyright Act, I certify that I have obtained a written permission from the copyright owner(s) to include such material(s) in my thesis.

I declare that this is a true copy of my thesis, including any final revisions, as approved by my thesis committee and the Graduate Studies office, and that this thesis has not been submitted for a higher degree to any other University or Institution.

Abstract

Two phase flow phenomena is a critical issue in Proton Exchange Membrane Fuel Cell (PEMFC) development. Two main classes of PEMFCs, direct hydrogen fuel cell (DHFC) and direct methanol fuel cell (DMFC) have similar problem caused by two phase flow. Both the water in cathode (DHFC and DMFC) and CO₂ in anode (DMFC) cannot be removed efficiently will hinder the process of the chemical reaction of the fuel cell and interfere with the performance. To optimize the performance of a PEMFC, it is important to understand the gas-liquid interaction and an accurate two-phase modeling needs be develop for this purpose.

In this thesis, Volume of Fluid (VOF) method has been introduced into PEMFC modeling conducted by commercial computational fluid dynamics (CFD) software package FLUENT 6.3.26. User defined function (UDF) is adopted to calculated the pressure and liquid or gas amount. Different geometries and simplified simulation domain designs have been developed.

Dedication

To my parents Jing Huang and Shien Kang.

Acknowledgements

I would like to express my deepest gratitude to my supervisors, Dr. Biao Zhou, for the guidance provided throughout the course of my research, his constructive criticism, many valuable suggestions and continuous support.

My thanks also go to Dr. Xiaobu Yuan and Dr. Andrzej Sobiesiak for all their help and support to develop this thesis.

I specially thank all the members and previous members of the Dr. Zhou's laboratory with whom I had numerous fruitful discussions, in particular Xichen Wang.

I specially thank those who provided kindly and effective help among faculty, staff, and students at the University of Windsor.

Finally, I take the opportunity to thank my parents Shien Kang and Jing Huang for all their love and support. I would not have been able to complete this work without their sustained encouragement.

Table of contents

Declaration of Co-Authorship / Previous Publication	iii
Abstract	v
Dedication	vi
Acknowledgements	vii
List of Tables	xi
List of Figures	xii
Nomenclature	xiv
Chapter 1 Introduction	1
1.1 Fuel cells.....	1
1.1.1 General descriptions.....	1
1.1.2 Classification of fuel cells.....	1
1.2 PEM fuel cells.....	2
1.2.1 PEMFCs Principle.....	2
1.2.2 Advantages.....	4
1.2.3 Challenges.....	5
1.3 Objectives.....	6
Chapter 2 Literature review	7
2.1 Review of PEMFC numerical simulation.....	7
2.1.1 Review of DHFC numerical simulation.....	7
2.1.2 Review of DMFC numerical simulation.....	8
2.2 Review of PEMFC experiment visualization.....	9
2.2.1 Review of DHFC experiment visualization.....	9
2.2.2 Review of DMFC experiment visualization.....	10
Chapter 3 Numerical model setup	11
3.1 Governing equations.....	11
3.2 Interface tracking algorithm.....	12
3.2.1 Interface reconstruction algorithm.....	13
3.2.2 Fluid advection algorithm.....	14

3.2.3	Implementation of surface tension	14
Chapter 4	Interface phenomena in a DHFC cathode with an interdigitated design	16
4.1	Numerical model description.....	16
4.2	Results and discussion	17
4.2.1	Validation with liquid water distribution inside the fuel cell cathode	17
4.2.2	General liquid water flooding process in the interdigitated cathode	19
4.2.3	Liquid water flooding behavior	20
4.2.4	Liquid water outflow process through the outlet channel	33
4.2.5	Liquid water avalanche around the top-right corner.....	37
4.2.6	Amount of liquid water over time and the flooding phases.....	39
4.3	Summary.....	41
Chapter 5	Numerical model validations in DMFC anode with a serpentine channel	42
5.1	Numerical model description.....	42
5.2	Validation with break-up process at T-junction.....	43
5.2.1	Boundary conditions and mesh setup	43
5.2.2	Comparison of numerical simulation and experimental visualization with break-up process at T-junction	43
5.2.3	Velocity field of break-up process.....	46
5.2.4	Pressure fields	47
5.3	Effects of surface tension and liquid viscosity.....	49
5.3.1	Effects of surface tension	49
5.3.2	Effects of viscosity	51
5.4	Summary.....	51
Chapter 6	Interface phenomenon in a DMFC anode with a parallel design.....	53
6.1	Computational geometry	53
6.2	Boundary conditions and mesh setup	53
6.3	Results and discussion	54
6.3.1	Gas CO ₂ behavior inside DMFC anode with parallel design	54
6.3.2	General distribution of CO ₂ in the porous layer	56
6.3.3	CO ₂ emerging process and the vortexes phenomenon in the channels.....	57
6.3.4	CO ₂ volume amount inside computational domains	60
6.3.5	Pressure drop versus time.....	64
6.4	Summary.....	66

Chapter 7	Interface phenomena in DMFC anode with innovative GDL-1 and static contact angle	67
7.1	Computational domain	67
7.2	Fluid properties and boundary conditions.....	68
7.3	Mesh setup.....	69
7.4	Results and discussion	69
7.4.1	Validation with a practical DMFC anode	69
7.4.2	General CO ₂ flooding process.....	70
7.4.3	Effect of the gravity.....	75
7.4.4	The CO ₂ bubble floating in GDL.....	77
7.4.5	The emerging process of CO ₂ in channels.....	80
7.5	Summary.....	80
Chapter 8	Interface phenomena in DMFC anode with innovative GDL-2 and dynamic contact angle	82
8.1	Computational domain	82
8.2	Boundary condition	82
8.3	Methodology of implementation of dynamic contact angle	83
8.4	Results and discussion	84
8.4.1	Experiment validation of DMFC anode with a carbon cloth MEA.....	84
8.4.2	CO ₂ behavior inside parallel DMFC anode with and without dynamic contact angle effect	85
8.4.3	General process of emerging process of gas bubbles behavior in porous layer with static contact angle and dynamic contact angle.....	86
8.4.4	CO ₂ volume amount inside computational domain.....	89
8.4.5	Pressure drop of computational domain.....	90
8.5	Summary.....	91
Chapter 9	Conclusions	92
References		93
VITA AUCTORIS		97

List of Tables

Table 1-1 Comparison of DHFC and DMFC [1 – 3].....	4
Table 5-1 Effect of liquid viscosity	51
Table 6-1 Parameters and properties used in the model	54
Table 7-1 Parameters and properties used in the model	68
Table 8-1 Parameters and properties used in the model	83

List of Figures

Fig. 1-1 PEMFC structure	3
Fig. 3-1 Computational domain.....	13
Fig. 4-1 Computational domain and definition of the components	17
Fig. 4-2 Comparison of numerical simulation and experimental visualization.....	18
Fig. 4-3 The general process of water behavior shown with 3D isosurfaces	20
Fig. 4-4 Water volume fraction and velocity vector in the selected cross section in the porous layer ($Z = 0.15$ mm) and the water volume fraction and velocity vector in the selected cross section in the flow channels ($Z = 0.45$ mm).....	22
Fig. 4-5 Water volume fraction and velocity vectors in the cross sections ($X = 12$ mm and $X = 15$ mm) at $t = 0.419$ s.....	29
Fig. 4-6 Water volume fraction and velocity vectors in the cross sections ($Y = 6$ mm, $Y = 12$ mm, and $Y = 18$ mm) at (2) $t = 0.006$ s, (3) $t = 0.015$ s, (4) $t = 0.091$ s, (5) $t = 0.156$ s,	32
Fig. 4-7 Water outflow process from the outlet channel shown from the XY view at (1) $t = 0.753$ s, (2) $t = 1.367$ s, (3) $t = 1.383$ s	34
Fig. 4-8 Liquid water distribution in the 3D outlet channel and in the cross sections at (1) $t = 0.753$ s, (2) $t = 1.367$ s, (3) $t = 1.383$ s, (4) $t = 1.388$ s, (5) $t = 1.391$ s, (6) $t = 1.393$ s	37
Fig. 4-9 The avalanche process and the draining process shown from the XY view at (1) $t = 1.138$ s, (2) $t = 1.155$ s, (3) $t = 1.178$ s, (4) $t = 1.277$ s.....	38
Fig. 4-10 Variation curve of the amount of water as a function of time in the entire domain.....	40
Fig. 5-1 Computational domain of serpentine channel.....	42
Fig. 5-2 Validation with bubble generated in T-junction	44
Fig. 5-3 Gas volume fraction and velocity vector in T-junction.....	46
Fig. 5-4 Volume fraction of Gas and Pressure distribution in serpentine channel.....	48
Fig. 5-5 Volume fraction of gas and pressure drop with vector of first two inverted U shape channels.....	49
Fig. 5-6 Gaseous volume fraction of two cases with different surface tension	50
Fig. 6-1 Computational geometry.....	53
Fig. 6-2 General process of gas CO_2 flooding.....	55
Fig. 6-3 CO_2 distribution at $Z = -0.00015$ m	57
Fig. 6-4 General process by which liquid water emerges into the channels.....	59
Fig. 6-5 CO_2 volume amount in different part of the computational domain.....	60
Fig. 6-6 Pressure of each sub-domain inlet and outlet	65
Fig. 7-1 Computational domain of a DMFC anode with parallel design with an	

innovation GDL.....	67
Fig. 7-2 Innovation gas diffusion layer (GDL).....	68
Fig. 7-3 Comparison of numerical simulation and experimental visualization.....	69
Fig. 7-4 The general process of gas behavior shown with 3D isosurfaces (first column I) and selected cross-section (second column II), and the part of the cross-section has been enlarged to see the vector	74
Fig. 7-5 Comparison of emerging process of gas in two cases with same boundary condition but different gravity orientation:.....	76
Fig. 7-6 Gas volume fraction and velocity vector in the selected cross section in the porous layer	78
Fig. 7-7 Gas volume fraction and velocity vector in the selected cross section in the porous layer	80
Fig. 8-1 Gas diffusion layer built in this model.....	82
Fig. 8-2 Validation of simulation results with visualization study results of DMFC anode with a parallel design by Liao et al. [58]	84
Fig. 8-3 General process of gas CO ₂ flooding process with and without dynamic contact angle considered	86
Fig. 8-4 Comparison of emerging process of CO ₂ of two cases with static contact angle (left column) and with dynamic contact angle (right column) on cross-section of $Z = - 0.00005$ m in GDL.....	88
Fig. 8-5 The contact angle of wall around the GDL and CL in the case with DCA	88
Fig. 8-6 Gas CO ₂ volume amount inside each sub-domain.....	90
Fig. 8-7 Pressure at Methanol inlet and anode outlet	90

Nomenclature

ρ	Density ($\text{kg}\cdot\text{m}^3$)
ε	Porosity
\mathbf{u}	Velocity vector ($\text{m}\cdot\text{s}^{-1}$)
S	Source term
α	Phase volume fraction
μ	Dynamic viscosity ($\text{Pa}\cdot\text{s}$)
σ	Surface tension ($\text{N}\cdot\text{m}^{-1}$)
κ	Surface curvature
K	Permeability (m^2)
n	Normal vector
θ_D	Dynamic contact angle ($^\circ$)
θ_e	Contact angle in equilibrium ($^\circ$)
Ca	Capillary number
f_{Hoff}	Hoffmann function
f_{Hoff}^{-1}	Reversed Hoffmann function
f_{Hoff}^*	Improved Hoffmann function
x	Shift factor
Vel	Contact line velocity ($\text{m}\cdot\text{s}^{-1}$)

Subscripts

1	Liquid phase
2	Secondary phase

Chapter 1 Introduction

1.1 Fuel cells

1.1.1 General descriptions

A fuel cell is an energy conversion device that transforms the chemical energy stored in a fuel into electrical energy through an exothermic electrochemical reaction. Unlike a battery, a fuel cell does not deplete or require recharging. It generates electricity continuously as long as fuel and oxidant are supplied. A fuel cell usually contains two electrodes (an anode and a cathode) separated by an electrolyte. Two couple half reactions occurred at the electrodes: an oxidation reaction liberates electrons at the cathode side; a reduction reaction consumes electrons at the anode side [1, 2].

Compared with combustion engines, fuel cells are much more efficiently and environmentally friendly without NO_x , SO_x and particulate emissions. As a result, fuel cells are considered as potential alternatives to the fossil fuels. Meanwhile, they offer higher potential power density compare with battery and fast response to charge of load. Furthermore, fuel cells present even more intriguing advantages, such as mechanical simplicity, modularity, lower noise level, quick start-up.

However, fuel cells are not perfect with some serious problems, for example, highly cost, low power density, storage and availability of the fuels, operational temperature. Fuel cells cannot be extensively applied without approaches to these problems [1].

1.1.2 Classification of fuel cells

A number of fuel cell types have been developed. The most common classification of fuel cells is according to the electrolyte material utilized. They include (1) proton exchange membrane fuel cell (PEMFC); (2) phosphoric acid fuel cell (PAFC); (3) alkaline fuel cell (AFC); (4) molten carbonate fuel cell (MCFC); (5) solid-oxide fuel cell (SOFC). Besides, additional sub-classification could be demonstrated based on operation temperature range or different fuels utilized. For example, both direct hydrogen proton exchange membrane fuel cells and direct methanol fuel cell (DMFC) included in PEMFC. Each type of fuel cells has its unique advantage for certain application area. Table 1.1 shows the performance characteristics and applications of the main groups of fuel cells [1 - 3]. The approximate operating

temperature for each type of fuel cells is different, ranging from 30 – 100 °C for PEMFC, 160 – 220 °C for PAFC, 60 – 250 °C for AFC, 600 – 800 °C for MCFC, and 600 – 1000 °C for SOFC.

1.2 PEM fuel cells

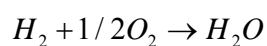
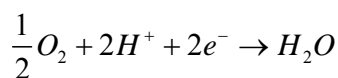
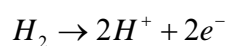
1.2.1 PEMFCs Principle

The PEMFC is named because of the special proton-exchange membrane that it uses as its electrolyte. It can be sub-classified by the fuel it used. The most common fuel for the PEMFCs is hydrogen. Usually, the hydrogen needs to be produced from various fuels through a reforming process, such as methane, methanol, and gasoline. In recent years, using methanol as a fuel which could directly consumed in fuel cells without the deforming process also present intriguing advantages. This kind of fuel cells is named direct methanol fuel cell (DMFC).

Figure 1.1 shows the basic component of a PEM fuel cell. A proton conducting membrane is sandwiched between the anode and the cathode side. In each side, it include anode or cathode catalysts layer (CL), gas diffusion layers (GDLs), and channels in a bipolar plate. In a direct hydrogen PEM fuel cell, hydrogen which introduced through the channels cross the GDL and get the anode catalyst layer. With the presence of catalyst, the hydrogen dissociate into protons and electrons. The membrane is attached by both anode and cathode CLs. While the electrons generated in the anode CLs, they are unable to go through the membrane as the protons do. As a result, current generated [4].

As introduced above, the PEMFC could be sub-classified according to the fuel used. One of main type of PEMFC is hydrogen proton exchange membrane fuel cell. Usually it is called PEMFC directly because of the long developing history before other types of PEMFC. However, in this thesis, relative directly methanol fuel cell (DMFC), hydrogen PEMFC is called directly hydrogen fuel cell (DHFC) to distinguish.

The two major reactions occurring in a DHFC are hydrogen oxidation reaction at anode and oxygen reduction reaction at cathode as followed:



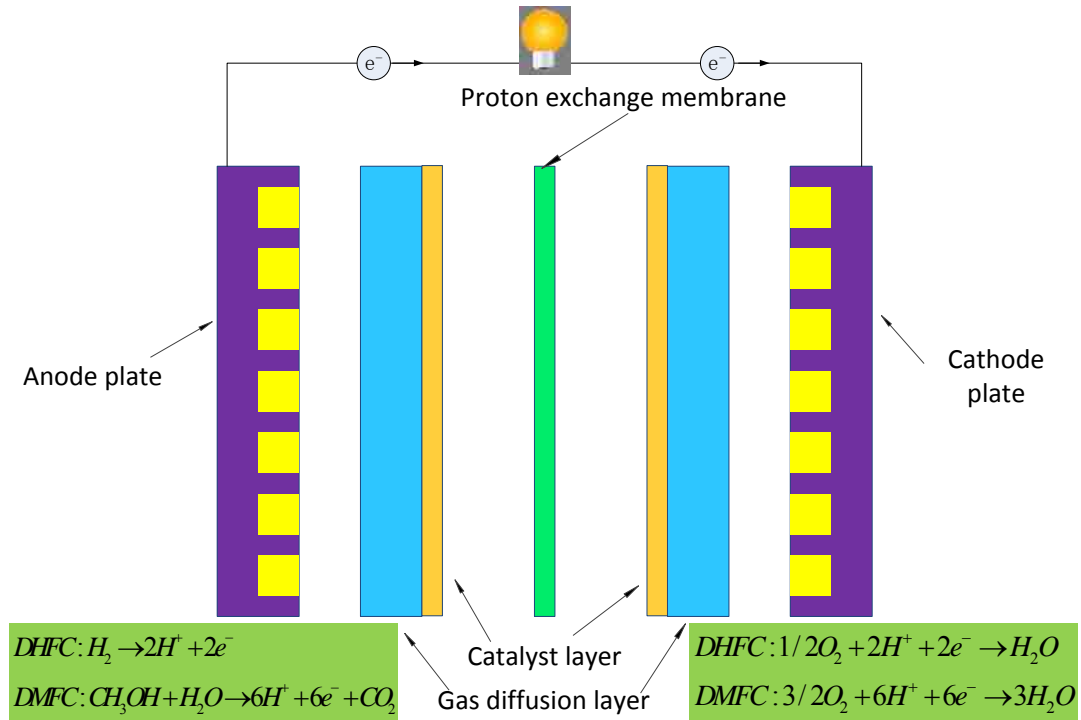
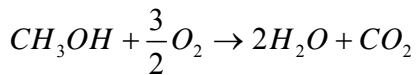
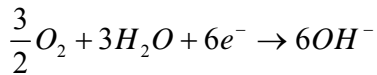
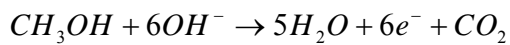
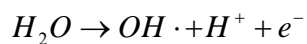


Fig. 1-1 PEMFC structure

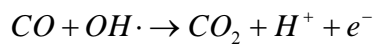
The fuel in the DMFC is changed to methanol, and the cell reactions are changed to:



Today, the catalyst used for both anode and cathode reaction is platinum. Adopting platinum could reduce the loss of cell voltage potential with methanol oxidize in cathode. However, this catalyst is not enough for the reduction of oxygen, which results low efficient on lessen of methanol crossover. During the methanol oxidation reaction, carbon dioxide (CO) is also formed and adsorbed onto the catalyst. This will affect the performance of the cell by reduce surface area. Meanwhile, other components in the catalyst layer, such as ruthenium or gold tends to improve this performance because these catalysts oxidize water to yield OH radicals:



Then the OH species could react with CO and generate CO₂.



1.2.2 Advantages

First, lower operating temperature makes PEMFCs easier to operate. They are usually could rapid start-up and change the power output.

Second, solid electrolyte results less expensive to manufacture. Different with liquid electrolyte, solid part helps sealing the anode and cathode fluid (liquid and gas). Also, because of the solid electrolyte do not have the problems like orientation and corrosion, they make the PEMFCs a longer life.

Table 1-1 Comparison of DHFC and DMFC [1 - 3]

	DHFC	DMFC
Electrolyte	Proton exchange membrane	Proton exchange membrane
Fuels	Hydrogen	Methanol and water
Operating Temperature (°C)	30 - 100	30 - 100
Charge carrier	H ⁺	H ⁺
Catalyst	Pt	Pt/Ru
Operation pressure (atm)	1 - 3	1 (Anode) 1 - 3 (Cathode)
Advantages	Low-temperature operation; High efficiency; Relatively rapid start-up; Zero-emissions; High H ₂ power-to-weight ratio; Hydrogen can be produced at either large or small facilities.	Low-temperature operation; High efficiency; Relatively rapid start-up; Zero-emissions; High energy density of MeOH; Ease of produce and transport of MeOH.
Disadvantages	Water management; Expensive catalyst; Durability of components not yet sufficient; Poor-quality waste heat; Intolerance to CO; Thermal management.	CO ₂ bubble management in anode; Water management in cathode; Expensive catalyst; Durability of components not yet sufficient; Poor-quality waste heat; Intolerance to CO; Thermal management.
Application	Stationary applications Portable Automotive	Portable APU (Auxiliary Power Unit)

Third, the PEMFCs brought no air-pollution with zero-emission. Because of the only product are water and heat, the DHFCs are considered to produce drinking water.

DHFC is more matured with longer history and more research concern because of its higher power-to-weight ratio. Nevertheless, for the application of small and portable devices, DMFCs showed their merit. Compare with hydrogen, methanol is much more easy to produced and transport and could be utilized in the fuel cells without passing through an expensive reformer. Although the power-to-weight ratio of methanol is only 1/5 of hydrogen, methanol could offer 4 times power density per volume under 250 atm because it is liquid.

1.2.3 Challenges

DHFC

During the commercialize progress of DHFC, there are still some serious technical issues for the fuel cell researchers: (1) two-phase flow management in cathode side (2) management of heat, (3) durability, and (4) freeze-thaw cycling and frozen-start capability.

Water management is a critical challenge for high-performance DHFCs. In the cathode side of DHFCs, oxygen reacts with protons transferred via a membrane and with electrons through an external circuit from the anode to generate water and release heat in the catalyst layer. Of the designs available in the literature [5], liquid water flooding typically occurs if the operating condition deviates from its nominal condition. Deviations in the operating conditions are unavoidable for practical engineering applications of DHFCs, such as fuel cell powered vehicles. Therefore, to commercialize DHFCs, the liquid water flooding process must be understood and properly resolved.

DMFC

Although DMFC has been recognized as one of the most promising portable fuel cell which could be commercialized, there is also some technological problem during the development of DMFC: (1) two-phase flow management in the anode and cathode [6, 7], (2) methanol crossover [8, 9], (3) poor catalyst activity, (4) high catalyst loading, (5) management of heat [10], (6) relatively low power density [11], (7) management of water [12-13], (8) slow reaction kinetics of methanol electro-oxidation.

With similar principle of DHFC, CO₂ produced by the chemical reaction at the anode and

should be removed from the anode outlet as efficiently as possible. Otherwise the bubble of CO_2 choked in the anode channel would increase the gradient of methanol concentration along the channel and hinder the continuous reaction. As a result, gas management in the anode side is a critical challenge for high-performance DMFC.

1.3 Objectives

In conclusion of the introduction above, it is easy to realize the critical problem for both DHFC and DMFC—two-phase flow phenomena. The interface phenomenon of liquid-gas is the central topic of the thesis.

Various general PEMFC model (both for DHFC and DMFC) are developed to investigate the interface phenomenon in PEMFC anode and cathode with various flow field. The volume of fluid (VOF) algorithm is adopted to track the interface. The accelerated model is used to get the effect of both two phase interaction and accumulation of fluid. Different porous layers were adopted to explore the best method to simplified simulation GDL and CL.

Through these numerical studies, the objectives could be summarized as follows:

- Gas-liquid interface tracking through multi-phase, three-dimensional PEMFC model;
- Tracking the distribution of liquid water in DHFC cathode with an interdigitated design;
- Tracking the distribution of CO_2 in DMFC anode with a parallel design;
- Tracking the liquid water flooding phenomena forming process;
- Validated VOF algorithm application in bubble flow field;
- Improve the simplified model application on PEMFCs model, especially in DMFC anode;
- Improve the simplified model which could be adopted in different geometry design.

Chapter 2 Literature review

2.1 Review of PEMFC numerical simulation

2.1.1 Review of DHFC numerical simulation

At the end of the previous century, many researchers were involved in fundamental investigations into the basic operating principles of DHFCs, especially for the transport mechanism of hydrogen ions through membranes [14-18]. Since the beginning of the 21st century, high-performance computing techniques and advanced numerical algorithms have been employed in DHFC modeling [19-21]. However, in these studies, only single-phase flow (i.e., no liquid water was considered) was simulated. Although this simplification provides some insight into the physics of the DHFCs, it cannot be applied to real applications with DHFCs in which liquid water exists during most of the operations.

Numerous researchers such as You and Liu [22], Wang et al. [23], and Cha et al. [24] have developed two-phase flow models in which liquid water was considered to be water vapor to simplify the modeling process. These developments significantly improved the understanding of simulations with two-phase flow. Unfortunately, these so-called two-phase flow models are essentially multi-component single-phase flow models in which the liquid water that is treated as water vapor is only an additional species for the conventional single-phase model. Therefore, these models provide some important information about the water vapor, but the information regarding the water in the liquid phase is not included; thus, the interface between the gas phase and the liquid phase cannot be predicted.

As reported by numerous researchers [25, 26], liquid water exists in DHFCs, and liquid water flooding becomes a serious concern, especially when the DHFCs operate with high current density. The liquid water generated from the catalyst layer of the cathode can block the pores of the gas diffusion layer (GDL), which prevents the reactant air from reaching the catalyst layer. This blockage is the primary reason for the low performance of DHFCs and is the main source of stability and durability problems in DHFCs. In recent years, several modeling attempts have been made to help understand the fluid flow in GDL while anisotropic nature causes concerns as study in Karan et al.'s review [27] and Zhang et al.'s research [28]. Also, Wang et al. [29] investigated the water management in catalyst layer and gas diffusion layer with a Lattice Boltzmann model gave a good insight of flow pattern in the porous layer.

The behavior of liquid water inside the flow channels of single cells and cathode stacks was investigated by Zhou et al. [30-32] by using a volume of fluid (VOF) method that can directly track the interface between the gas phase and the liquid phase. However, these studies only focused on liquid water in the flow channels without considering the GDL and catalyst layer. Zhou et al. [33] also developed a general model for DHFCs in which a two-phase flow VOF model was coupled with detailed thermo-electro-chemical submodels. This general model of DHFCs can provide detailed information of the fluid flow, heat transfer, water behavior, and movement of electrons and ions. This model is state-of-the-art for DHFC modeling; however, it requires a large amount of computational resources. In a recent study, Zhou et al. [34] used the VOF algorithm to explore water behavior in serpentine flow channels and obtained a similar water deformation process and spatial-temporal position between the experimental visualization and numerical simulation. However, this simulation set the water inlet in the form of droplet injected from a pinhole, which caused some inconsistency compared to the actual liquid water generated in the fuel cell. Another type of water inlet with an initial distribution of water film that was used in an earlier study [30] had a similar problem. Of these water inlet methods, the method that emits water from the back surface of the porous layer with an accelerated model [35] is the best method to improve the fidelity of the simulation.

Accelerated models actually have been commonly used in life tests and other areas [36-41], but the application of this method in fuel cells related research was conducted by Zhou et al. for the first time [35]. The Chapter 4 of this thesis employs this method to shorten the computational time without sacrificing the major physics of liquid water flooding process.

2.1.2 Review of DMFC numerical simulation

With the development of DMFC, a number of studies have verified the CO₂ bubble have enormous influence in DMFC performance [42, 43]. Gas management in DMFC anode has realized as one of the mainly issues of DMFC research. Since DMFC technology is a further development of DHFC, efforts in developing mathematical models for DMFC have been limited until recent years. Researchers have introduced different CFD model to solve the bubble problem. Kulikovsky [44, 45] investigates a DMFC model which studied gaseous bubbles in the anode channel and obtained asymptotic solution. They also explored local molar concentration of methanol along the channel and its effect on formation of bubbles. Wang et al. [46] introduced the mixture model to study DMFC, explored the heat transfer, methanol crossover etc problems. But same with the mixture model used in DHFC, as the liquid was considered as mixture, no interface could be tracked. Liu et al. [47] improved the DMFC modeling research by developed a three-dimensioned flow model which basically could be defined as mixture model because no interface could be captured. Hong et al. [48]

chose lattice-Boltzmann and VOF methods to explore the CO₂ bubble dynamics. As their compare result, lattice-Boltzmann and VOF model are both effective ways to track the interface of two-phase flow but the application for complex geometry hasn't been explored.

For the objective of this thesis, VOF model is introduced to solve the two-phase problem in anode side of the DMFC. With the interface reconstruction scheme, the interface could be calculated more accurately.

According to study in Chapter 4, employing a volume of fluid (VOF) method is advantageous to track the interface between the gas phase and the liquid phase. It is possible to give further attempts to use VOF methodology to solve the similar problem of two phase flow in DMFCs. Chapter 5 - 8 developed a few different model of simplified DMFC anode with VOF method. A new geometry of GDLs was investigated. Like introduced above, GDL usually made of carbon paper or carbon cloth, the size of the pores of conventional GDLs are arbitrary, and the sizes of the pores are very small. Zhou et al. [49] designed a GDL with different micro-flow channels to solve liquid water flooding problems in conventional GDLs of DHFC. This design simulated the small holes in GDL without effective for water removal in the fluid channel, but neglected the effect of fluid convection inside GDL. In this study, the pores in GDL are well designed with uniformly holes distributed in a 0.1mm thickness porous layer sandwiched by a 0.1 mm thickness catalyst layer (CL) and a parallel designed channel on the other side.

2.2 Review of PEMFC experiment visualization

2.2.1 Review of DHFC experiment visualization

The liquid water behavior in DHFC has been investigated via experiments by scientists and researchers. Various imaging visualization techniques have been introduced into this area, for example, the direct optical visualization technique [50-51], the neutron imaging technique [52, 53], and the Magnetic Resonance Imaging (MRI) technique [54]. Interdigitated flow channels in DHFC cathode was experimentally explored by Yan et al. [55] and Prasad et al. [53]. The flow pattern of the interdigitated flow channel design, the parallel flow channel design and single-serpentine flow channel design were compared. All these researchers made great efforts on liquid water management in DHFC cathode, however, there's still no effective visualization technique can be used to track the details of liquid water behavior and corresponding flow fields in DHFC cathode, especially in GDL.

2.2.2 Review of DMFC experiment visualization

Different with DHFC cathode, more researchers tend to study the gas remove problem in DMFC anode by experiment. Pan et al. [56] explored the nucleation and growth of CO₂ bubbles generated by chemical reactions of sulfuric acid and sodium bicarbonate in three different types of micro-channels, and simulated this experiment. Xiong et al. [57] analysed the bubble generation and transport in a microfluidic device with high aspect ratio. Effect of liquid viscosity and surface tension were discussed accordingly. These studies have remarkable insight into gas bubble behaviors in the anode channel of DMFCs. However, two phase interaction cannot be predicted.

Meanwhile, many experiments of DMFC with visualization study of CO₂ bubble behavior in anode channels were set up, the effect of aqueous methanol solution flow rate, temperature, and concentration with serious of experiment were discussed [58, 59]. Experiment provide a good visualization data for CO₂ bubble behaviors in the flow channels, however, detailed bubble formation procedure and two phase interaction need to be probed into with numerical model studies.

Chapter 3 Numerical model setup

3.1 Governing equations

In the thesis, FLUENT [60] was used with a 3D unsteady VOF model to perform the numerical simulations and to track the gas–liquid interface inside of the computational domain. A UDF was applied in the calculation. The flow in the gas phase was assumed to be laminar. And pressure based solver was chosen with the first order implicit scheme.

The mass conservation law that governs unsteady, laminar flow can be written as:

$$\frac{\partial(\varepsilon\rho)}{\partial t} + \nabla \cdot (\varepsilon\rho\mathbf{u}) = 0 \quad (1)$$

For multi-phase flow, the mixture density can be defined as:

$$\rho = \alpha_2\rho_2 + (1 - \alpha_2)\rho_1 \quad (2)$$

where subscript 1 mean the primary phase and 2 means the secondary phase (liquid water in DHFC, and gas in DMFC).

Volume fraction of the secondary phase α_2 could be solved by the volume fraction equation as followed:

$$\frac{\partial(\varepsilon\alpha_2\rho_2)}{\partial t} + \nabla \cdot (\varepsilon\alpha_2\rho_2\mathbf{u}) = S_f \quad (3)$$

In this simplified model of PEMFC, $S_f = 0$.

The details of the VOF equation will be presented in next section.

The momentum equation can be expressed as:

$$\frac{\partial(\varepsilon\rho\mathbf{u})}{\partial t} + \nabla \cdot (\varepsilon\rho\mathbf{u}\mathbf{u}) = -\varepsilon\nabla p + \nabla(\varepsilon\mu\nabla\mathbf{u}) + \varepsilon\rho\mathbf{g} + S_u \quad (4)$$

where $\mu = \alpha_2\mu_2 + (1 - \alpha_2)\mu_1$, p is the static pressure, ε is the porosity, and \mathbf{u} is the velocity vector.

In this model, the surface tension was represented by using a continuum surface force (CSF) model in which the source term in the flow channel portion is expressed in terms of a pressure jump across the interface and can be written as:

$$S_u = \varepsilon \sigma \frac{\rho \kappa \nabla \alpha_2}{(\rho_1 + \rho_2) / 2} \quad (5)$$

where σ is the surface tension coefficient, ρ represents the density, κ represents the surface curvature, which is defined in terms of the divergence of the unit normal \hat{n} :

$$\kappa = \nabla \cdot \hat{n} = \frac{n}{|n|}$$

where $n = \nabla \alpha_2$ is the surface normal that is defined as the gradient of α_2 .

For the momentum equation in the porous layer, the source term is expressed using the second term on the right-hand side as an additional resistant force due to the porosity and permeability inside of the porous layer

$$S_u = \varepsilon \sigma \frac{\rho \kappa \nabla \alpha_2}{(\rho_1 + \rho_2) / 2} - \varepsilon \frac{\mu}{K} u \quad (6)$$

where K represents the permeability.

3.2 Interface tracking algorithm

In this model, PLIC (piecewise linear interface calculation) VOF tracking methods is implemented because it is accurate and applicable for general unstructured meshes [61].

The basic concept of VOF model is computation of convection and diffusion fluxes through a computational domain with impact of source terms inside the domain. With this computation, the volume fraction of each cell would be figured out and the interface will be reconstructed in each cell through an interpolating formulation.

The VOF geometric reconstruction process need go through two steps: reconstruction and propagation. The mainly objective of reconstruction step is segment of the interface inside the cell.

As the unit normal vector \mathbf{n} and the volume fraction value are computed in the VOF equation, the two factors determined the orientation and the location of the interface in terms of a straight line. After the straight line has been obtained, PLIC algorithm is employed to track the motion of the interface because of effect of flow field.

3.2.1 Interface reconstruction algorithm

As presented above, the objective of PLIC methods is determine a straight line in each cell. During this process, a estimation of straight line which perpendicular to an interface normal vector $\mathbf{n}_{i,j}$ and divide the two volume for phases. The normal vector $\mathbf{n}_{i,j}$ is determined from the neighboring cells based on block's $\alpha_{i,j}$ of 9 cells as shown in Fig. 3-1.

The normal vector $n_{i,j}$ could be calculated from $\alpha_{i,j}$, $n_{i,j} = \nabla \alpha_{i,j}$. Initially, a cell corner value of the normal vector $n_{i,j}$ is computed. An example at $i+1/2, j+1/2$ in 2D is as follows:

$$n_{x,i+1/2,j+1/2} = \frac{1}{2h} (\alpha_{i+1,j} - \alpha_{i,j} + \alpha_{i+1,j+1} - \alpha_{i,j+1}) \quad (7)$$

$$n_{y,i+1/2,j+1/2} = \frac{1}{2h} (\alpha_{i,j+1} - \alpha_{i,j} + \alpha_{i+1,j+1} - \alpha_{i+1,j}) \quad (8)$$

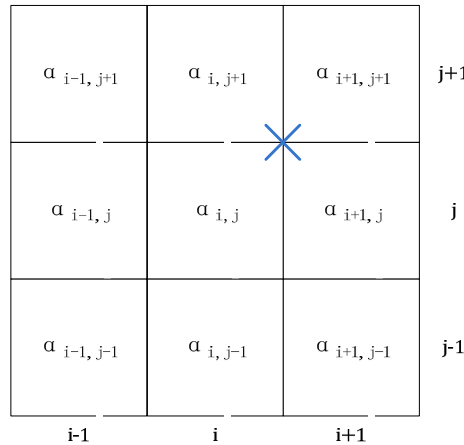


Fig. 3-1 Computational domain

The cell-centre values are solved by averaging:

$$n_{i,j} = \frac{1}{4} (n_{i+1/2,j-1/2} + n_{i-1/2,j-1/2} + n_{i+1/2,j+1/2} - n_{i-1/2,j+1/2}) \quad (9)$$

The most general equation for a straight line on a mesh with normal \mathbf{n} is

$$n_x x + n_y y = d \quad (10)$$

in which d is a parameter related to the smallest distance between the line and the origin.

3.2.2 Fluid advection algorithm

There are three steps of the advection algorithm:

First, construct and reconstruct the fluid interface with planar surface with straight line in each 2D cell as presented above.

The volume fraction $\alpha_{i,j}$ is truncated by the formula:

$$\alpha_{i,j}^{n+1} = \min[1, \max(\alpha_{i,j}^{n+1}, 0)] \quad (11)$$

at the $(n+1)$ time step.

Second, solve the velocity field. Move the fluid volume according to the local velocity

The velocity at the interface is interpolated linearly and the new position of the interface is calculated by the following formula:

$$x^{n+1} = x^n + u(\Delta t) \quad (12)$$

Third, update new volume fractions values in the computational cells.

The new volume fraction field is obtained according to the local velocity field, and fluxes at each cell are determined by algebraic or geometric approaches.

$$\widehat{\alpha}_{i,j} = \alpha_{i,j}^n + \frac{\Delta t}{\Delta x} [\alpha_{u,i-1/2,j} - \alpha_{u,i+1/2,j}] \quad (13)$$

$$\alpha_{i,j}^{n+1} = \widehat{\alpha}_{i,j} + \frac{\Delta t}{\Delta y} [\widehat{\alpha}_{v,i,j-1/2} - \widehat{\alpha}_{v,i,j+1/2}] \quad (14)$$

$\alpha_{u,i-1/2,j}$ denotes the horizontal flux of the (i, j) cell, $\widehat{\alpha}_{v,i,j-1/2}$ denotes the vertical flux of the (i, j) cell. Volume fractions are updated at time level n from x-sweep first and then y-sweep.

3.2.3 Implementation of surface tension

Surface tension also plays an important role in the interface formation and movement. The surface tension coefficient is implemented in the source term of the momentum equation as introduced above. The relationship of pressure drop across the surface could be expressed with Young–Laplace equation as [60]

$$\Delta p = \sigma \kappa = \sigma \left(\frac{1}{R_1} + \frac{1}{R_2} \right) \quad (15)$$

Where, R_1 and R_2 are the two radii in orthogonal directions, to measure the surface curvature.

A wall adhesion angle in conjunction with the surface tension model is also considered in the model. If θ_w is the contact angle at the wall, then the surface normal at the live cell next to the wall is

$$\hat{n} = \hat{n}_w \cos \theta_w + \hat{t}_w \sin \theta_w \quad (16)$$

Where \hat{n}_w and \hat{t}_w are the unit vector normal to the solid surfaces and the unit vector tangential to the solid surfaces, and θ_w is the contact angle at the solid surfaces.

Chapter 4 Interface phenomena in a DHFC cathode with an interdigitated design¹

4.1 Numerical model description

Fig. 4-1 shows a schematic of the computational domain that contains the cathode with an interdigitated flow design and a porous layer that represents both the catalyst layer and the GDL. Liquid water is introduced from the back surface of the porous layer along the z-direction into the porous layer domain to simulate water production inside of the cathode catalyst layer. The air inlet, cathode outlet, and other locations in this geometry are shown in Fig. 4-1. Seven branches (2 mm width, 1.7 mm depth, 1 mm rib width) are applied with a 0.3 mm porous layer attached with 2.4 mm × 2.4 mm effective area.

A flow rate inlet boundary condition (flow rate of $1.7 \times 10^{-4} \text{ kgs}^{-1}$ in the direction normal to the inlet boundary) was applied to the liquid water inlet surface (i.e., the back surface of the porous layer), as shown in Fig. 4-1. The air inlet used a constant flow rate of $2 \times 10^{-5} \text{ kgs}^{-1}$ as its boundary condition. The accelerated model could be applied by adjusting the molar mass flow rate ratio between liquid water and air. In the present study, this ratio is set as 13.7 : 1. At the cathode outlet, the boundary condition was set as a pressure outlet in which the pressure is the same as the atmosphere. The contact angles used in the boundary conditions of the upper wall, side wall, and other walls were 43°, 40° and 140°, respectively. The porosity of the porous layer was set to 0.5 with a permeability of $1 \times 10^{-11} \text{ m}^2$.

The computational domain consisted of 284,304 cells with a minimum grid size of $5 \times 10^{-13} \text{ m}^3$. The mesh size in the porous layer was 0.167 mm × 0.167 mm × 0.05 mm. The mesh size in the flow channel was 0.167 mm × 0.167 mm × 0.142 mm. This computational mesh setup is considered to be effective and reasonable according to Zhou's previous research [34], where, with a similar geometry and mesh size to that used in the present study, the numerical simulation results and the experimental results have been compared, and the grid independency check has been conducted.

¹ This is the outcome of joint research undertaken in collaboration with Chin-Hsiang Cheng, Huan-Ruei Shiu and Chun-I Lee and under the supervision of professor Biao Zhou.

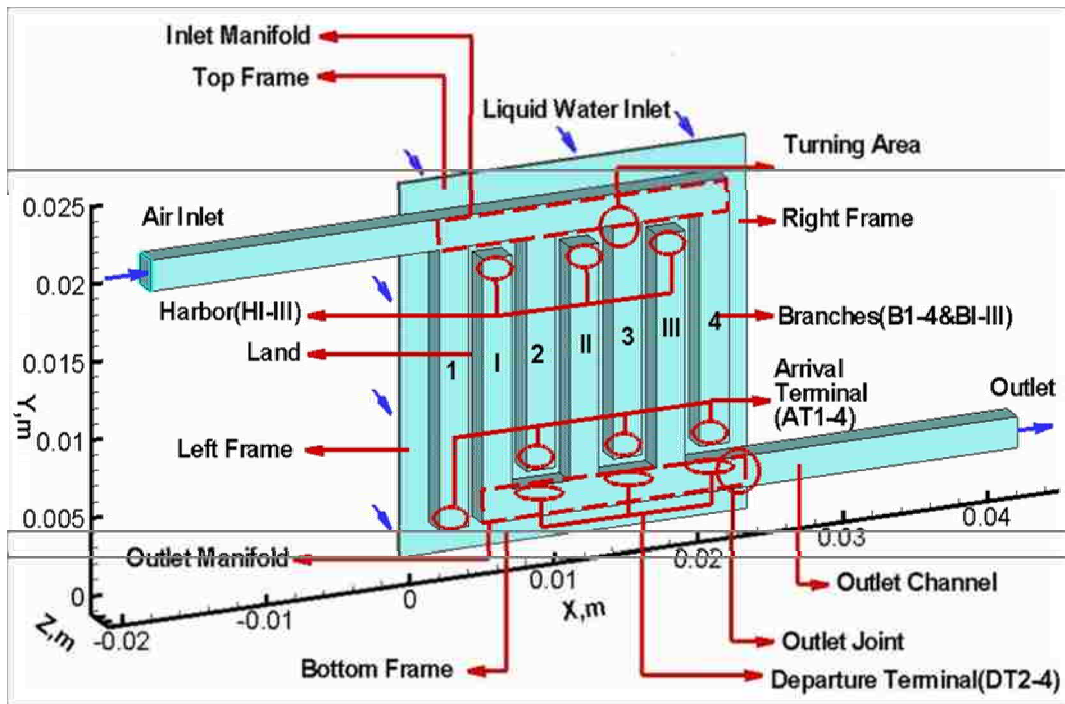


Fig. 4-1 Computational domain and definition of the components

4.2 Results and discussion

4.2.1 Validation with liquid water distribution inside the fuel cell cathode

To validate our numerical model, some neutron images (Fig. 4-2 (1 - 3 left column)) of liquid water distribution at different time for interdigitated DHFC presented by Prasad et al. [53] were selected to compare with the numerical results from the present study (Fig. 4-2(1 - 3 right column)).

From Fig. 4-2(1-3), the following general phenomenon can be observed from both experiments and numerical simulation.

(1) The locations of water emerging are both around Harbors (as defined in Fig. 4-1), as shown in Fig. 4-2(1-left) and Fig. 4-2(1-right).

(2) The liquid water accumulated nearby the departure terminals (as defined in Fig. 4-1), as shown in Fig. 4-2(2-left) and Fig. 4-2(2-right).

(3) As shown in Fig. 4-2(3-left) and Fig. 4-2(3-right), the liquid water accumulated in the outlet manifold and formed a rivulet; and also more liquid water accumulated in the outlet branches that are close to the air inlet.

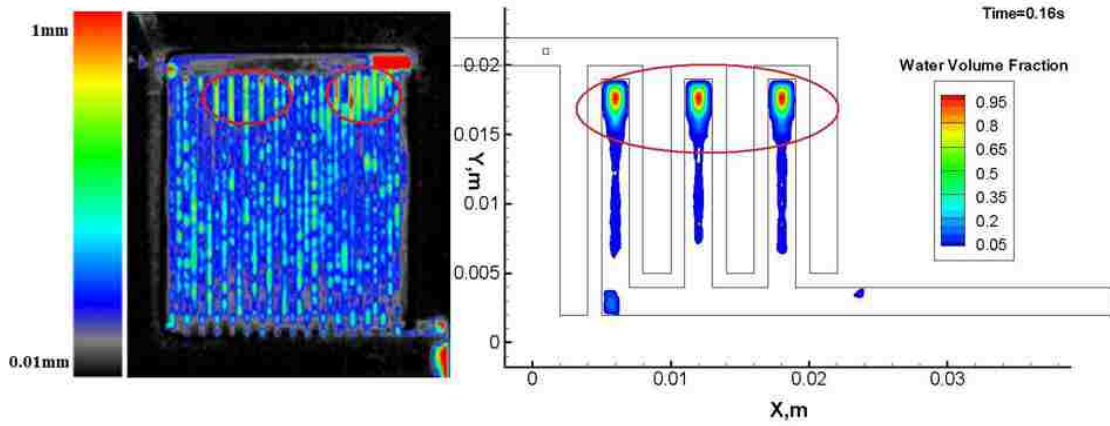


Fig. 4-2 (1)

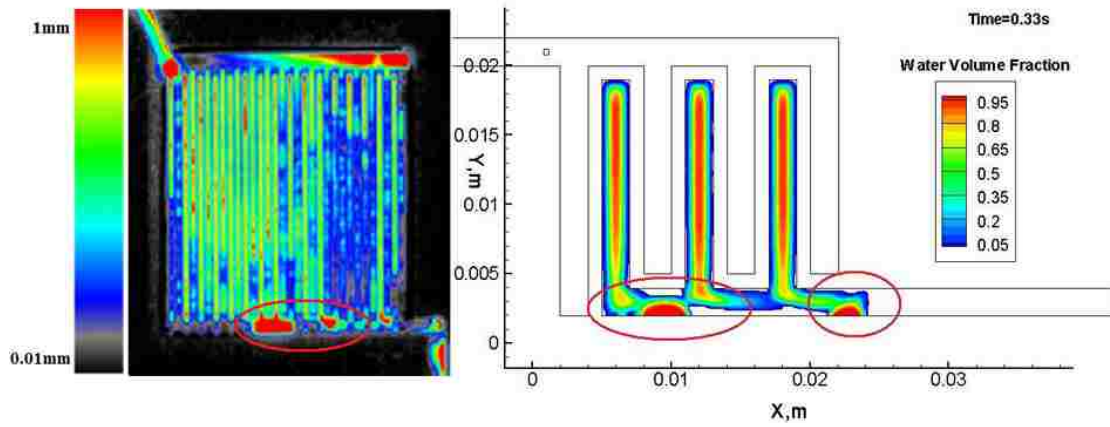


Fig. 4-2 (2)

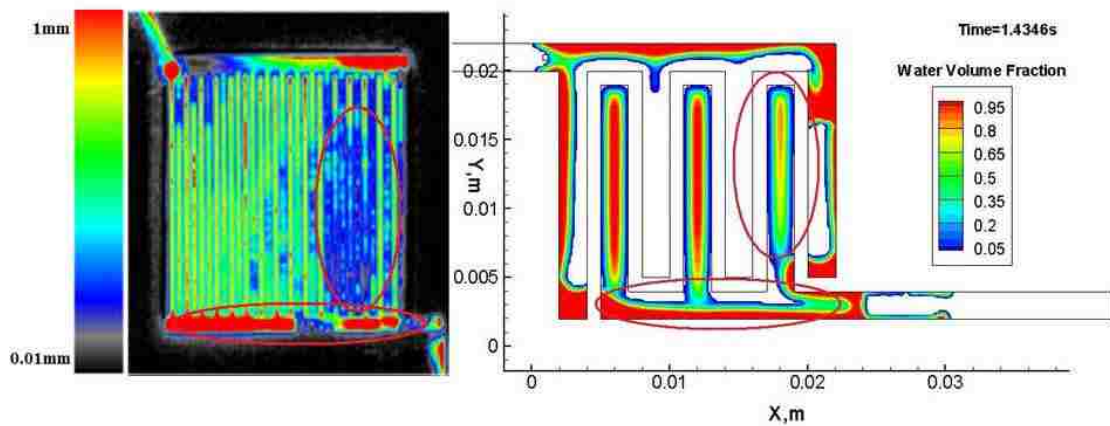


Fig. 4-2 (3)

Fig. 4-2 Comparison of numerical simulation and experimental visualization
 Fig. 4-2 (1 - 3 left column) Neutron images showing water distribution at different times [53];
 Fig. 4-2 (1 - 3 right column) Numerical simulation result of water distribution on selected cross section ($Z = 0.4 \text{ mm}$)

The readers may notice that the results from the experiment [53] include the liquid water in both anode and cathode while that of the numerical model was in cathode only. However, liquid water is produced in the cathode. Therefore, the main features we observed from the experiment images could be assumed to be manifested mainly by the cathode.

Based on the facts mentioned above, the numerical model presented in this paper can be a useful tool for the optimization of the fuel cell design.

4.2.2 General liquid water flooding process in the interdigitated cathode

As shown in Fig. 4-3(1) through Fig. 4-3(8), the liquid water flooding process for the PEMFC cathode with an interdigitated flow field and the porous layer can be summarized as follows:

- (1) The liquid water was introduced from the back surface of the porous layer with a prescribed flow rate, as described in Section 4.1;
- (2) As shown in Fig. 4-3(1), liquid water emerged in the porous layer under the harbors (HI, HII, HIII in Fig. 4-1);
- (3) As shown in Fig. 4-3(2), liquid water filled the porous layer under the outlet branches (BI, BII, BIII in Fig. 4-1) and then entered the outlet branches;
- (4) As shown in Fig. 4-3(3), liquid water gradually filled the porous layer except for the zones under the inlet branches (B1, B2, B3 in Fig. 4-1);
- (5) As shown in Fig. 4-3(4), liquid water accumulated around the peripheral zones of the porous layer under the frames (left, right, top, and bottom frames in Fig. 4-1), and some of the water in the porous layer near the outlet joint began to drain into the outlet channel, whereas the water that could not enter the outlet joint entered the inlet manifold and inlet branches B1 and B4;
- (6) Liquid water from outlet branches BI, BII, and BIII in Fig. 4-1 and the porous layer flowed into the outlet manifold and merged around the outlet joint. The water then continuously drained (in a stratified flow) through the outlet channel, as shown in Fig. 4-3 (5);
- (7) After the time period when the stratified drainage flowed through the outlet channel, an interesting liquid water shape with back-to-back (BTB) tulips formed near the outlet joint, as shown in Fig. 4-3 (6), and the liquid water accumulated around the top-right corner (the area near the intersection of the top frame and right frame in Fig. 4-1);
- (8) The amount of water that accumulated near this corner continuously expanded, i.e., continuously occupied the vicinity of this corner. At the moment when the front of the liquid water moving from this corner made contact with the inner bend of inlet branch 4 (B4 in Fig. 4-1), the accumulated water avalanched (this phenomenon will be discussed in Section 3.5), as shown in Figs. 3(7-8);
- (9) Process (7) and Process (8) periodically repeated.

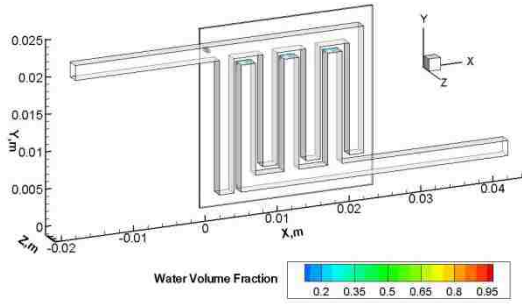


Fig. 4-3 (1) $t = 0.007$ s

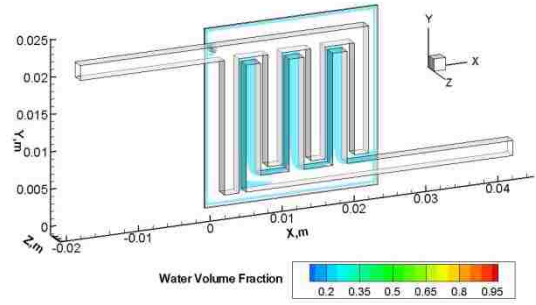


Fig. 4-3 (2) $t = 0.020$ s

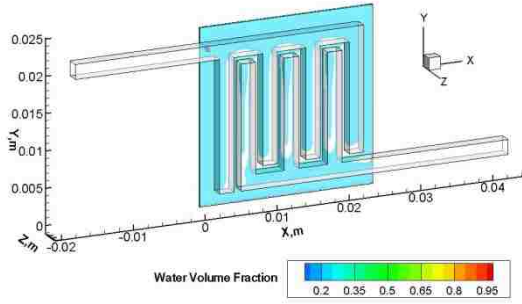


Fig. 4-3 (3) $t = 0.185$ s

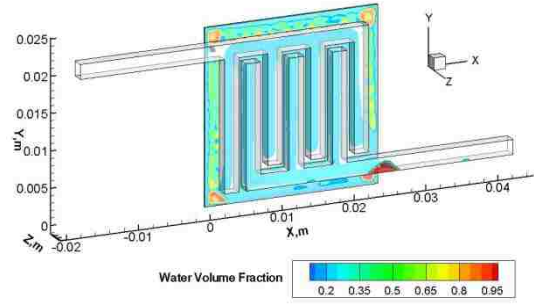


Fig. 4-3 (4) $t = 0.415$ s

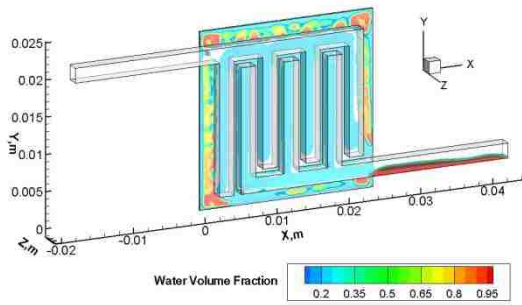


Fig. 4-3 (5) $t = 0.480$ s

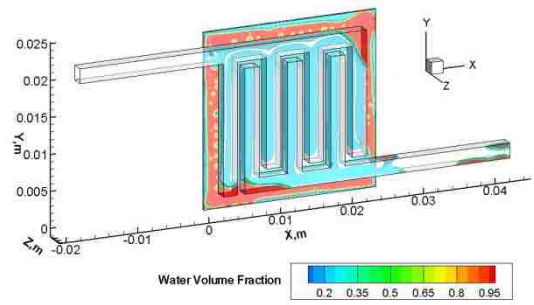


Fig. 4-3 (6) $t = 1.048$ s

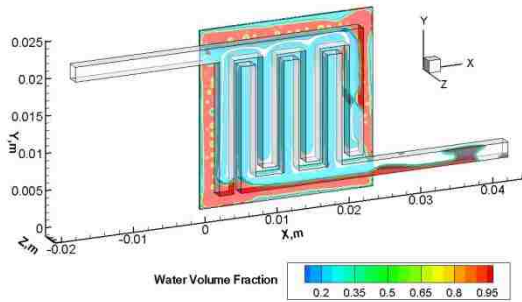


Fig. 4-3 (7) $t = 1.159$ s

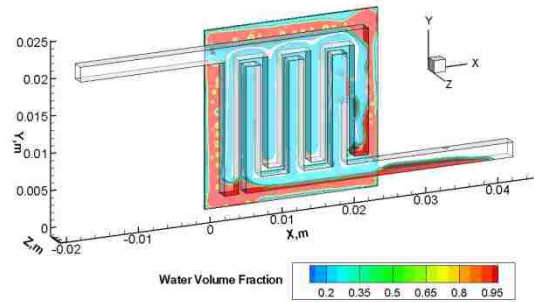


Fig. 4-3 (8) $t = 1.201$ s

Fig. 4-3 The general process of water behavior shown with 3D isosurfaces at (1) $t = 0.007$ s, (2) $t = 0.020$ s, (3) $t = 0.185$ s, (4) $t = 0.415$ s, (5) $t = 0.480$ s, (6) $t = 1.048$ s, (7) $t = 1.159$ s, (8) $t = 1.201$ s

4.2.3 Liquid water flooding behavior

Fig. 4-4 shows the detailed water flooding sub-processes in the porous layer Fig. 4-4

(1)-Porous Layer through Fig. 4-4 (17)-Porous Layer) and the flow channels (Fig. 4-4 (1)-Channels through Fig. 4-4 (17)-Channels). Fig. 4-4 (a)-Porous Layer shows the location of the selected cross section in the porous layer at $z = 0.15$ mm with the projection of the flow channels (inlet channel and manifold, outlet channel and manifold, and inlet branches and outlet branches). Fig. 4-4 (1)-Channels shows the location of the selected cross section in the flow channels at $z = 0.45$ mm.

In the following sections, the liquid water flooding behavior will be discussed first followed by a discussion of the flow channels.

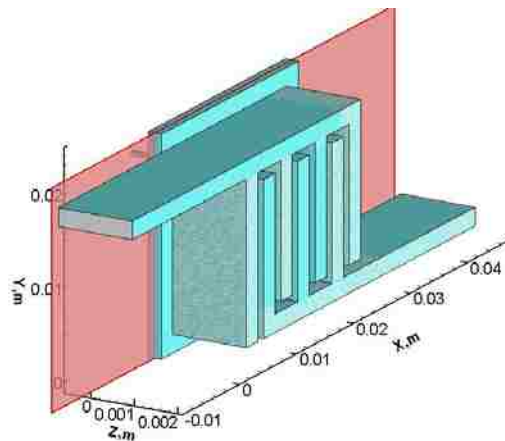


Fig. 4-4 (1)-Porous Layer Location of the cross section in the porous layer at $Z = 0.15$ mm with projection of the flow channels (inlet channel and manifold, outlet channel and manifold, and inlet branches and outlet branches) to observe the liquid water behavior in the porous layer

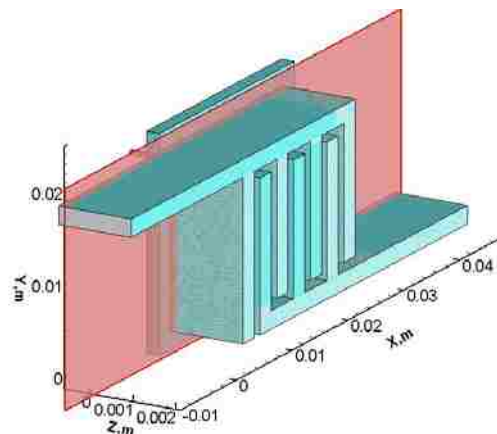


Fig. 4-4 (1)-Channels Location of the cross section in the flow channels at $Z = 0.45$ mm

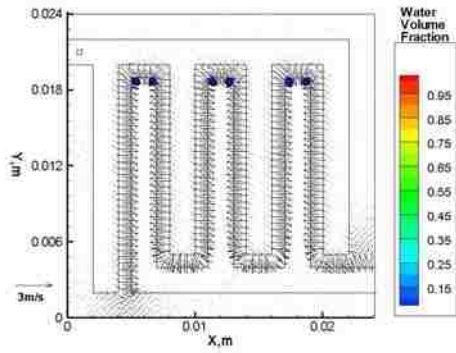


Fig. 4-4 (2)-Porous Layer $t = 0.030$ s

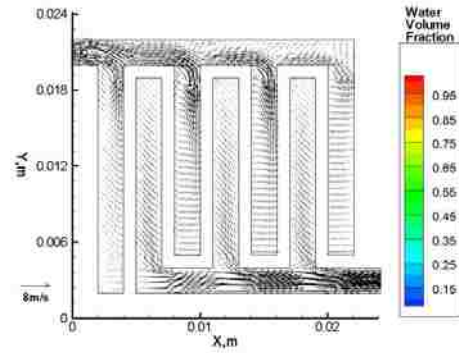


Fig. 4-4 (2)-Channels $t = 0.030$ s

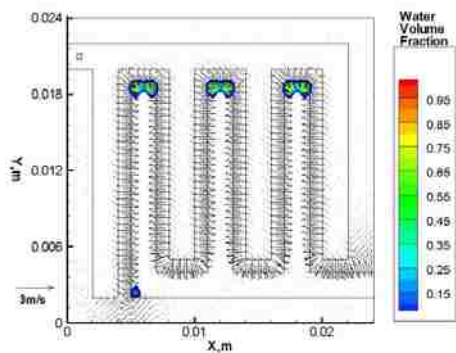


Fig. 4-4 (3)-Porous Layer $t = 0.050$ s

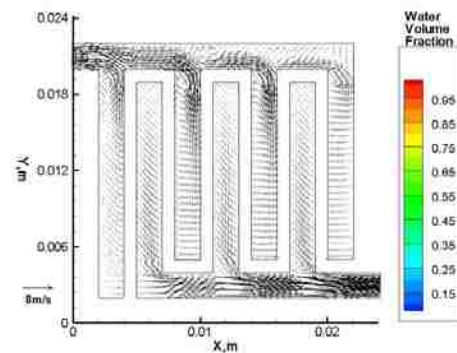


Fig. 4-4 (3)-Channels $t = 0.050$ s

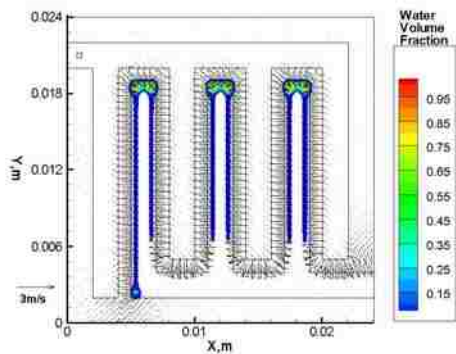


Fig. 4-4 (4)-Porous Layer $t = 0.053$ s

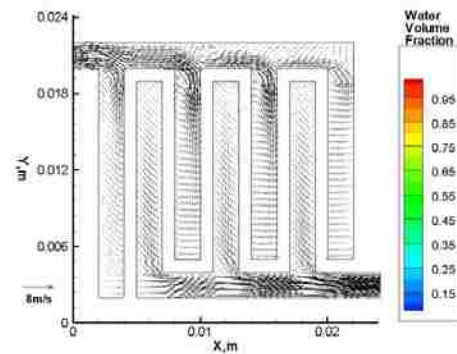


Fig. 4-4 (4)-Channels $t = 0.053$ s

Fig. 4-4 Water volume fraction and velocity vector in the selected cross section in the porous layer ($Z = 0.15$ mm) and the water volume fraction and velocity vector in the selected cross section in the flow channels ($Z = 0.45$ mm) at (2) $t = 0.030$ s, (3) $t = 0.050$ s, (4) $t = 0.053$ s

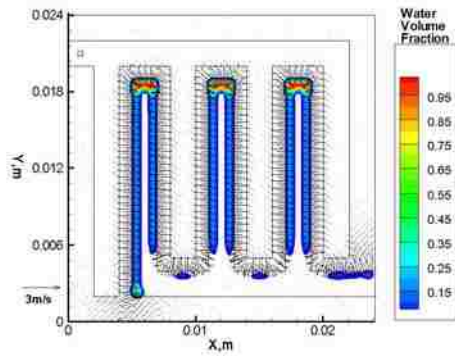


Fig. 4-4 (5)-Porous Layer $t = 0.064$ s

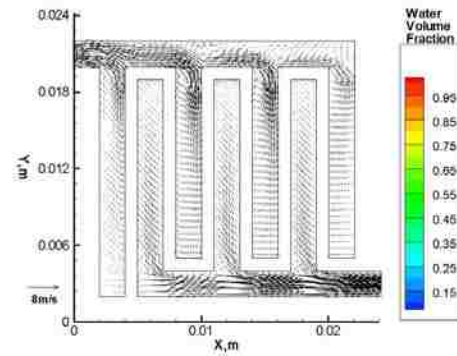


Fig. 4-4 (5)-Channels $t = 0.064$ s

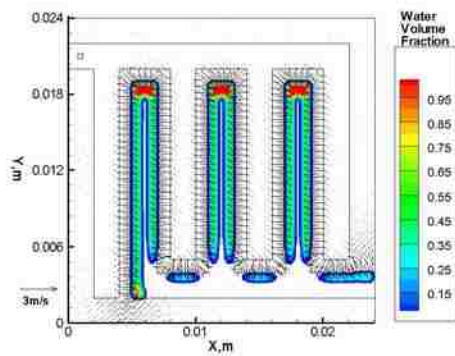


Fig. 4-4 (6)-Porous Layer $t = 0.081$ s

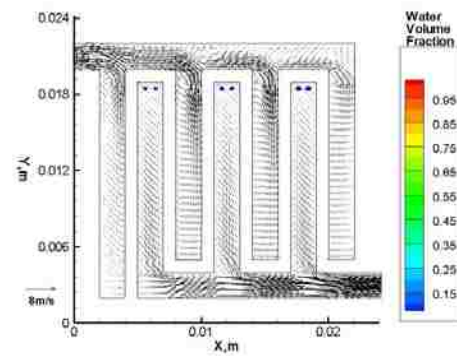


Fig. 4-4 (6)-Channels $t = 0.081$ s

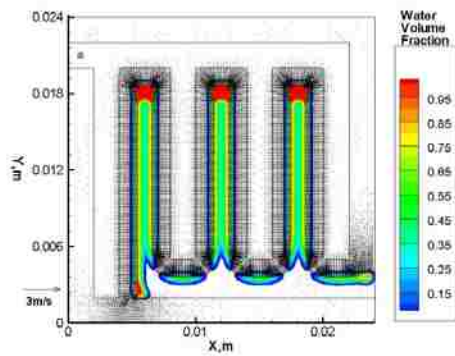


Fig. 4-4 (7)-Porous Layer $t = 0.100$ s

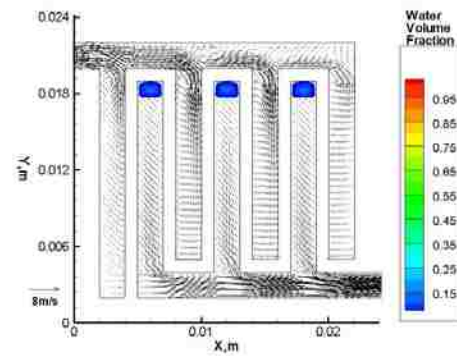


Fig. 4-4 (7)-Channels $t = 0.100$ s

Fig. 4-4-continue Water volume fraction and velocity vector in the selected cross section in the porous layer ($Z = 0.15$ mm) and the water volume fraction and velocity vector in the selected cross section in the flow channels ($Z = 0.45$ mm) at (5) $t = 0.064$ s, (6) $t = 0.081$ s, (7) $t = 0.100$ s.

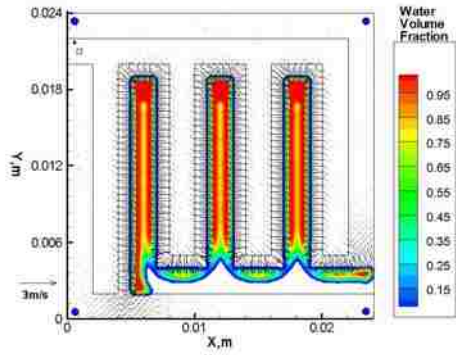


Fig. 4-4 (8)-Porous Layer $t = 0.116$ s

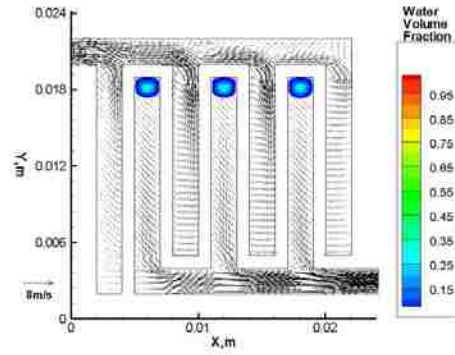


Fig. 4-4 (8)-Channels $t = 0.116$ s

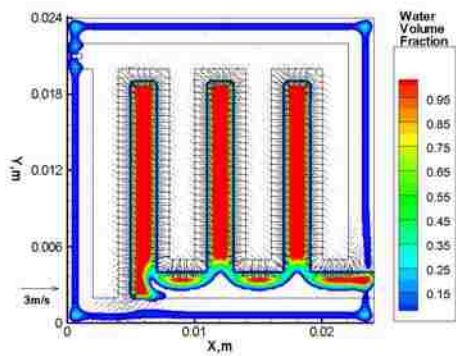


Fig. 4-4 (9)-Porous Layer $t = 0.143$ s

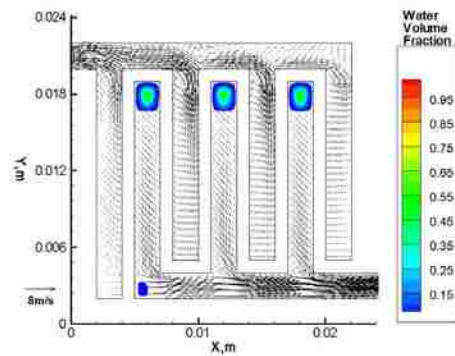


Fig. 4-4 (9)-Channels $t = 0.143$ s

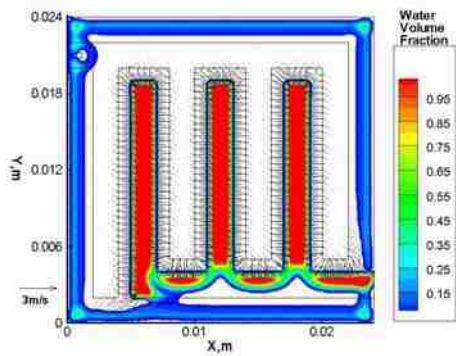


Fig. 4-4 (10)-Porous Layer $t = 0.162$ s

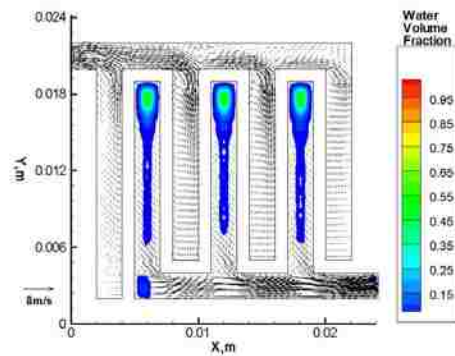


Fig. 4-4 (10)-Channels $t = 0.162$ s

Fig. 4-4-continue Water volume fraction and velocity vector in the selected cross section in the porous layer ($Z = 0.15$ mm) and the water volume fraction and velocity vector in the selected cross section in the flow channels ($Z = 0.45$ mm) at (8) $t = 0.116$ s, (9) $t = 0.143$ s, (10) $t = 0.162$ s

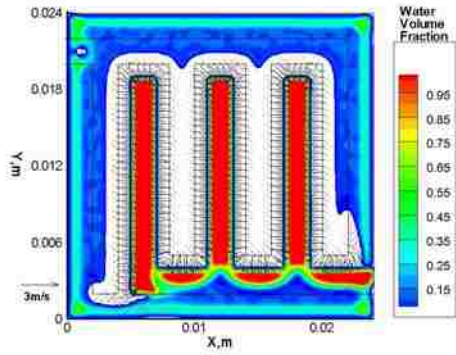


Fig. 4-4 (11)-Porous Layer $t = 0.185$ s

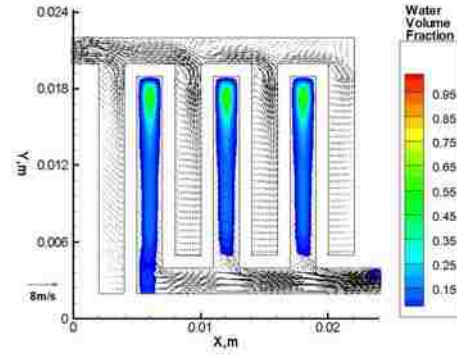


Fig. 4-4 (11)-Channels $t = 0.185$ s

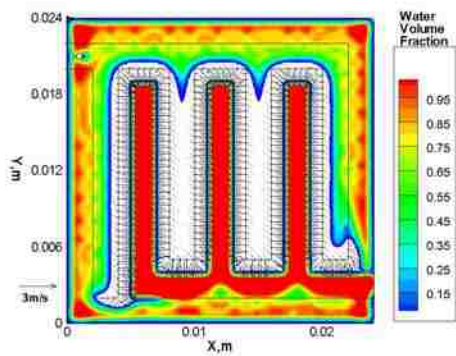


Fig. 4-4 (12)-Porous Layer $t = 0.280$ s

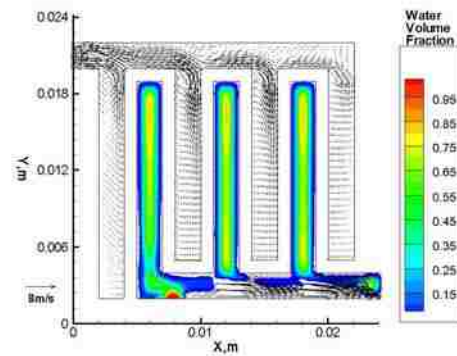


Fig. 4-4 (12)-Channels $t = 0.280$ s

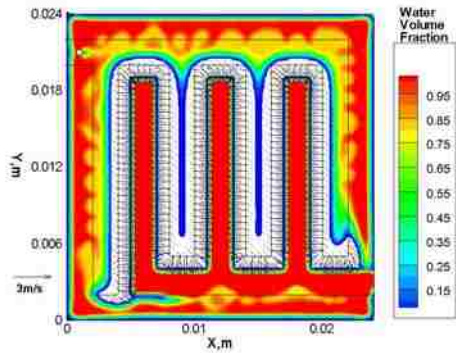


Fig. 4-4 (13)-Porous Layer $t = 0.311$ s

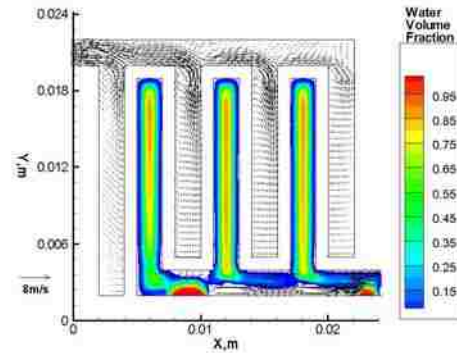


Fig. 4-4 (13)-Channels $t = 0.311$ s

Fig. 4-4-continue Water volume fraction and velocity vector in the selected cross section in the porous layer ($Z = 0.15$ mm) and the water volume fraction and velocity vector in the selected cross section in the flow channels ($Z = 0.45$ mm) at (11) $t = 0.185$ s, (12) $t = 0.280$ s, (13) $t = 0.311$ s

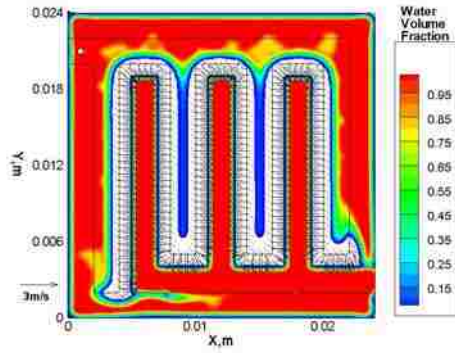


Fig. 4-4 (14)-Porous Layer $t = 0.359$ s

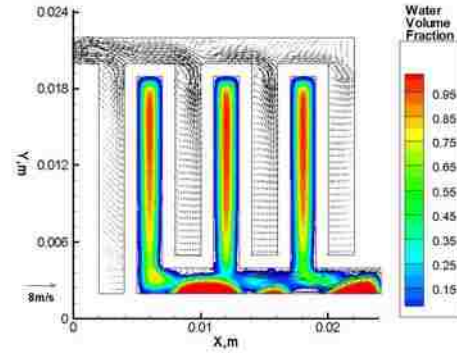


Fig. 4-4 (14)-Channels $t = 0.359$ s

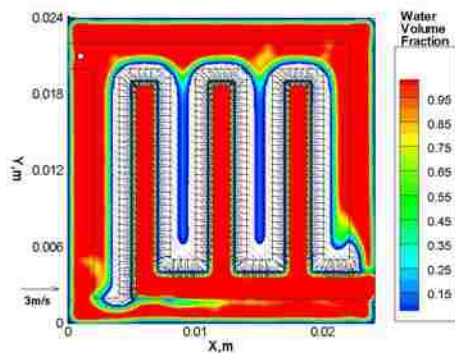


Fig. 4-4 (15)-Porous Layer $t = 0.385$ s

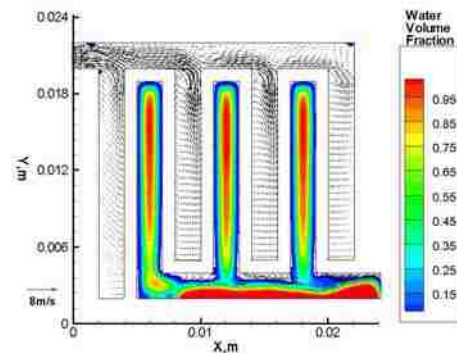


Fig. 4-4 (15)-Channels $t = 0.385$ s

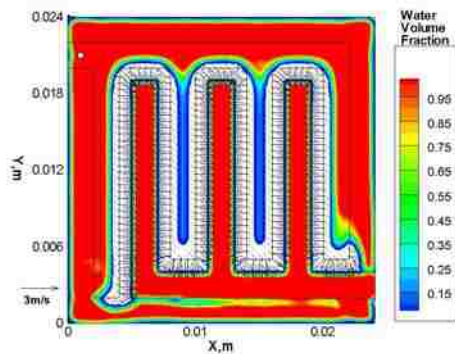


Fig. 4-4 (16)-Porous Layer $t = 0.419$ s

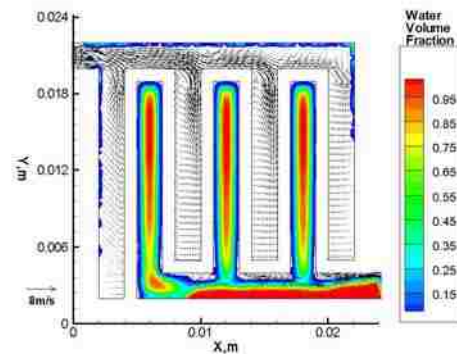


Fig. 4-4 (16)-Channels $t = 0.419$ s

Fig. 4-4-continue Water volume fraction and velocity vector in the selected cross section in the porous layer ($Z = 0.15$ mm) and the water volume fraction and velocity vector in the selected cross section in the flow channels ($Z = 0.45$ mm) at (14) $t = 0.359$ s, (15) $t = 0.385$ s, (16) $t = 0.419$ s.

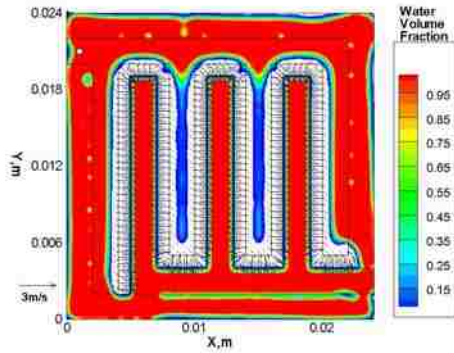


Fig. 4-4 (17)-Porous Layer $t = 0.826$ s

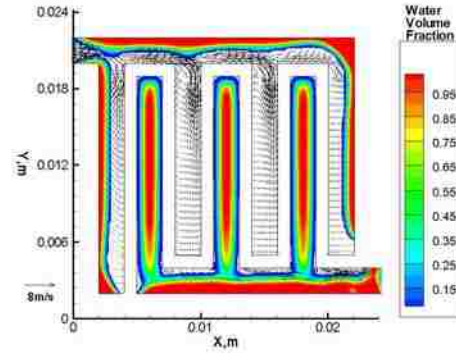


Fig. 4-4 (17)-Channels $t = 0.826$ s

Fig. 4-4-continue Water volume fraction and velocity vector in the selected cross section in the porous layer ($Z = 0.15$ mm) and the water volume fraction and velocity vector in the selected cross section in the flow channels ($Z = 0.45$ mm) at (17) $t = 0.826$ s.

The general process of liquid water flooding in the porous layer

(1): Liquid water emerged from the zones under the harbors (HI, HII, and HIII in Fig. 4-1) at a location near each corner of the harbors, as shown in Fig. 4-4 (2)-Porous Layer;

(2): The pairs of the two liquid water spots under the same harbor expanded to join and form a “sunglass” shape, and, around the same time, a small amount of water appeared as a liquid spot under the zones near the bottom left corner of the outlet manifold, as shown in Fig. 4-4 (3)-Porous Layer;

(3): The “sunglasses” evolved into a wooden barstool (WBS) by connecting with the “sunglass” legs that formed from the liquid water emitting from the zones under the peripheral edges of the outlet branches (BI, BII, and BIII in Fig. 4-1), and the WBS located under the first outlet branch (BI) exhibited unequal legs, as shown in Fig. 4-4 (4)-Porous Layer;

(4): The liquid water with a WBS shape continuously expanded, and some liquid water emerged from under the departure terminals (DT1, DT2, and DT3 in Fig. 4-1), as shown in Fig. 4-4 (5)-Porous Layer;

(5): Each pair of legs of the WBS’s continuously expanded to join and fill the zones under the corresponding outlet branch and to connect with the liquid water near the zones under the departure terminals, as shown in Fig. 4-4 (6)-Porous Layer to Fig. 4-4 (8)-Porous Layer;

(6): The liquid water from the peripheral zones of the porous layer (the zones under the four frames) emerged (as shown in Fig. 4-4 (8)-Porous Layer to Fig. 4-4 (9)-Porous Layer) and expanded to form relatively stable “golden arches” (as shown in Fig. 4-4 (11)-Porous Layer to Fig. 4-4 (15)-Porous Layer) in which the right leg exhibited a boot shape due to gas

from the last inlet branch (B4) traveling the shortest distance to the outlet channel from the porous layer.

The general process of liquid water flooding in the flow channels

Fig. 4-4 (2)-Channels through 4(5)-Channels show that no liquid water reached the selected cut-plane (Fig. 4-4 (1)-Channels), and the vertex around the entrance bend in the inlet branches is clearly shown.

Fig. 4-4 (7)-Channels through 4(11)-Channels show that liquid water from the porous layer began to reach this cut-plane (Fig. 4-4 (7)-Channels) then gradually expanded and occupied the outlet branches from the middle to the edge of the branches.

Fig. 4-4 (12)-Channels through Fig. 4-4 (17)-Channels show that liquid water from the three outlet branches began to move towards the outlet manifold, met the liquid water from the porous layer under the outlet manifold, and formed a rivulet along the bottom of the outlet manifold that flowed towards the outlet channel.

Fig. 4-4 (16)-Channels through Fig. 4-4 (17)-Channels show that liquid water under the frames gradually reached the inlet manifold and inlet branches B1 and B4 from the peripheral edges and formed a steady flow pattern for open-channel flow.

Air-liquid interaction and its effects

To understand the fundamental processes of both air and liquid water flowing through the cathode with an interdigitated design and a porous layer, the velocity field and liquid water volume fraction are shown in Fig. 4-5; this figure also shows the locations of the cross sections shown in Fig. 4-5 (2) and Fig. 4-5 (3). Fig. 4-5 (2) shows the process of the air from the inlet manifold entering the outlet branch (BII) underneath the porous layer near the harbor (HII). The air from the inlet manifold with a high pressure was forced into the lower porous layer by pushing the liquid water away and creating a path towards the nearby outlet branch (BII). Fig. 4-5 (3) shows a similar process of the air from the inlet branch (B3) entering the outlet manifold.

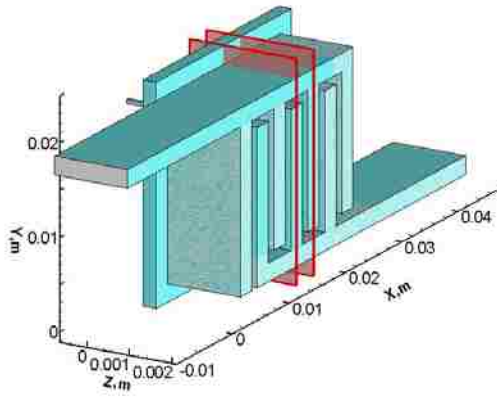


Fig. 4-5 (1) Location of the cross sections at X = 12 mm and X = 15 mm

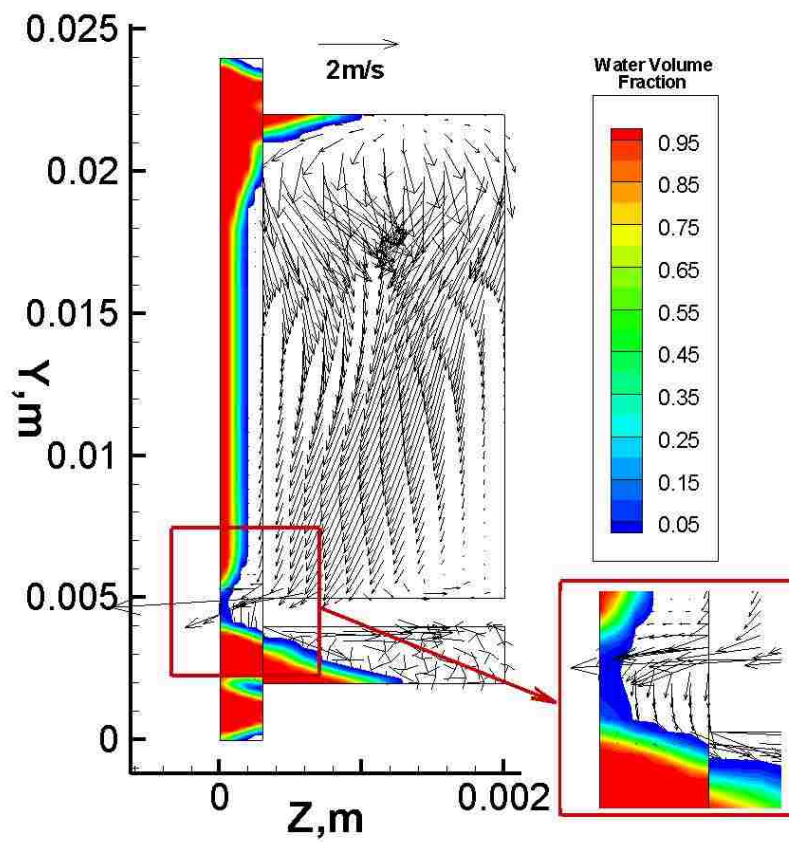


Fig. 4-5 (2) Water volume fraction and velocity vectors in the cross section at X = 12 mm at t = 0.419 s

Fig. 4-5 Water volume fraction and velocity vectors in the cross sections (X = 12 mm and X = 15 mm) at t = 0.419 s

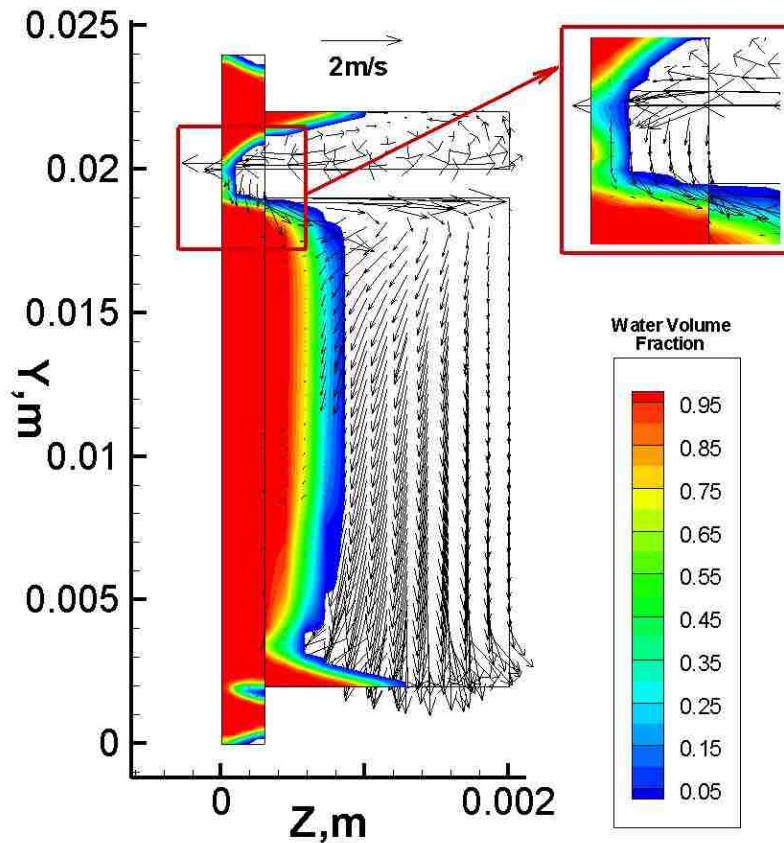


Fig. 4-5 (3) Water volume fraction and velocity vectors in the cross section at $X=15$ mm at $t = 0.419$ s

Fig. 4-5-continue Water volume fraction and velocity vectors in the cross sections ($X = 12$ mm and $X = 15$ mm) at $t = 0.419$ s

Fig. 4-6 illustrates the interaction of liquid water and air by showing the velocity vector and liquid water volume fraction at various times ($t = 0.006$ s to $t = 0.917$ s), and Fig. 4-6 (1) shows the location of the three cross sections.

As shown in Fig. 4-6, the water movement in the three selected cross sections exhibits a similar deformation process but is not synchronized, which might explain the flooding behavior shown in Fig. 4-6.

The detailed evolution process described below is based on cut-plane 2, which was slower than the process in cut-plane 1 and faster than the process in cut-plane 3.

From Fig. 4-6 (2-9), the liquid water movement inside of the porous layer and the process of the liquid water entering the flow channels can be summarized as follows:

Initially (i.e., the instant just after the startup of the fuel cell, as shown in Fig. 4-6 (2)), the

air traveling from the inlet branches moves to the porous layer under the land then enters the outlet branches. This airflow pattern gradually results in liquid water accumulation that exhibits a half-mango shape on the membrane catalyst layer interface around the intersection of the outlet branches and their adjacent land inside of the porous layer.

As shown in Fig. 4-6 (3), the pair of two half-mangoes near the same outlet branches gradually merge in the middle to form a half-dumbbell under the outlet branches, whereas a half-mango shape appears under the inlet branches (B2 and B3) inside of the porous layer, and the liquid water exhibits a pancake shape under the other two inlet branches (B1 and B4). A half-dumbbell shape formed under each outlet branch due to the flow from the two neighboring inlet branches through the porous layer under the land in between. The half-mango shape under each inlet branch formed due to airflow from the inlet branch to the two neighboring outlet branches through the porous layer under the land in between.

As shown in Fig. 4-6 (4-9), the liquid water in the different cut-planes undergoes the same evolution process, i.e., the liquid water under the outlet branches changes from a half-dumbbell to a half-sine-wave to a cowboy hat shape and finally to a Bunsen flame shape.

This evolutionary process slows down from cut-planes 1 to 3, and, at certain times (e.g., $t = 0.475$ s, as shown in Fig. 4-6 (8)), the Bunsen-shaped liquid water for each plane begins to reach a somewhat “stable” and similar shape (Fig. 4-6 (8-9)). On the other hand, the liquid water under inlet branches B2 and B3 exhibits nearly the same half-mango shape over time, whereas the liquid water under inlet branches B1 and B4 initially forms a pancake shape (Fig. 4-6 (4)). It accumulates inside of the porous layer and the frames (left and right frames), and eventually rises to inlet branches B1 and B4 along the side wall of the branches, as shown in Fig. 4-6 (8-9).

This process of air moving from one channel through the porous layer into another channel, along with Fig. 4-6, can be used to explain the “golden arches” discussed in Section 4.2.3.

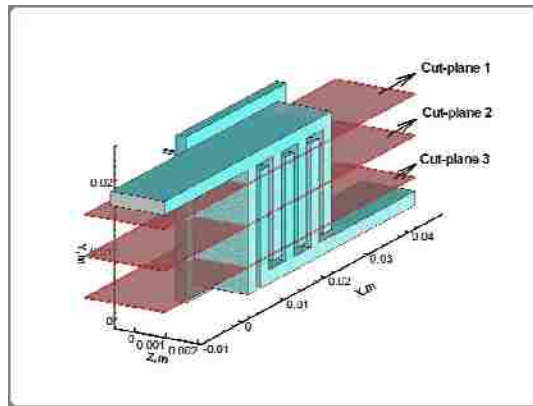


Fig. 4-6 (1) Location of the cross sections at $Y = 6 \text{ mm}$, $Y = 12 \text{ mm}$, and $Y = 18 \text{ mm}$

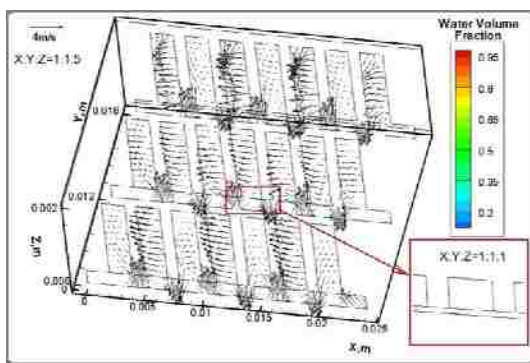


Fig. 4-6 (2) $t = 0.006 \text{ s}$

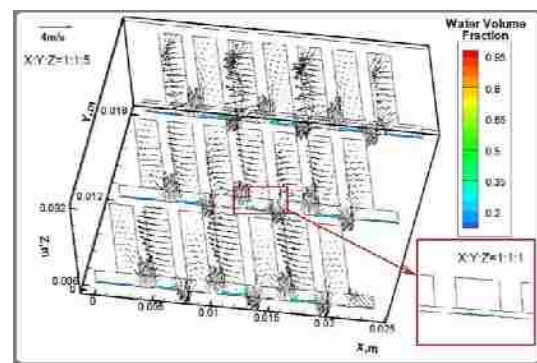


Fig. 4-6 (3) $t = 0.015 \text{ s}$

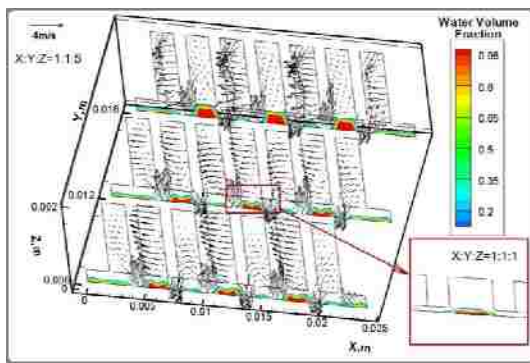


Fig. 4-6 (4) $t = 0.091 \text{ s}$

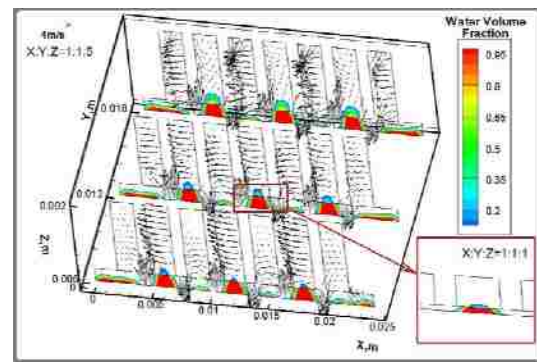


Fig. 4-6 (5) $t = 0.156 \text{ s}$

Fig. 4-6 Water volume fraction and velocity vectors in the cross sections ($Y = 6 \text{ mm}$, $Y = 12 \text{ mm}$, and $Y = 18 \text{ mm}$) at (2) $t = 0.006 \text{ s}$, (3) $t = 0.015 \text{ s}$, (4) $t = 0.091 \text{ s}$, (5) $t = 0.156 \text{ s}$,

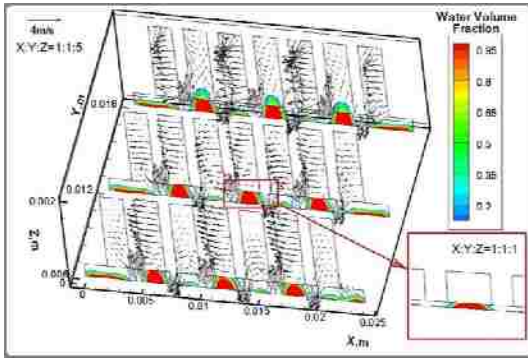


Fig. 4-6 (6) $t = 0.169$ s

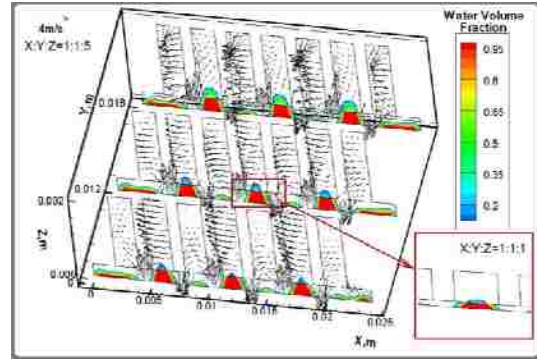


Fig. 4-6 (7) $t = 0.185$ s

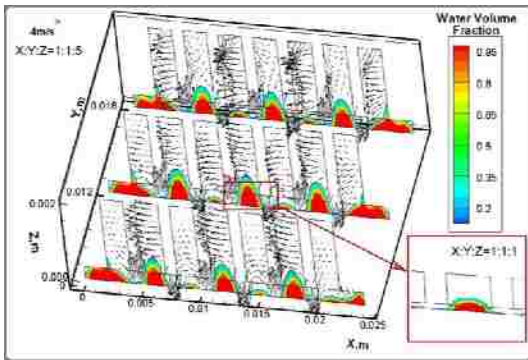


Fig. 4-6 (8) $t = 0.475$ s

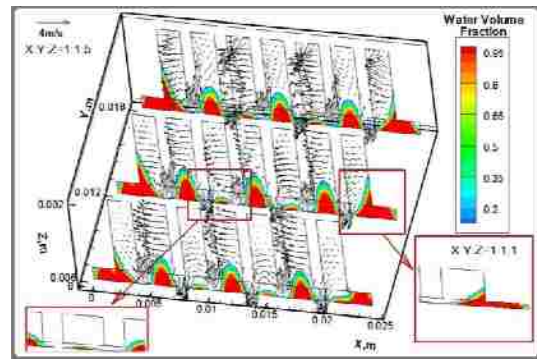


Fig. 4-6 (9) $t = 0.917$ s

Fig. 4-6-continue Water volume fraction and velocity vectors in the cross sections ($Y = 6$ mm, $Y = 12$ mm, and $Y = 18$ mm) at (6) $t = 0.169$ s, (7) $t = 0.185$ s, (8) $t = 0.475$ s, (9) $t = 0.917$ s

4.2.4 Liquid water outflow process through the outlet channel

Fig. 4-7 shows a front view of the liquid water outflow process through the outlet channel. This front view is typically used in experiments in which liquid water behavior is recorded using a camera. Figure 8 shows the liquid water distribution in the selected cross sections in the 3D outlet channel.

From Fig. 4-7, the liquid water outflow process can be described as follows:

(1) At the moment when the liquid water from the outlet branches meets in the outlet manifold, forms a liquid stream (hereafter referred to as “the first liquid water stream”), and reaches the outlet joint, this stream of liquid water then begins to drain through the outlet channel with a bottom-stratified flow pattern Fig. 4-7 (1) for some period of time;

(2) Until the moment when the liquid water in the zones under the right frame (hereafter referred to as “the second liquid water stream”) reached the outlet joint from the porous layer and met with the first liquid water stream, as shown in Fig. 4-7 (2), a forward-tulip shape quickly formed due to a contact angle of 43° , and thus the liquid water wet the side wall of

the outlet channel, as shown in Fig. 4-6 (3);

(3) The outlet joint was blocked due to the formation of the forward tulip, and, at the same time, the air moving from all directions and meeting around the departure terminal (DT4) (hereafter referred to as the discharge air stream) began to strike the forward-tulip-shaped liquid water blockage. Eventually, a backward-tulip shape formed at the back of the forward tulip, and thus the BTB tulips appeared, as shown in Fig. 4-7 (4);

(4) Due to the BTB tulips being continuously struck by the discharge air stream, the tulips moved forward, and the thickness between the two cusps of the BTB tulips decreased, as shown in Fig. 4-7 (5). Eventually, the BTB tulips broke up into a top-bottom-stratified pattern, as shown in Fig. 4-7 (6);

(5) Processes (2) through (4) repeated, and some of the latter top-bottom-stratified liquid water caught up to the water ahead, formed new BTB tulips, and moved away from the outlet channel, which formed small droplets as they moved around.

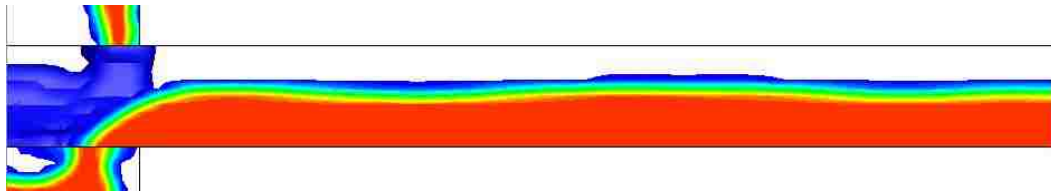


Fig. 4-7 (1) $t = 0.753$ s

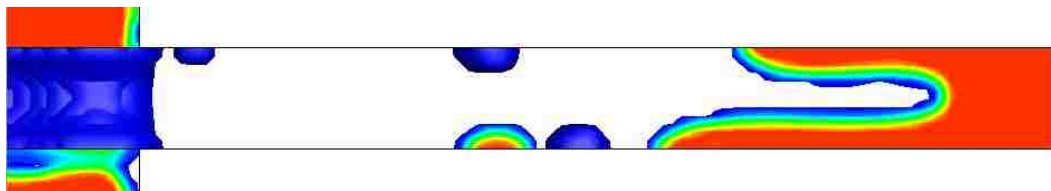


Fig. 4-7 (2) $t = 1.367$ s

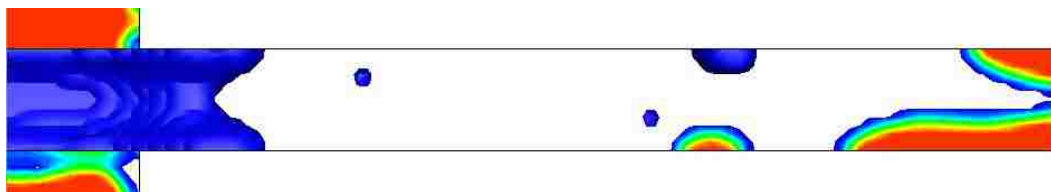


Fig. 4-7 (3) $t = 1.383$ s

Fig. 4-7 Water outflow process from the outlet channel shown from the XY view at (1) $t = 0.753$ s, (2) $t = 1.367$ s, (3) $t = 1.383$ s

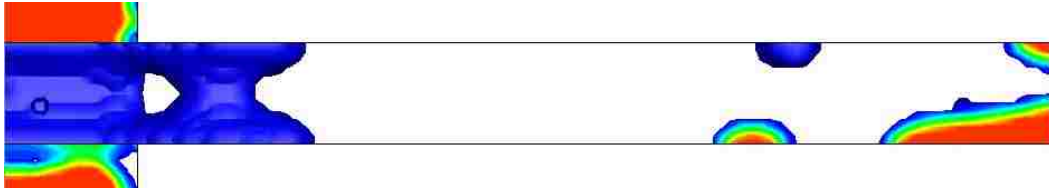


Fig. 4-7 (4) $t = 1.388$ s

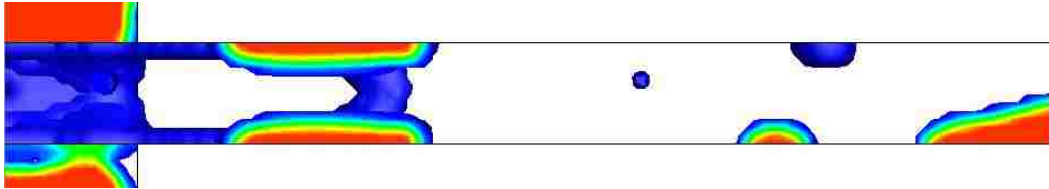


Fig. 4-7 (5) $t = 1.391$ s

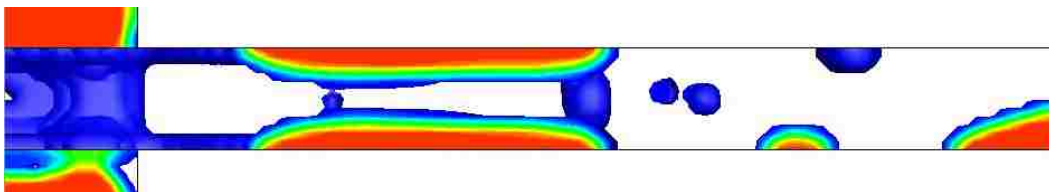


Fig. 4-7 (6) $t = 1.393$ s

Fig. 4-7-continue Water outflow process from the outlet channel shown from the XY view at (4) $t = 1.388$ s, (5) $t = 1.391$ s, (6) $t = 1.393$ s

The phenomenon shown in Fig. 4-7 can be observed in the experiments by recording the liquid water behavior from the front view because it is a 2D phenomenon.

Details of the liquid water outflow process through this outlet channel are shown in Fig. 4-8. This 3D process can be described as a process in which the liquid water accumulates on the back surface of the outlet channel around the outlet joint and is forced to flow out by the discharge air stream. The liquid water is then forced to redistribute in the outlet channel, from the back surface to the corners, the top, bottom, and front surfaces as well as the middle of the channel.

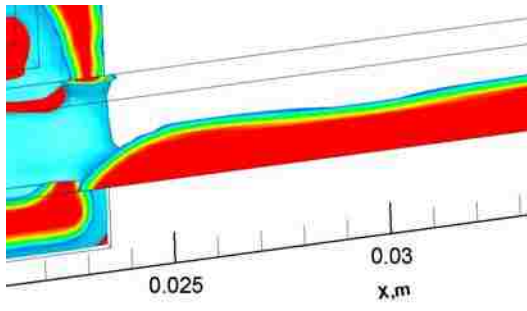


Fig. 4-8 (1)-3D $t = 0.753$ s

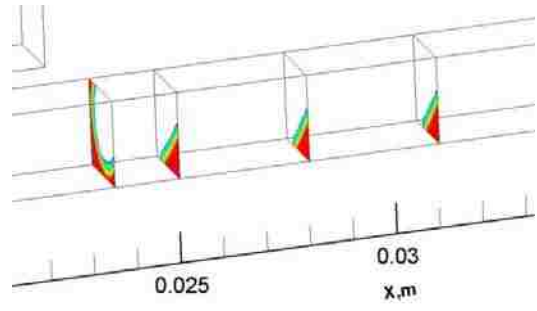


Fig. 4-8 (1)-Cross Sections $t = 0.753$ s

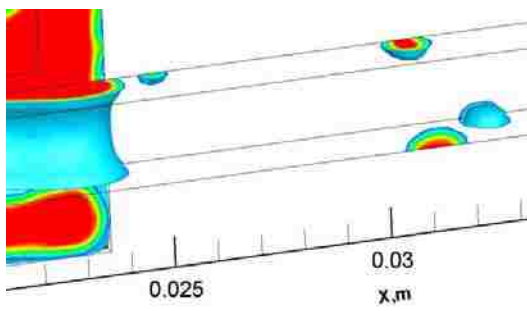


Fig. 4-8 (2)-3D $t = 1.367$ s

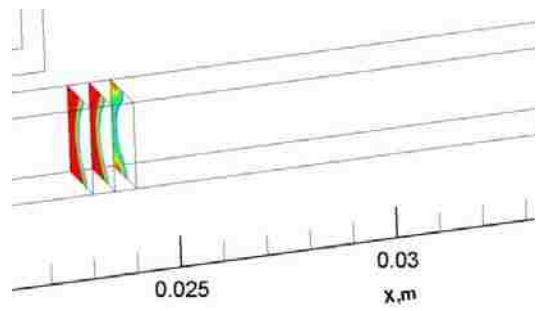


Fig. 4-8 (2)-Cross Sections $t = 1.367$ s

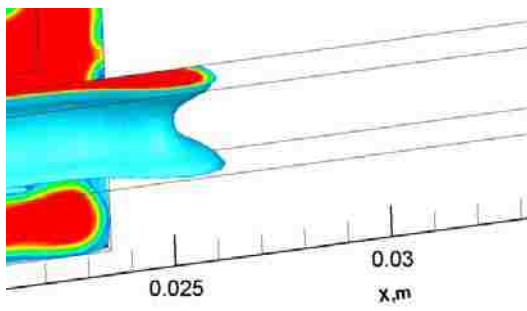


Fig. 4-8 (3)-3D $t = 1.383$ s

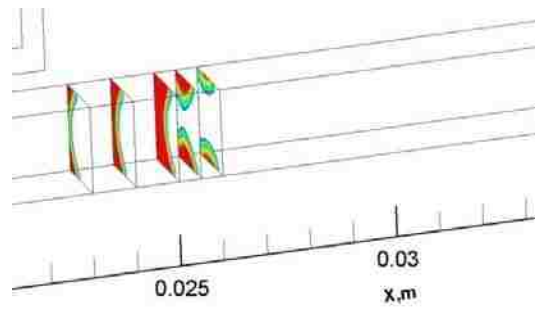


Fig. 4-8 (3)-Cross Sections $t = 1.383$ s

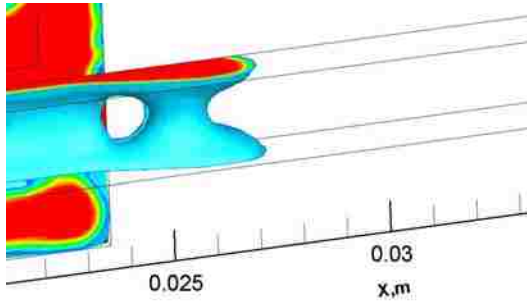


Fig. 4-8 (4)-3D $t = 1.388$ s

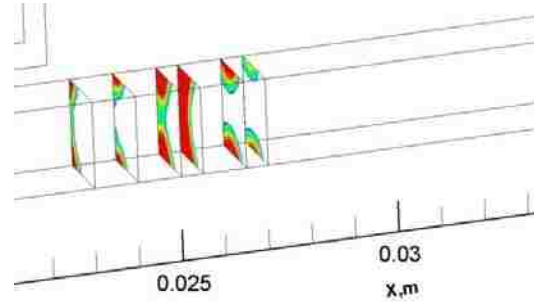


Fig. 4-8 (4)-Cross Sections $t = 1.388$ s

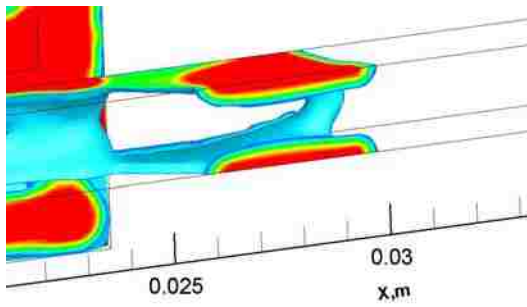


Fig. 4-8 (5)-3D $t = 1.391$ s

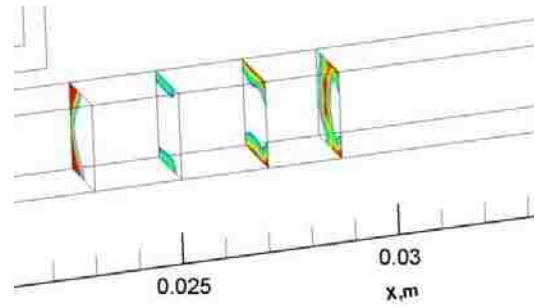


Fig. 4-8 (5)-Cross Sections $t = 1.391$ s

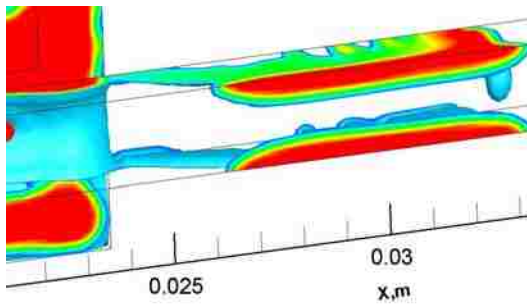


Fig. 4-8 (6)-3D $t = 1.393$ s

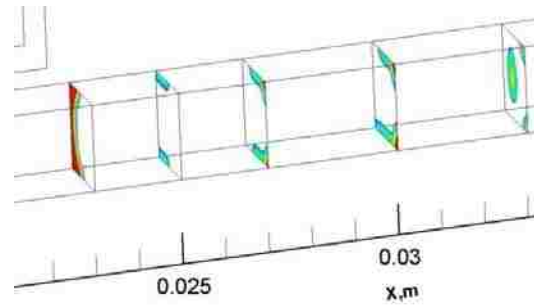


Fig. 4-8 (6)-Cross Sections $t = 1.393$ s

Fig. 4-8 Liquid water distribution in the 3D outlet channel and in the cross sections at (1) $t = 0.753$ s, (2) $t = 1.367$ s, (3) $t = 1.383$ s, (4) $t = 1.388$ s, (5) $t = 1.391$ s, (6) $t = 1.393$ s

4.2.5 Liquid water avalanche around the top-right corner

Fig. 4-9 shows the liquid water avalanche process around the top-right corner. This process can be described as follows:

- (1) The liquid water accumulated around the top-right corner, as discussed in 4.2.3;
- (2) When the accumulated water front made contact with the inner bend in inlet branch 4

(B4 in Fig. 1), this water began to avalanche, as shown in Fig. 4-9 (1). Due to this contact, the accumulated water blocked the bend in the last inlet branch (B4);

(3) When this blockage occurred, the air from the inlet manifold began to strike the stagnant water and formed an upward tulip and a downward tulip due to the wetting effect (similar to the effect mentioned in Section 4.2.3). At the same time, BTB tulips formed inside of the bend and the last inlet branch (B4) and then moved along the last inlet branch (B4) while the BTB tulips broke up into a left-right-stratified pattern, as shown in Fig. 4-9 (2);

(4) The left-stratified liquid water entered the outlet branch (BIII) beneath the porous layer and then moved to the outlet manifold, whereas the right-stratified liquid water continuously moved along the right surface in the last inlet branch (B4) and accumulated near the last arrival terminal (AT4). Then, the water either moved to the last departure terminal (DT4) or the last outlet branch (BIII) through the porous layer, as shown in Fig. 4-9 (3-4);

(5) The water from the avalanche eventually merged with the water in the outlet manifold and typically generated a strong wave that disturbed the water flow pattern in the outlet channel as it drained.

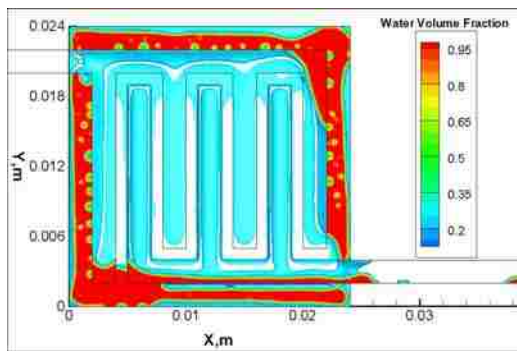


Fig. 4-9 (1) $t = 1.138$ s

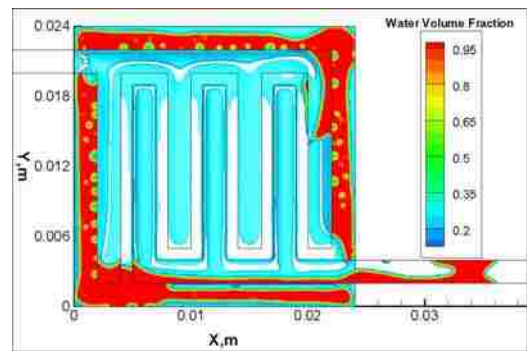


Fig. 4-9 (2) $t = 1.155$ s

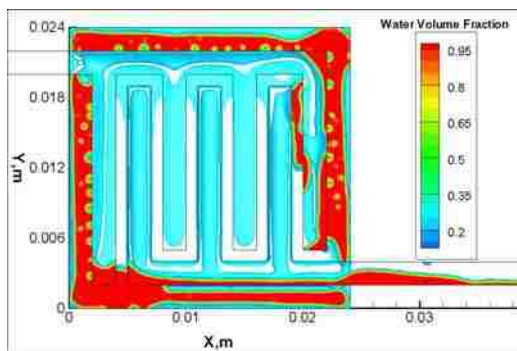


Fig. 4-9 (3) $t = 1.178$ s

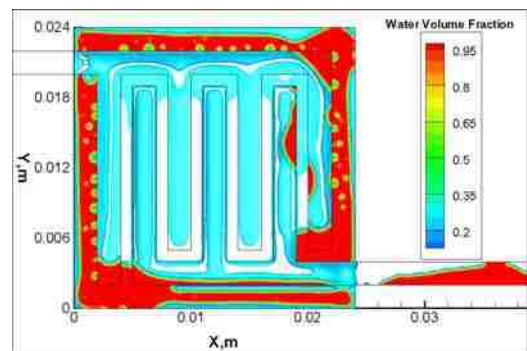


Fig. 4-9 (4) $t = 1.277$ s

Fig. 4-9 The avalanche process and the draining process shown from the XY view at (1) $t = 1.138$ s, (2) $t = 1.155$ s, (3) $t = 1.178$ s, (4) $t = 1.277$ s

4.2.6 Amount of liquid water over time and the flooding phases

Based on the variation in the amount of liquid water over time in the porous layer, flow channels, and cathode, the liquid water flooding process inside of the cathode with the interdigitated design can be divided into three phases: the porous layer phase, in which the liquid water generated from the interface of the membrane and catalyst layer accumulates inside of the porous layer, the channel phase, in which the liquid water accumulates in the flow channels and the porous layer, and the drainage phase, in which the liquid water drains from the outlet channel.

The time for the porous layer phase can be defined as the time period from $t = 0$ to Cowboy Hat Time (CHT as defined in Fig. 4-10), i.e., the instant when the half-sine-wave shape begins to form the cowboy hat shape, as shown in Fig 4-6 (6). During this phase, no liquid water was inside of the flow channels, and the liquid water inside of the porous layer changed from a half-mango shape to a cowboy hat shape.

The time for the channel phase can be defined as the time period from CHT to the Departure Time (DT as defined in Fig. 4-10), which is the instant when the liquid water inside the outlet manifold begins to flow from the outlet channel. During this phase, the liquid water inside of the porous layer around the zones under the frames, which was initially shaped like a pancake (e.g., Fig 4-6 (3)), accumulated, as shown in Fig. 6(7). During this phase, the liquid water with a cowboy hat shape from the porous layer was subjected to an emerging process from the porous layer to the channels, which manifested itself as a Bunsen flame shape that developed from a “baby” (Fig 4-6 (7)) into an “adult” (Fig 4-6 (8)).

The drainage phase can be defined from DT onwards. The drainage phase of the porous layer can further be divided into two sub-phases: the stable emerging phase, which is the phase in which the liquid water from the porous layer enters the flow channels with a stable adult Bunsen-flame shape, and the avalanche phase in which the liquid water from the avalanche periodically and suddenly squeezes into, accumulates in, and squeezes out of the porous layer.

The drainage phase of the flow channels can be further divided into three sub-phases: bottom stratified drainage, which is the phase from DT to the Tulip Departure Time (TDT as defined in Fig. 4-10); transition drainage, which is the phase from TDT to the Avalanche Exit Time (AET as defined in Fig. 4-10); and the BTB tulips and stratified drainage, which is the phase AET and onwards. In Fig. 4-10, TDT and TET are defined as the instant when the first forward tulip reaches the exit of the outlet channel (outlet as defined in Fig.1) and the instant

when the first BTB tulips flow out of the outlet channel, respectively. ADT and AET are defined as the instant when the water from the first avalanche reaches the outlet and the instant when the water flows out of the outlet channel, respectively.

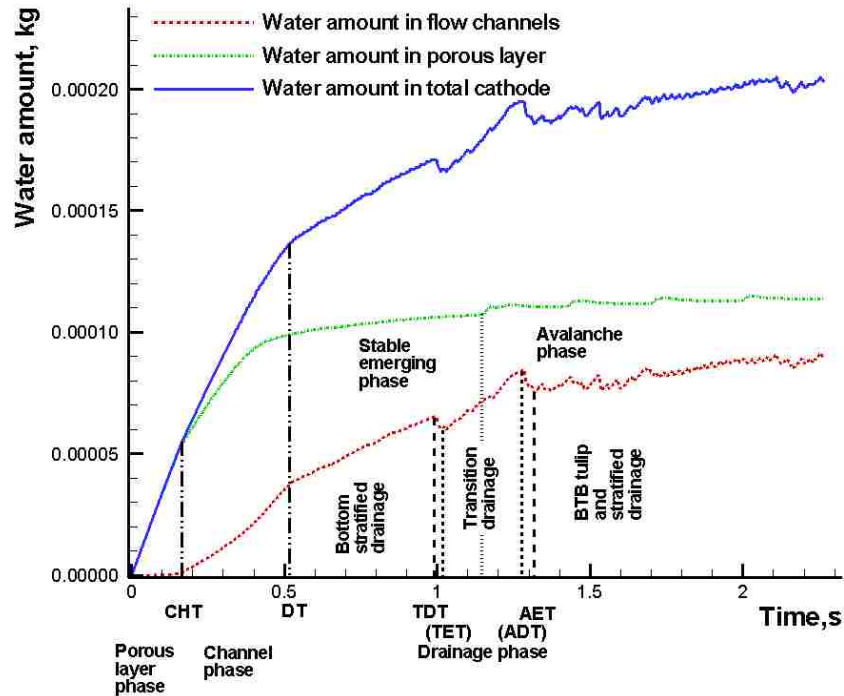


Fig. 4-10 Variation curve of the amount of water as a function of time in the entire domain

(CHT: Cowboy Hat time; DT: Departure Time; TDT: Tulip Departure Time; TET: Tulip Exit Time; ADT: Avalanche Departure Time; AET: Avalanche Exit Time)

From Fig. 4-10, before TDT, the amount of liquid water inside of the flow channels increases with time. Both the porous layer phase and the channel phase exhibited a higher rate of amount of water increasing than that of the stratified drainage phase because some of the liquid water inside of the outlet channel drained during the stratified drainage phase. From TDT to TET, the amount of liquid water inside of the flow channels decreased due to the first BTB tulips draining out. From TET to ADT, the amount of liquid water inside of the channels increased, and a few small fluctuations occurred due to the BTB tulips periodically draining in between. From ADT to AET, the amount of liquid water inside of the flow channels decreased due to liquid water draining from the avalanche. After AET, the liquid water inside of the flow channels gradually approached a “mean-stable state” when the amount of liquid water inside of the flow channels reached a nearly constant mean value, and some small fluctuations occurred due to the periodic interaction between the avalanche and the BTB tulips.

From Fig. 4-10, the total amount of liquid water inside the cathode can be accounted for based on the above descriptions of the amount of liquid water in the porous layer and the flow channels.

4.3 Summary

In this study, the general liquid water flooding process inside of a DHFC cathode with an interdigitated design was investigated by analyzing the air-liquid interaction and by using the VOF method.

(1) The general process of liquid water flooding inside of this type of cathode begins from liquid water generation at the interface of the membrane and the catalyst layer and immediately moves inside of the porous layer based on the flow field design. Then, the liquid water begins to move into the flow channels and accumulates as it moves towards the outlet manifold. Finally, the water accumulates in the outlet manifold and drains through the outlet channel. This process can be classified into three phases: the porous layer phase, the channel phase, and the drainage phase, which is based on the Cowboy Hat Time and the Departure Time.

(2) During the liquid water flooding process, the liquid water can exhibit many different shapes such as a half-mango, half-dumbbell, half-sine-wave, cowboy hat, pancake, Bunsen flame, golden arch, BTB tulip, rivulet shape or a stratified flow pattern. The shape is the result of the interaction between the air and the liquid water as well as the flow geometries.

(3) The liquid water avalanche phenomenon was demonstrated for this type of cathode design, which highlights a potential research direction to improve the water removal performance of this type of interdigitated design.

Chapter 5 Numerical model validations in DMFC anode with a serpentine channel

5.1 Numerical model description

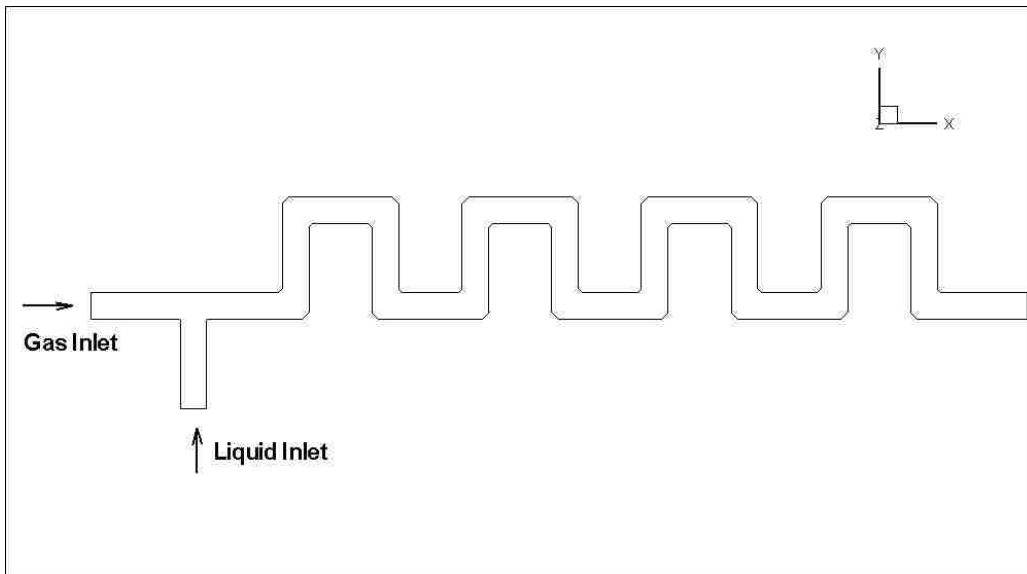


Fig. 5-1(1) Simulation geometry

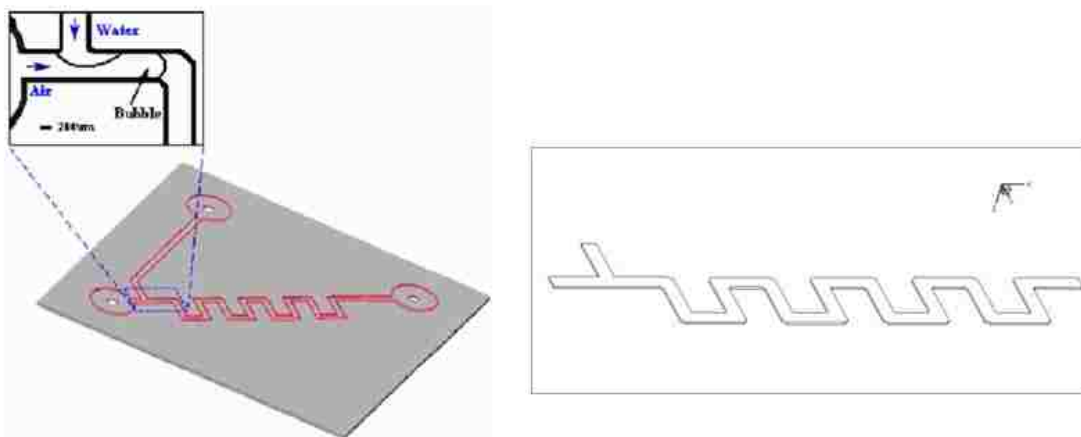


Fig. 5-1(2) Comparison between experiment geometry (left) [57] and simulation geometry (right)

Fig. 5-1 Computational domain of serpentine channel

Before introducing VOF model in DMFC, this numerical method is validated by compare

with a precision and well documented experimental result explored by Xiong et al. [57]. The experimental case is selected as bubble generated and flow in a serpentine channels. The reasons for choosing these experimental results could be list as:

- It is excellent tracked the two phase interface with bubbles phenomenon;
- Generally, it is well documented, although there are some necessary parameters missed, such as channel length;
- This experiment is designed artful with bubbles break up at T-junction process;
- The geometry of serpentine is one kind of fundamental channel designs in PEMFC;
- Different surface tension and viscosity has been experiment studied and could help to validate the model.

The geometry used for comparison is shown in Fig. 5-1. The cross-section of $594\text{ (w)} \times 80\text{ (h)}\ \mu\text{m}^2$ is same in the experiment and simulation. Since the detailed of the channel length didn't documented in the experiment paper, it is set up by analyzed from figures plotted in the experiment.

5.2 Validation with break-up process at T-junction

5.2.1 Boundary conditions and mesh setup

To keep the coincidence of experiment condition and simulation assumption, a no-slip boundary condition is applied to the walls. The air is introduced from the gas inlet channel with a flow rate of $3.5 \times 10^{-9}\text{ kgs}^{-1}$. The water is introduced from the liquid inlet channel with a flow rate of $4.31654 \times 10^{-6}\text{ kgs}^{-1}$. The contact angle value of 140° is selected in the model. The computational domain consisted of 20, 910 cells with a minimum grid size of $1.944 \times 10^{-15}\text{ m}^3$.

5.2.2 Comparison of numerical simulation and experimental visualization with break-up process at T-junction

Fig. 5-2 shows the whole process of the first bubble generation at T-junction from both experiment results (left side) and simulation results (right side). As discussed in experiment study, the bubble generated (break-up) procedure is divided to three phases: gas ligament expansion, gas ligament collapse, and bubble flow out phase. From Fig 5-2, it could be seen the procedure is very similar in the simulation result. Moreover, the modeling results are helpful to analyze the velocity field and interface behaviors as followed.

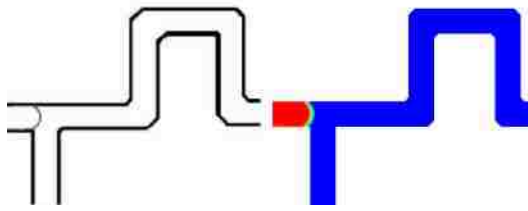


Fig. 5-2 (1)

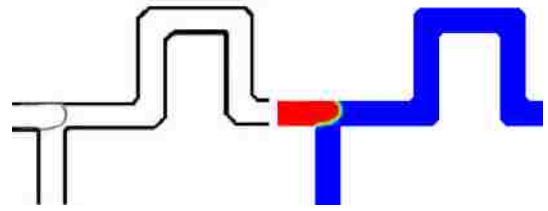


Fig. 5-2 (2)

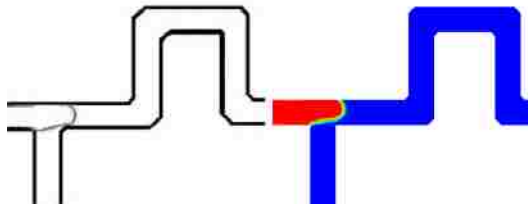


Fig. 5-2 (3)

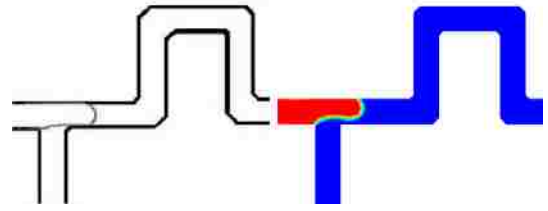


Fig. 5-2 (4)

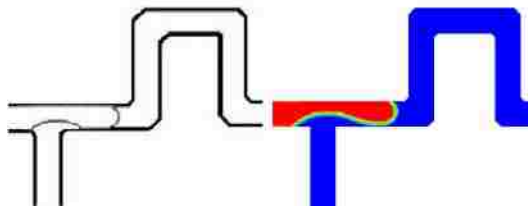


Fig. 5-2 (5)

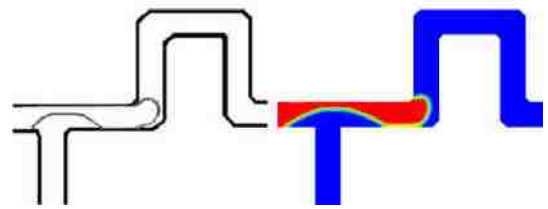


Fig. 5-2 (6)

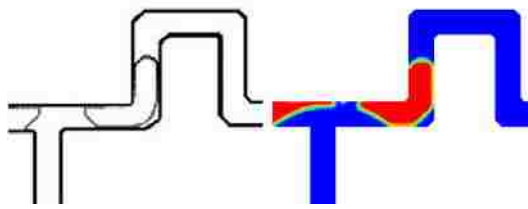


Fig. 5-2 (7)

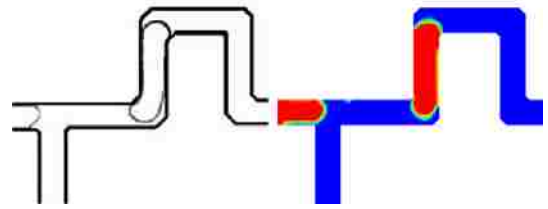


Fig. 5-2 (8)

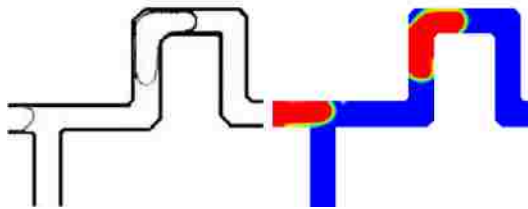


Fig. 5-2 (9)

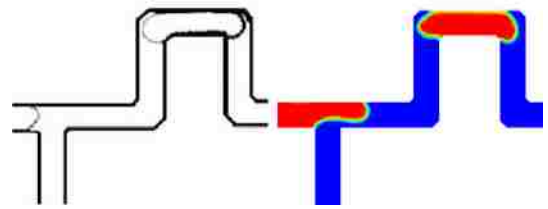


Fig. 5-2 (10)

Fig. 5-2 Validation with bubble generated in T-junction
The experiment results come from Xiong et al.'s work [57]

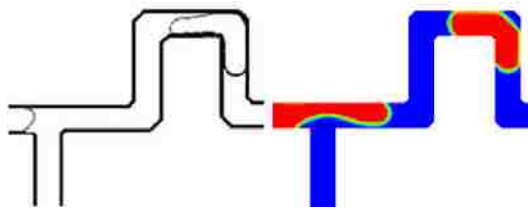


Fig. 5-2 (11)

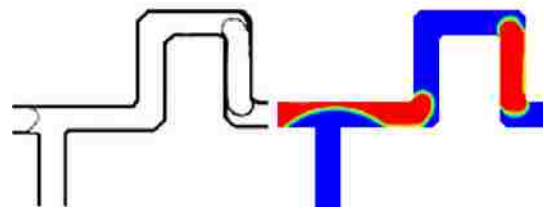


Fig. 5-2 (12)

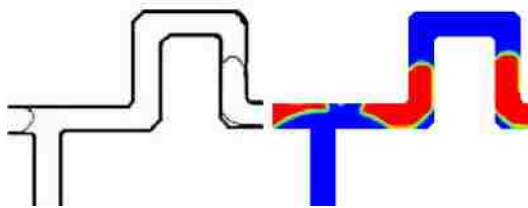


Fig. 5-2 (13)

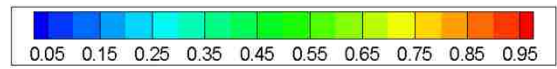


Fig. 5-2 (14) Color scheme legend of gas volume fraction

Fig. 5-2-continue Validation with bubble generated in T-junction
The experiment results come from Xiong et al.'s work [57]

As shown in Fig 5-2 (1 - 7), after gas comes in from the left inlet with constant flow rate, a bubble moves slowly pushing by the gas supplied from the gas inlet and facing the resistance of the liquid which existed in the channel from the beginning. The head of the bubble keeps a convex round shape by the reason of the contact angle of the wall on the side. As the gas slug arrives the T-junction of the two inlet channel, liquid comes from the other inlet channel pushing it to the top side of the horizontal channel. The gas shapes a neck above the perpendicular channel where bearing the shear force come from it. This sub-process is so called gas ligament expansion. The gas ligament bars up the opening of the liquid and results increasing the shear force. Thus, the neck, the only transport ligament of the gas gets slimmer and finally be cut off by the liquid. This process named gas ligament collapse while the leaving bubble born and begin to travel in the serpentine channel drives by velocity filed and bubble flow out phase begin The Fig 5-2 (8 - 13) shows the leaving bubble travel in the first inverted U shape of the serpentine channel. In Fig 5-2 (8) and Fig 5-2 (12), the bubble appears an "S" shape by attach the top side of the lower channel and the bottom side of the higher channel, apparently, it is trying to take the shortest route to get the outlet. Same reason for the bubble shapes in Fig. 5-2 (9 - 11) and Fig. 5-2 (13), it always attach the inner side of the converted U channel.

5.2.3 Velocity field of break-up process

Fig 5-3 shows the gaseous bubble behavior during the break-up process with velocity field. Fig 5-3 (1) shows that liquid flow smoothly before the bubble arrive the T-junction. Because of the corner effects, the velocity vector is intensive around inner corner and unconsolidated near the external corner. The velocity in liquid phase around the T-junction are enlarged when the gas slug trying to cover the exit of liquid inlet channel as shown in Fig 5-3 (2). With the liquid inlet channel is blocked, liquid accumulated at the exit of liquid inlet channel and push the air to the top wall and the “neck” shaped (as presented in Section 5.2.1). As shown in Fig 5-3 (6), when the gas bubbles approach to but not touch the wall of the channel, stress on the water will strongly increased in the gap. After the ligament collapsed, strong velocity of liquid forms a vortex between the bubble released and the gas slug in the gas inlet channel. The interaction between the airflow and the liquid water can provide strong shear stress and can fragment some of the air on the gas-water interface into small bubbles. Theses small bubbles rolled up by the vortex and consumed by the gas-water interface again.

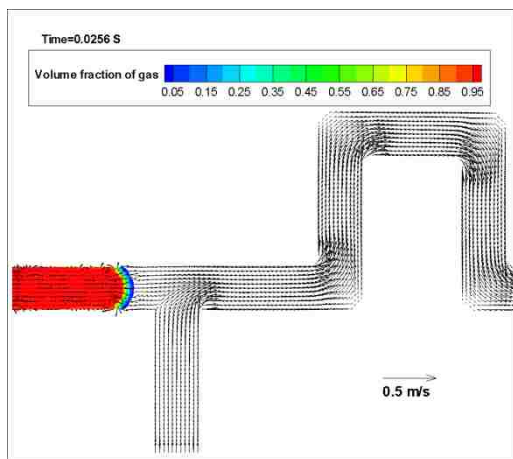


Fig 5-3 (1) $t = 0.0256$ s

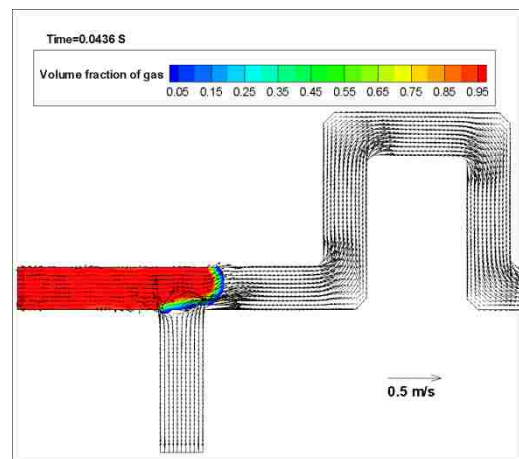


Fig 5-3 (2) $t = 0.0436$ s

Fig. 5-3 Gas volume fraction and velocity vector in T-junction

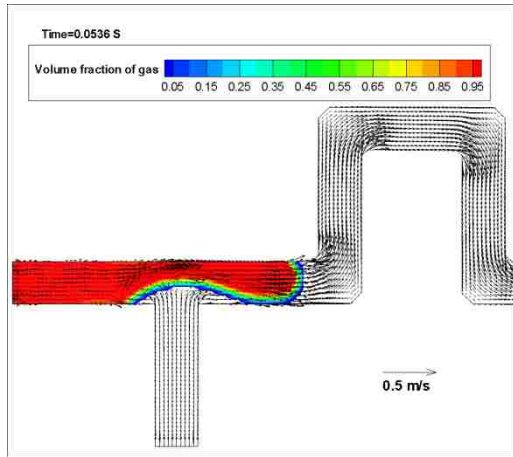


Fig 5-3 (3) $t = 0.0256$ s

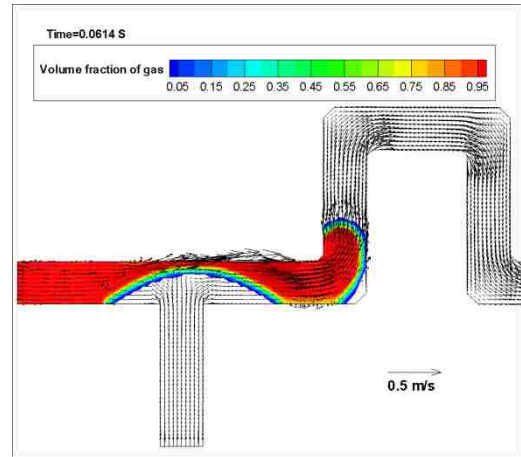


Fig 5-3 (4) $t = 0.0256$ s

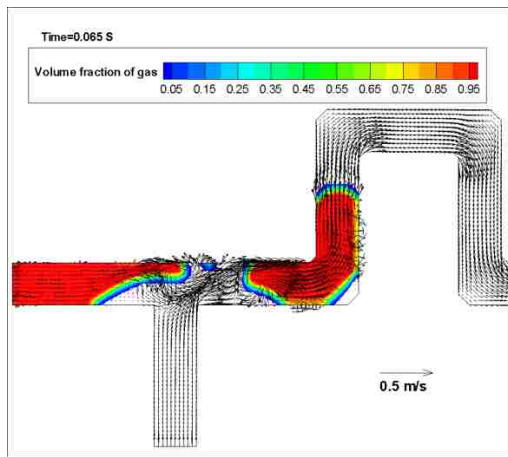


Fig 5-3 (5) $t = 0.0650$ s

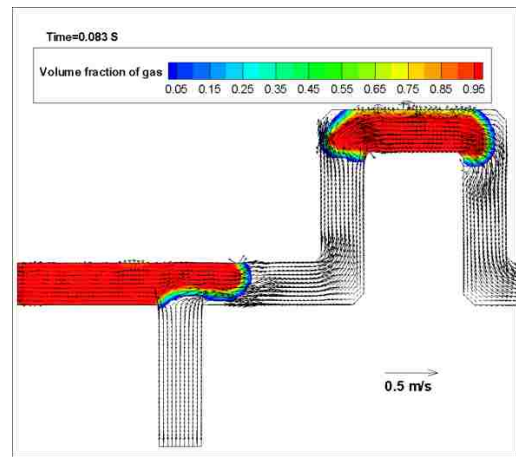


Fig 5-3 (6) $t = 0.0830$ s

Fig 5-3-continue Gas volume fraction and velocity vector in T-junction

5.2.4 Pressure fields

Fig. 5-4 and Fig. 5-5 show the figures of volume fraction of gas and pressure distribution in the serpentine channel. The pressure drops gradually along the channel from inlet to outlet. Since the outlet pressure is assume to keep at relative pressure of zero (atmosphere) as boundary condition, no change for pressure around the outlet. The pressure around the inlet is changing from 7000 Pa to 5500 Pa in the three figures of different instant ($t = 0.0148$ s, $t = 0.1480$ s and $t = 0.1840$ s)).

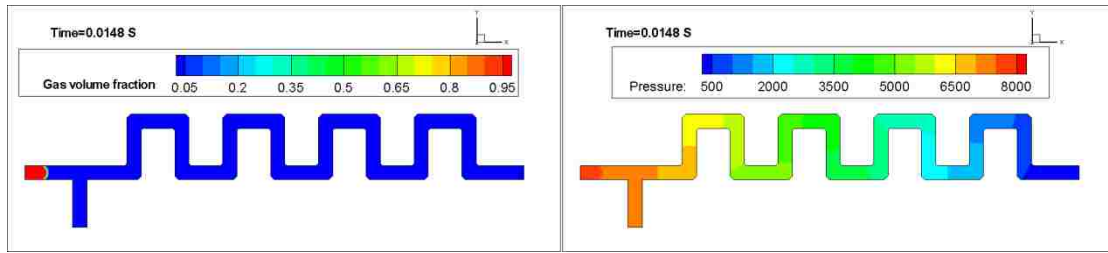


Fig. 5-4 (1) $t = 0.01480$ s

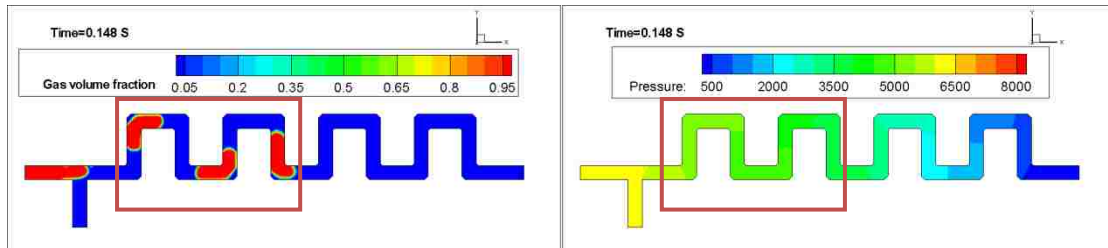


Fig. 5-4 (2) $t = 0.1480$ s

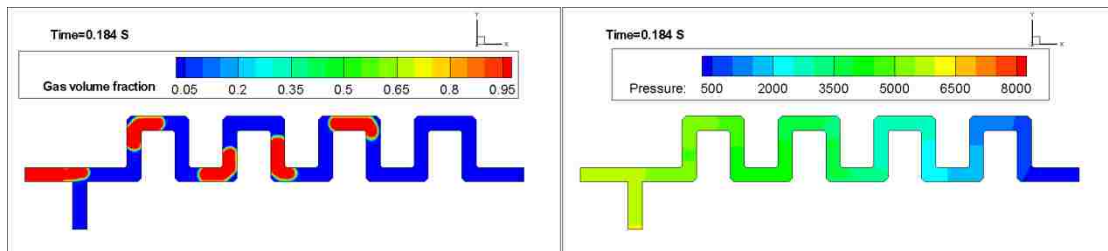


Fig. 5-4 (3) $t = 0.1840$ s

Fig. 5-4 Volume fraction of Gas and Pressure distribution in serpentine channel (Figures on left column show volume fraction of gas and figure on right side show pressure distribution on (1) $t = 0.0148$ s (2) $t = 0.1480$ s (3) $t = 0.1840$ s)

Fig. 5-5 shows the pressure and velocity field of first and second inverted U shape channel in the red blocks shown in Fig. 5-4 (2). The velocity of the gas phase is stronger in the middle of the bubble. The bubble which locates at the corner tends to flow straight results the strong velocity towards to the wall.

Although the pressure tends to decrease along the channel, the pressure inside the gas bubbles is higher than inside the liquid and results an interesting phenomenon that the velocity vector orientated from the lower pressure field to the high pressure field. This phenomenon proved the effects from the capillary pressure difference across the interface between liquid and gas with the surface tension. Since the contact angle is set as 140° in gas phase, which results the gas slug in the tube shows convexity surfaces on both head and tail side, which means higher pressure inside the gas balanced by the surface tension. The balance between the surface tension forces and pressure could be expressed as Young-Laplace equation (Equation (15) in Section 3.2.3).

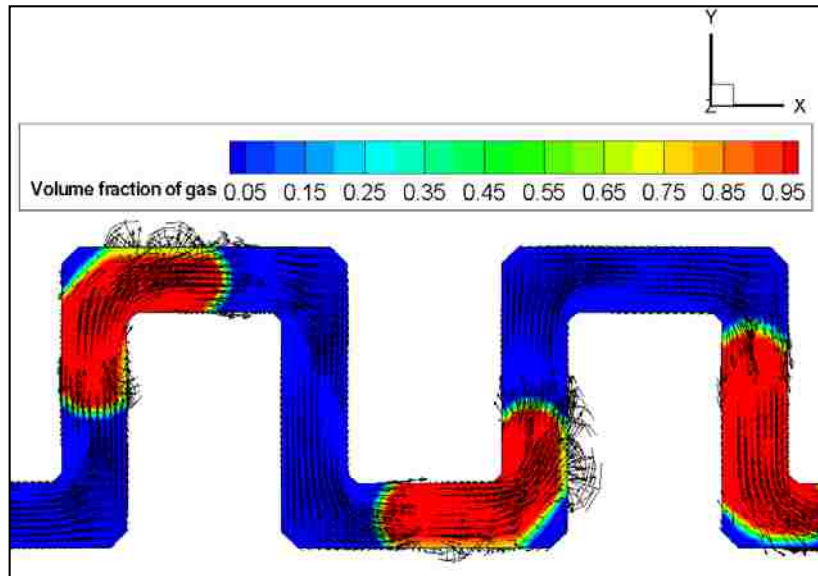


Fig. 5-5 (1) Volume fraction of gas with velocity vector of first two inverted U shape channels

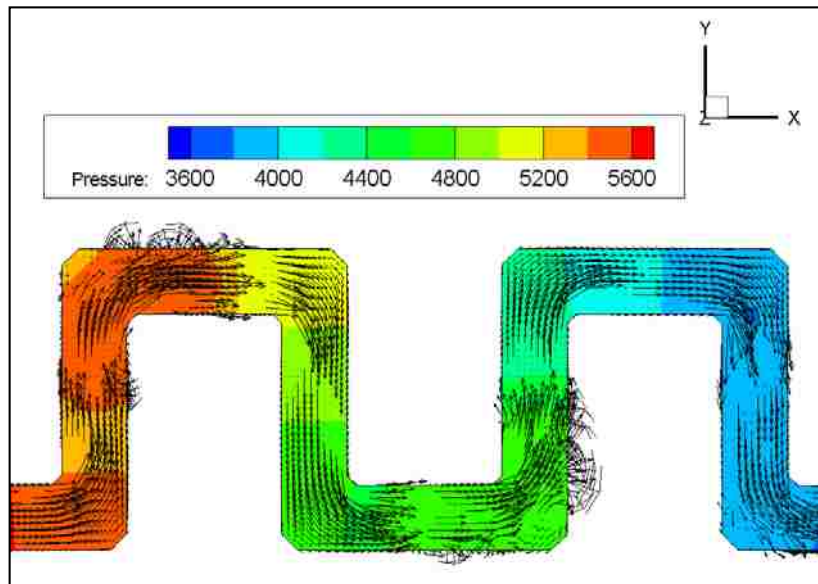


Fig. 5-5 (2) Pressure distribution with velocity vector of first two inverted U shape channels

Fig. 5-5 Volume fraction of gas and pressure drop with vector of first two inverted U shape channels

5.3 Effects of surface tension and liquid viscosity

5.3.1 Effects of surface tension

The two figures in Fig. 5-6 show the results of two simulation experiment. Same boundary condition (liquid/gas inlet velocity, contact angle, etc.) is adopted in these two cases except

surface tension coefficient: Liquid velocity is 0.273 m/s, gas velocity is 0.0546 ms⁻¹. The surface tension is selected as experiment measured value 0.072 Nm⁻¹ and 0.037 Nm⁻¹ separately. Also the liquid density is a little different between two cases (1000 kgm⁻³ in the second case and 998 kgm⁻³ in the first case) in order to keep identical with the experiments.

Fig. 5-6 shows the simulation results at the exactly same time point. With same flow rate of two kinds of fluid, the lower surface tension results asunder bubbles. After 89.5 ms, the first two small bubbles combined together and form a tadpole-like shape as presented in the experiment paper. Since the results for the experiment is not detailed enough, the analysis below only represents the modeling results.

As the surface tension could be defined as property of the surface of a liquid that allows it to resist an external force [63], the asunder bubbles is reasonable. While the bubble generated in the T-junction as presented in previous section, the shear force from the liquid inlet channel would be easier to cut the gas slug with lower surface tension.

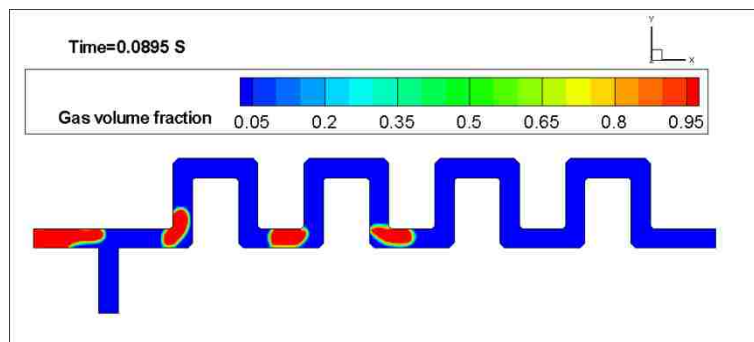


Fig. 5-6 (1) Gaseous volume fraction with surface tension $\sigma = 0.072 \text{ Nm}^{-1}$

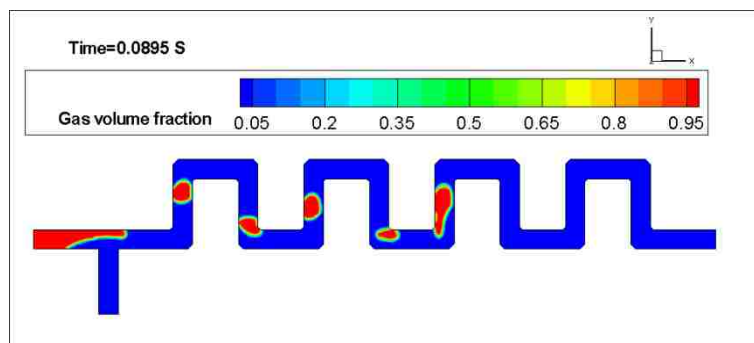








Fig. 5-6 (2) Gaseous volume fraction with surface tension $\sigma = 0.037 \text{ Nm}^{-1}$

Fig. 5-6 Gaseous volume fraction of two cases with different surface tension

5.3.2 Effects of viscosity

As shown in Table 5-1, three cases are simulated to explore the effect of liquid viscosity and experimental results are compared with. The velocities of gas or liquid in three cases are identical separately as 0.182 ms^{-1} for gas and 0.091 ms^{-1} for liquid. The liquid viscosity is increase from $0.00119 \text{ Pa}\cdot\text{s}$ for first case to $0.00731 \text{ Pa}\cdot\text{s}$ for the third one. The liquid viscosity of $0.00268 \text{ Pa}\cdot\text{s}$ is chose in the second case. The figures in the last column of Table 5-1, the simulation results show that the bubble generated in the case with higher liquid viscosity is shorter. Same result obtained in the experiment study as shown in forth volume.

Table 5-1 Effect of liquid viscosity

Velocity of gas inlet (ms^{-1})	Velocity of liquid inlet (ms^{-1})	Liquid viscosity ($\text{Pa}\cdot\text{s}$)	Bubble shape presented in experimental results [58]	Simulation results
0.182	0.091	0.00119		
0.182	0.091	0.00268		
0.182	0.091	0.00731		

5.4 Summary

In this chapter, a serpentine channel with a liquid inlet and a gas inlet is adopted as geometry to investigate the VOF model application in bubbles behavior by analyzing the gas-liquid interaction.

(1) The whole process of the bubble generation and break up in the T-junction from the simulation result is exactly similar with the experiment investigation.

(2) By analyzing the velocity field and pressure distribution from the simulation results, some phenomena such as the corner effect and the surface behavior of bubbles are explained.

(3) The effect of the surface tension is studied with two simulation models with similar

condition except different surface tension. The results show a tadpole-like shape as same as presented in the experimental study.

(4) The effect of liquid viscosity is explored by three similar simulation models. With the liquid viscosity increase, the bubble length along the channel is decrease because of the stronger shear force from the liquid.

Chapter 6 Interface phenomenon in a DMFC anode with a parallel design

6.1 Computational geometry

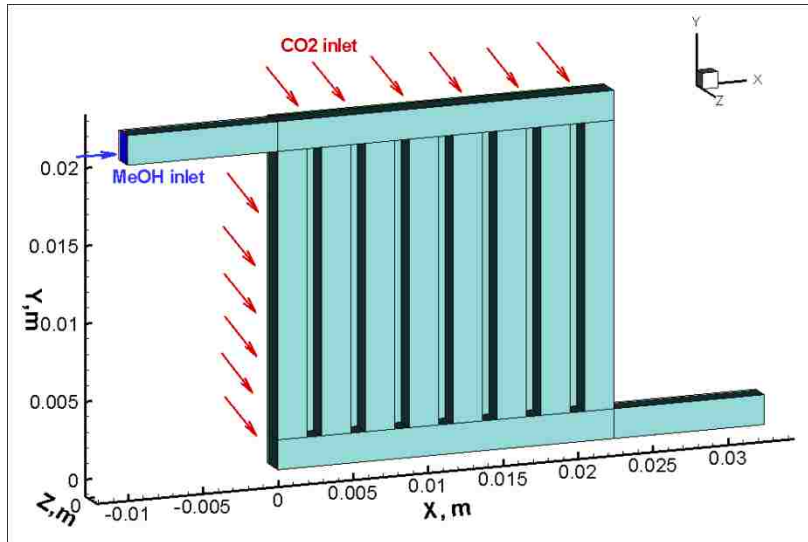


Fig. 6-1 Computational geometry

The numerical simulation domain represents as full-scale anode side geometry of a single DMFC. Fig. 6-1 illustrates the schematic of the numerical simulation domain, which contains liquid flow channels and a porous layer. The channels are in a parallel pattern with eight channels (1.92 mm width, 1.5 mm depth) and 1 mm width rib between adjacent channels. The 0.3 mm porous layer represents both CL and GDL attaches to the 500 mm² effective area. These are the typical dimensions of a fuel cell component [42].

6.2 Boundary conditions and mesh setup

In order to modeling a practical DMFC anode, the experiment conditions in the study of Wang et al. [42] are adopt as simulation parameters in this numerical model. A no-slip boundary condition is applied to the walls. The liquid methanol inlet is set with a flow rate of 0.000327779 kgs⁻¹ (the flow is normal to the inlet boundary), and the liquid water inlet (back surface of the porous layer shown in Fig. 6-1) is set with a flow rate of 3.8×10^{-7} kgs⁻¹. The pressure outlet is applied at the outlet boundary. The contact angles, which are set in the side walls of channels, upper walls of channels and the rest of walls, are 115°, 115° and 110°, respectively. The porosity of the porous layers used in this model is 0.2. The accelerate model

is adopt with 10 times of methanol inlet flow rate.

Table 6-1 Parameters and properties used in the model

Property	Value
Cell temperature	75 °C
CO ₂ Density	1.52575 kgm ⁻³ [64]
MeOH Density	945.516 kgm ⁻³
CO ₂ viscosity	1.73 × 10 ⁻⁵ Pa·s
MeOH viscosity	0.000368233 Pa·s
Surface tension coefficient	0.06128 Nm ⁻¹
MeOH inlet mass flow rate	0.000327779 kg·s ⁻¹
CO ₂ mass flow rate	3.8 × 10 ⁻⁸ kgs ⁻¹
Contact angle for the upper wall of channel	115°
Contact angle for the side wall of channel	115°
Contact angle for the other walls	110°

In the experiment done by the Wang et al. [42], the methanol is preheated to 85 °C, and decrease 10 °C because heat loss in the fuel cell. So the methanol solution and CO₂ inside anode is assume to keep on 75 °C in the simulation. The detailed fluid property value and boundary condition are shown in Table 6-1. Accelerate model is adopt as 10 times accelerate of CO₂ generated.

The computational domain consisted of 258,912 cells with a minimum grid size of 1.267×10⁻¹² m³. The mesh size in the porous layer was 0.16 mm × 0.16 mm × 0.05 mm. The mesh size in the flow channel was 0.16 mm × 0.16 mm × 0.15 mm. This computational mesh setup is considered to be effective and reasonable according to the study in Chapter 4 because this model select same methodology to explore the two phase (liquid and gas) phenomena.

6.3 Results and discussion

6.3.1 Gas CO₂ behavior inside DMFC anode with parallel design

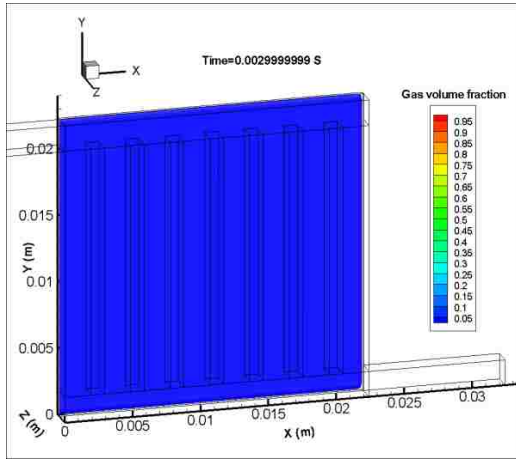


Fig. 6-2 (1) $t = 0.003$ s

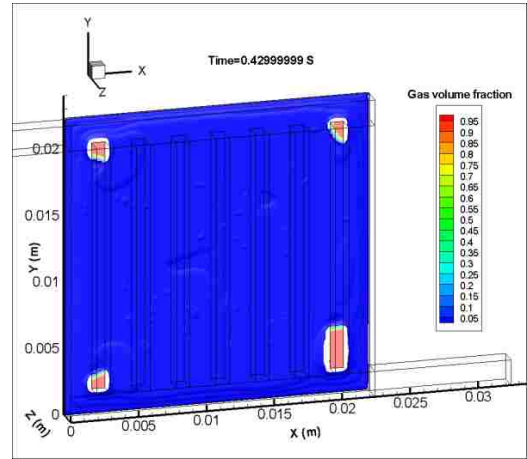


Fig. 6-2 (2) $t = 0.430$ s

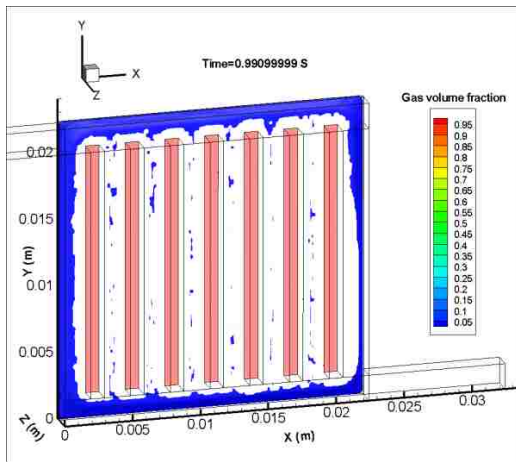


Fig. 6-2 (3) $t = 0.991$ s

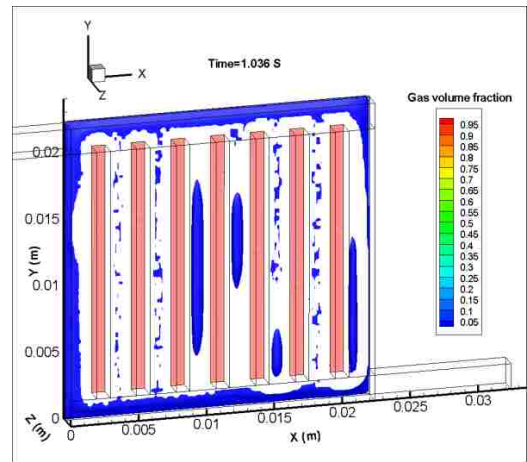


Fig. 6-2 (4) $t = 1.036$ s

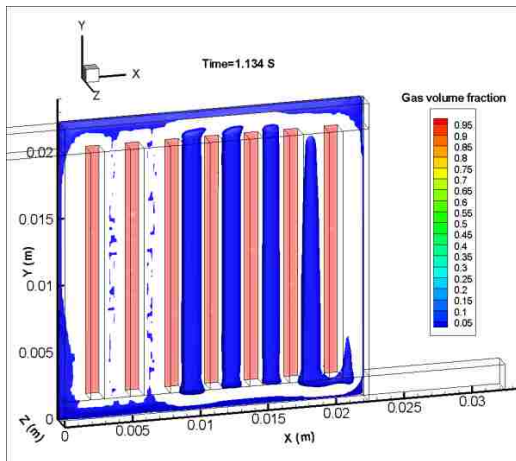


Fig. 6-2 (5) $t = 1.134$ s

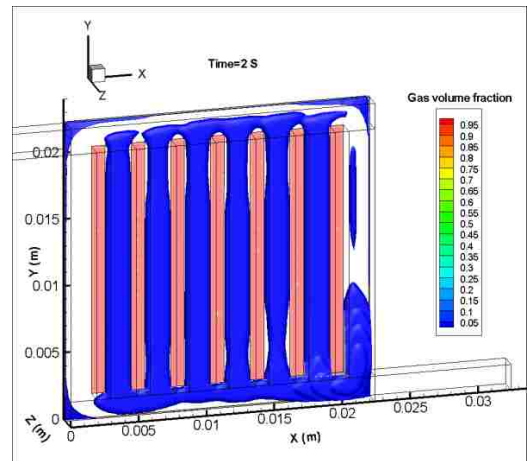


Fig. 6-2 (6) $t = 2.000$ s

Fig. 6-2 General process of gas CO₂ flooding

Fig. 6-2 (1)-(6) shows the main process of gas movement over time for some selected time instants. The general process of liquid water removal can be divided into the following sub-processes.

(1) CO_2 is supplied from the back surface of the porous layer by a constant flow rate to simulate the CO_2 generation through electro-chemical reaction as shown in Fig. 6-2 (1)

(2) This supplied CO_2 first enters the porous layer and accumulated from the four corners until the gas touch the interface under the nearest land of the corners as shown in Fig. 6-2 (2).

(3) As shown in Fig. 6-2 (3 - 4), CO_2 emerges in the channel after the whole porous layer is almost fulfilled. The emerging process first occurs in the third and fourth channel from left side in the figure.

(4) The gas CO_2 in the channels merges to bigger bubbles in every channel. Details will be discussed in later section.

(5) The gas CO_2 merges to a slug in every channel. Before moving out from outlet channel, the gas CO_2 converges in the bottom right corner and moves out by bubbles.

6.3.2 General distribution of CO_2 in the porous layer

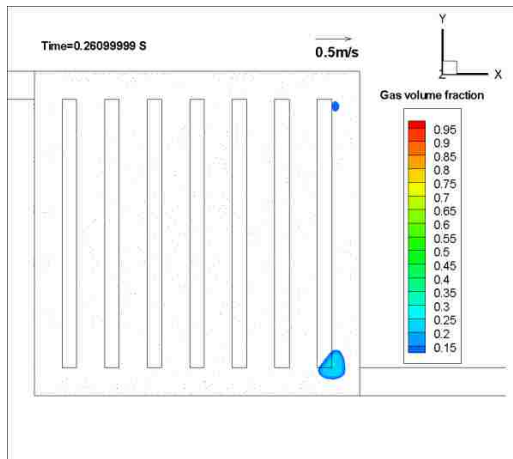


Fig 6-3 (1)

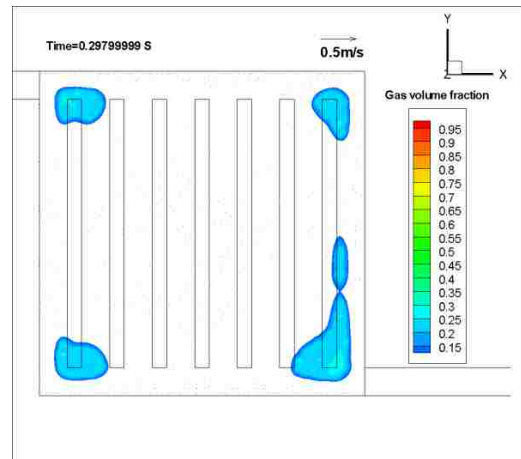


Fig 6-3 (2)

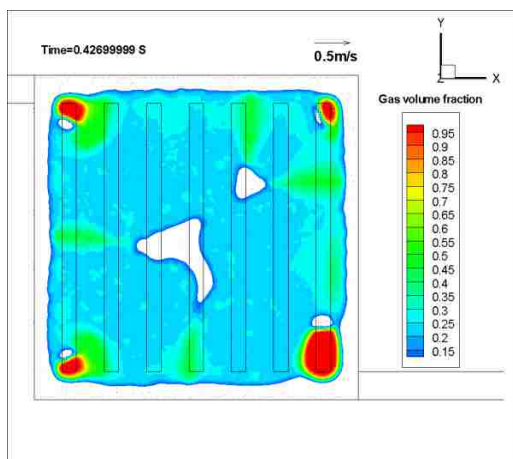


Fig 6-3 (3)

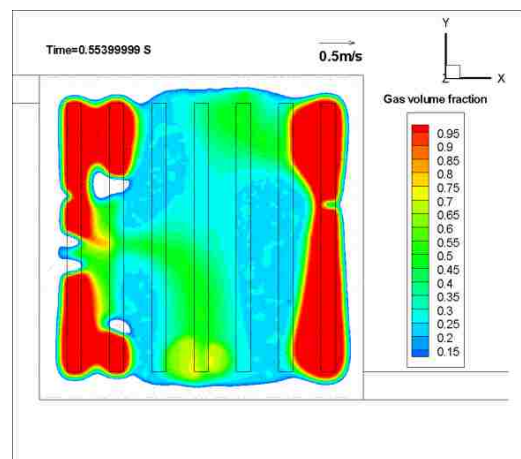


Fig 6-3 (4)

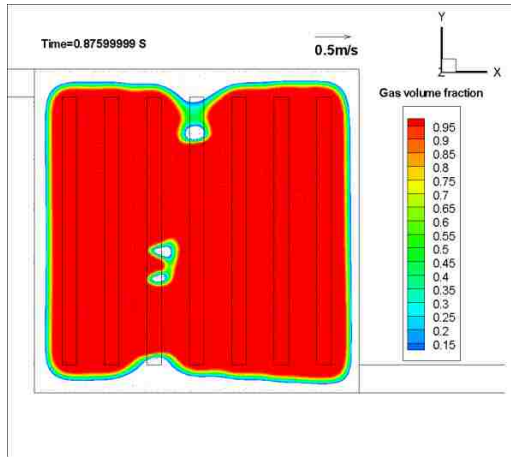


Fig 6-3 (5)

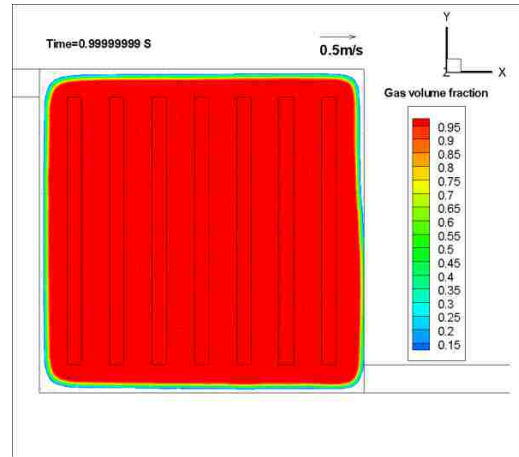


Fig 6-3 (6)

Fig. 6-3 CO₂ distribution at Z = -0.00015 m

The Fig 6-3 (1 - 6) shows the CO₂ distribution on the cross section from the porous layer domain (with projective channel edges) at Z = -0.00015m which is in the middle of porous layer. This series of figures are chose to explain the main process of the gas CO₂ behavior inside the porous layer domain. As shown in the Fig 6-3, after gas CO₂ inlet from the back surface, the CO₂ moves around with in.

(1) At first, the CO₂ first concentrate in the corner near outlet channel of porous layer domain as shown in Fig 6-3 (1).

(2) Later, more CO₂ accumulated in four corners and spread inside the porous layer domain. The CO₂ bubble which shows up first at the corner near outlet spread fastest along the last channel.

(3) Every two bubbles locate in left side and right side join together first. And the bigger bubbles keep spread and merge together encircle the center of the porous layer.

(4) With more gas accumulate, the four corners of porous layer is fulfilled first and finally fulfilled the whole porous layer.

6.3.3 CO₂ emerging process and the vortexes phenomenon in the channels

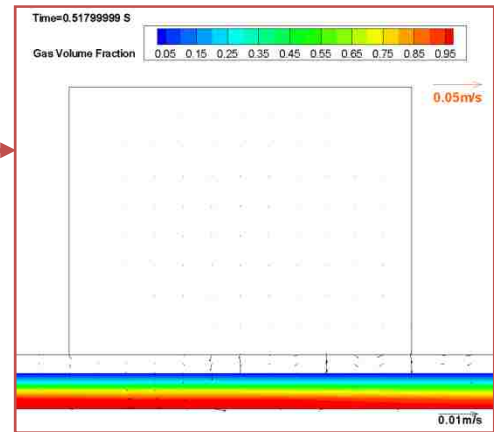
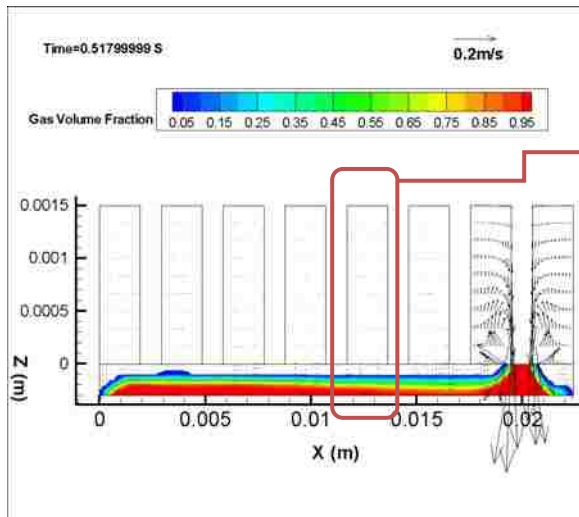


Fig. 6-4 (1) $t = 0.518$ s

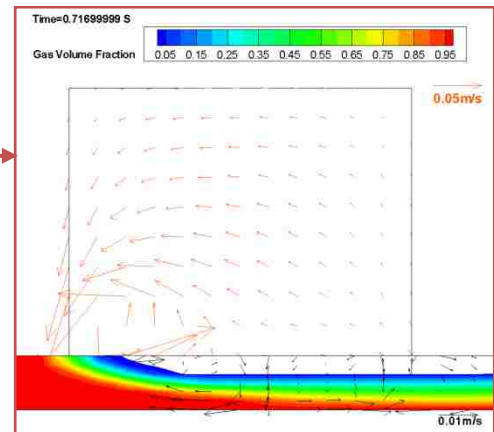
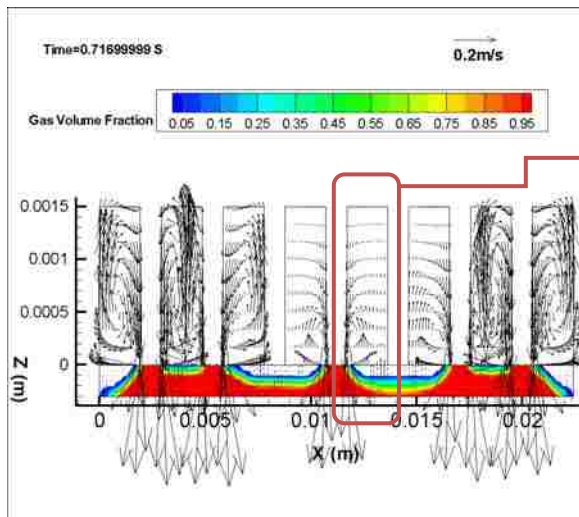


Fig. 6-4 (2) $t = 0.717$ s

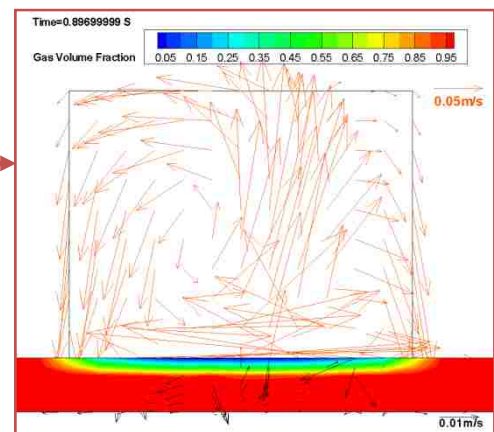
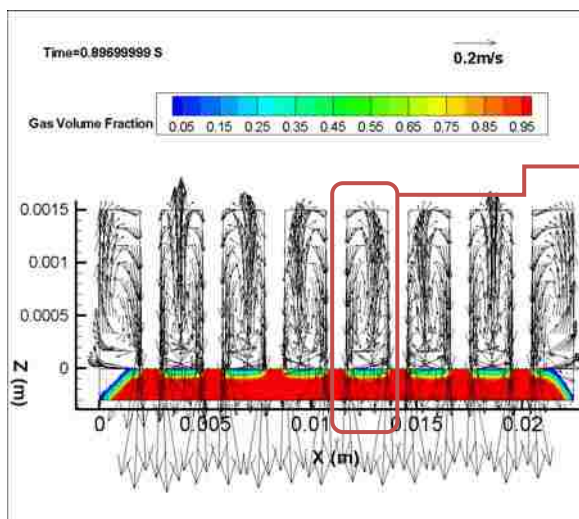


Fig. 6-4 (3) $t = 0.897$ s

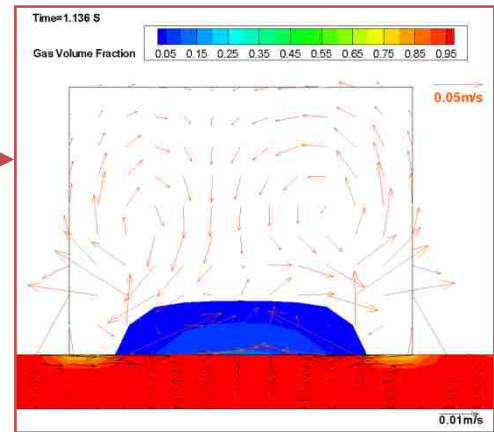
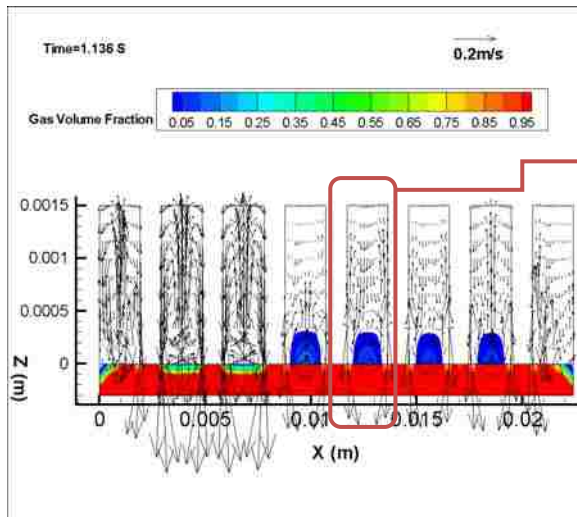


Fig. 6-4 (4) $t = 1.136 \text{ s}$

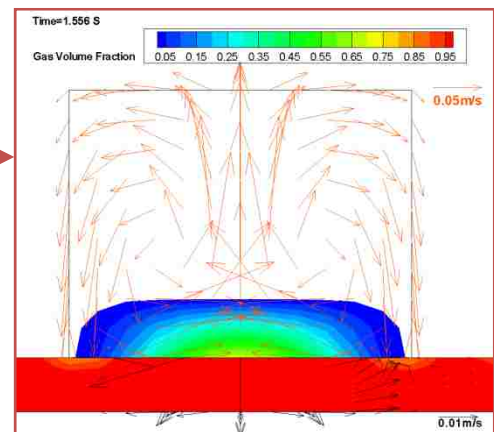
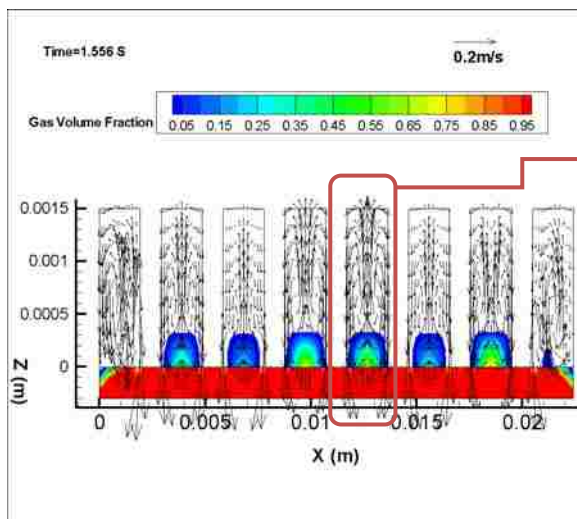


Fig. 6-4 (5) $t = 1.556 \text{ s}$

Fig. 6-4 General process by which liquid water emerges into the channels

The Fig. 6-4 shows the velocity vectors and VOF on the X-Z planes located at $Y = 0.01118 \text{ m}$, the middle of the channel direction (along the Y axis) with different reference velocity vectors, by which, the interface of liquid methanol and CO_2 could be explained as followed:

(1) Before CO_2 emerging in the flow, the methanol fulfilled the flow channels, and flow to the outlet either through channel to the outlet manifold and move out from the outlet channel or squeeze into the porous layer and flow to the outlet joint and move out.

(2) After CO_2 released from the back surface of porous layer, the interface between two fluids rise higher with wave motions until the crest of the CO_2 wave attach to the land between last two channels. This blocks the paths of the liquid methanol flow from last two channels to the outlet joint through porous layer and hence causes stronger velocity in them as shown in Fig. 6-4 (1).

(3) With more CO₂ comes in, the surface of CO₂ rose close to the interface between channels and porous layer. CO₂ attaches to the other two lands bottom as shown in Fig. 6-4 (2), more blocks on the paths of liquid flow cause strong vortexes in the channels.

(4) When there is only one side under the channel is blocked by the gas, the flow field in each channel forms one vortex which orientates to leave the blocks to the middle of the channel at the bottom side of the channel and lift by stop of the other wall of the channel.

(5) When the CO₂ is almost fulfill the porous layer, both sides of channel are blocked by the gas, a Dean Vortex shows up in the channels as shown in Fig. 6-4 (3).

(6) After the CO₂ emerging into the channels, the Dean Vortex is inverted and distorted because the emerging CO₂ push the methanol to the side of the channel at the bottom side. .

(7) The strength of Dean Vortexes decrease and the direction invert again after the CO₂ occupied whole interface between channels and porous layer.

6.3.4 CO₂ volume amount inside computational domains

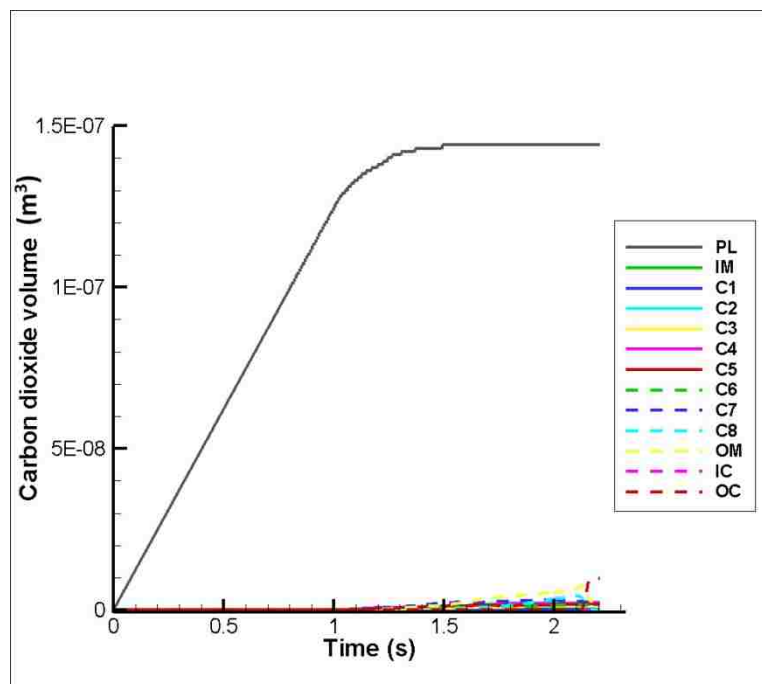


Fig 6-5 (1) The gas CO₂ volume amount in every part of computational domain

Fig. 6-5 CO₂ volume amount in different part of the computational domain

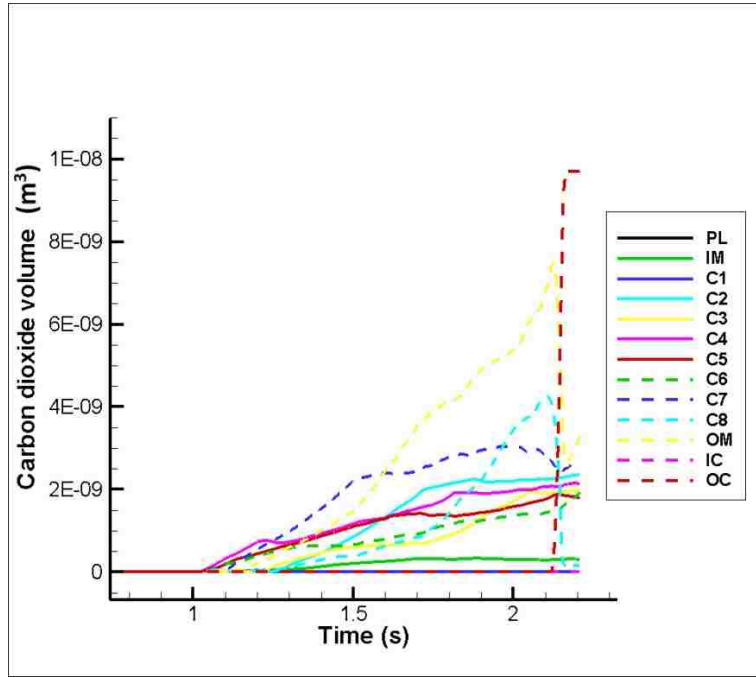


Fig 6-5 (2) CO₂ volume amount in every channel

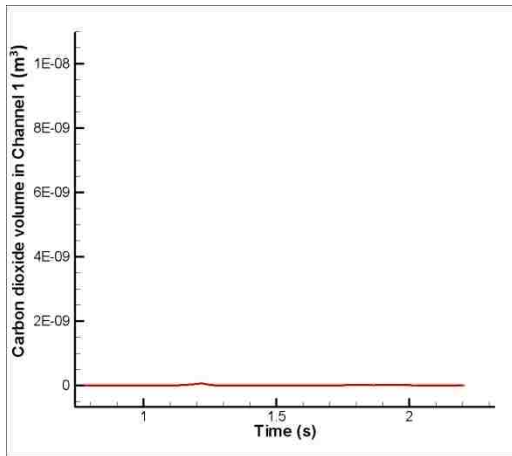


Fig 6-5 (3) in first channel

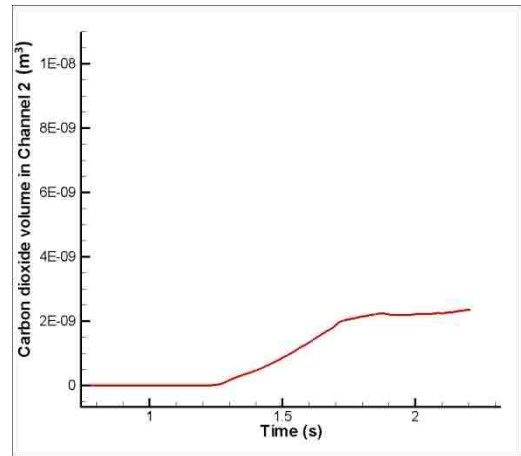


Fig 6-5 (4) in second channel

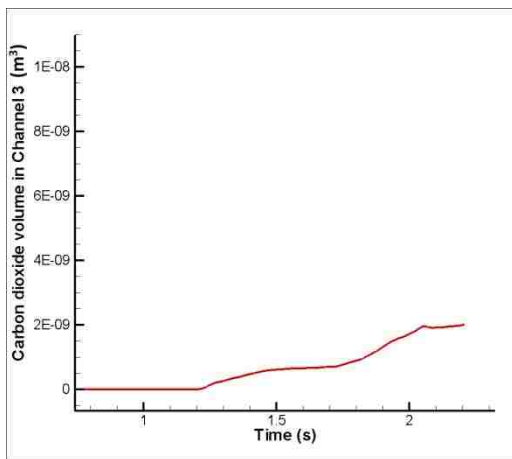


Fig 6-5 (5) in third channel

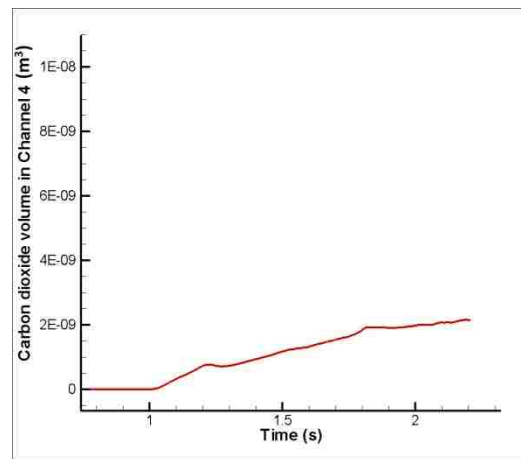


Fig 6-5 (6) in fourth channel

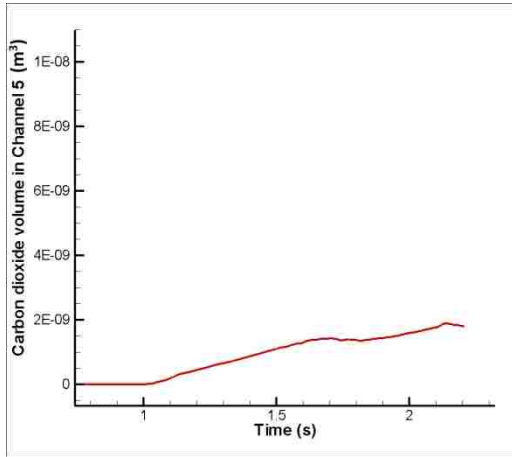


Fig 6-5 (7) in fifth channel

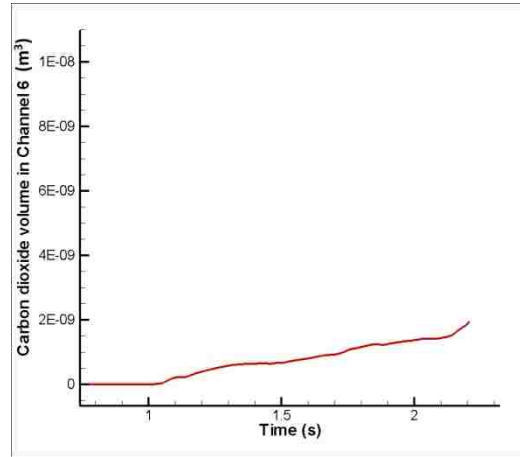


Fig 6-5 (8) in sixth channel

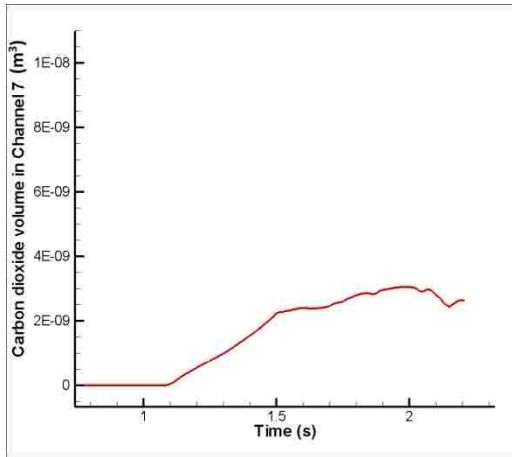


Fig 6-5 (9) in seventh channel

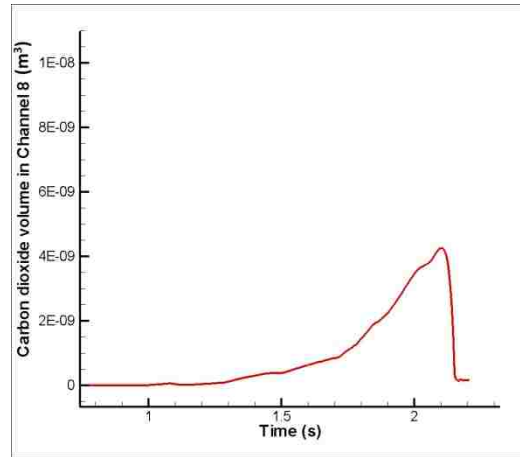


Fig 6-5 (10) in eighth channel

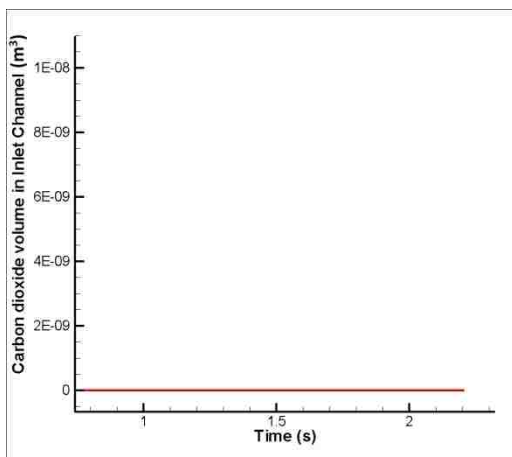


Fig 6-5 (11) in inlet channel

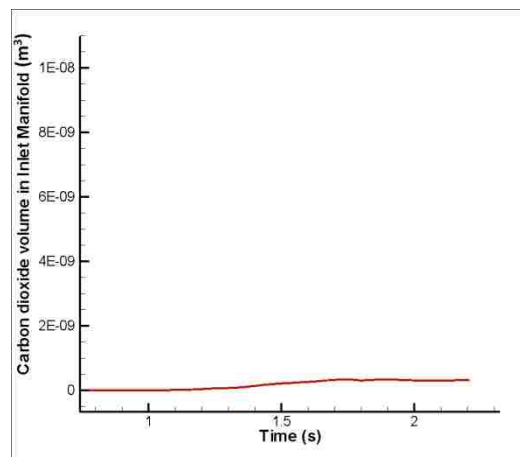


Fig 6-5 (12) in inlet manifold

Fig 6-5-continue CO₂ volume amount in different part of the computational domain

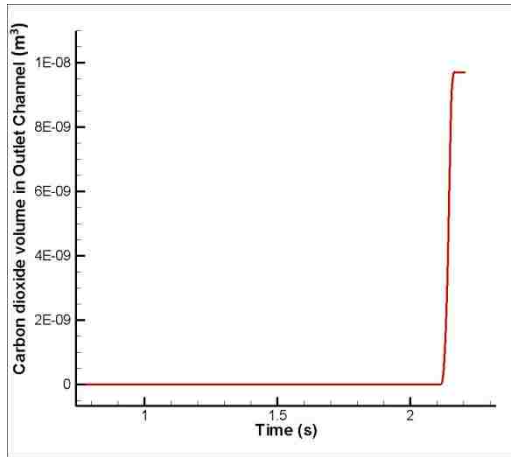


Fig 6-5 (13) in outlet channel

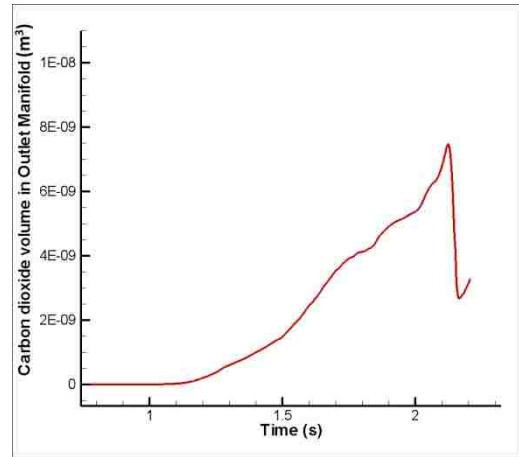


Fig 6-5 (14) in outlet manifold

Fig 6-5-continue CO₂ volume amount in different part of the computational domain

Fig 6-5 shows the gas CO₂ volume amount in different part of the computational domain collected by UDF function of FLUENT, by which the real amount of gas phase could be explored clearly.

Fig 6-5 (1) shows the CO₂ volume amount in all sub-domains. The CO₂ amount in porous layer increase linearly before the instant of $t = 1.1$ s, at the neighboring time point, the gas CO₂ emerge in the channel. The increasing rate decreases from this instant and close to zero. In other words, the CO₂ amount tends to keep constant.

To explore the CO₂ amount change in each channel, Fig 6-5 (2) enlarged the channels part and Fig 6-5 (3 - 14) show them separately.

In the whole computational period, there is almost no CO₂ emerging except at around $t = 1.2$ s, some lower volume fraction CO₂ emerging, but back to porous layer quickly forced by surface tension.

From Fig 6-5 (4 - 9), the second channel to the seventh channel shares similar situation that the CO₂ amount increase gradually after the CO₂ begin to emerge in the channels.

From Fig 6-5 (11 - 12), the CO₂ in inlet channel and inlet manifold keeps littleness.

Through Fig 6-5 (10, 13 - 14), one outflow phenomenon could be explained. Before the gas moving out, the gas gather together in the bottom right corner. After enough gas accumulated, the gas moves out in forms of a bubble.

6.3.5 Pressure drop versus time

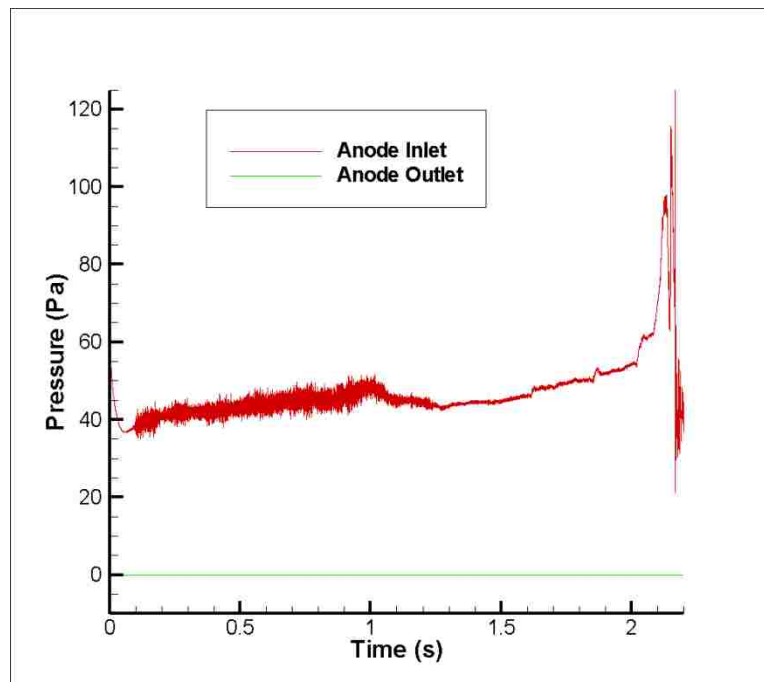


Fig. 6-6 (1) Pressure of Methanol inlet and anode outlet

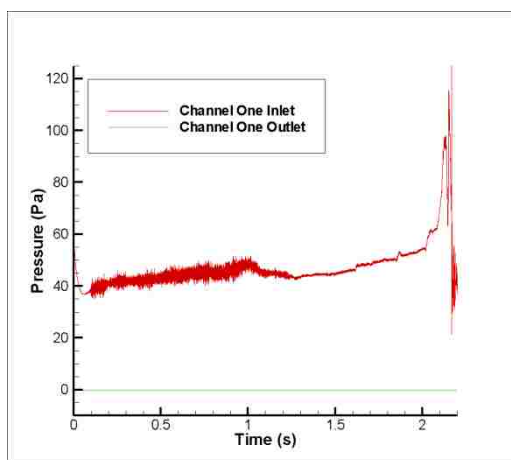


Fig. 6-6 (2) Pressure of first channel inlet and outlet

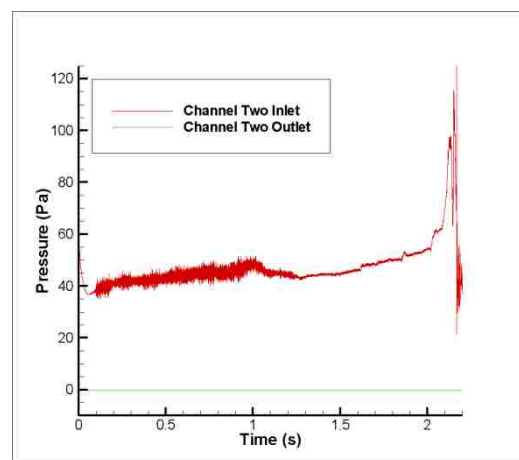


Fig. 6-6 (3) Pressure of second channel inlet and outlet

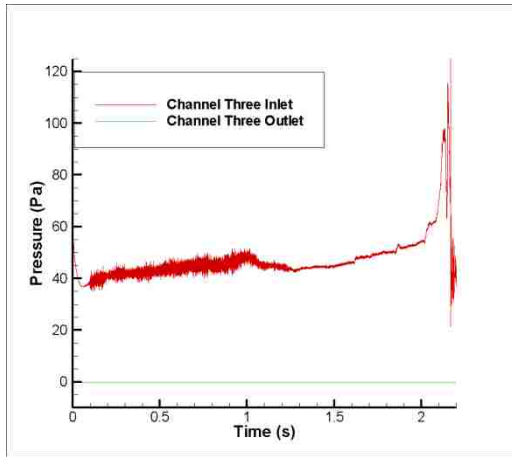


Fig. 6-6 (4) Pressure of third channel inlet and outlet

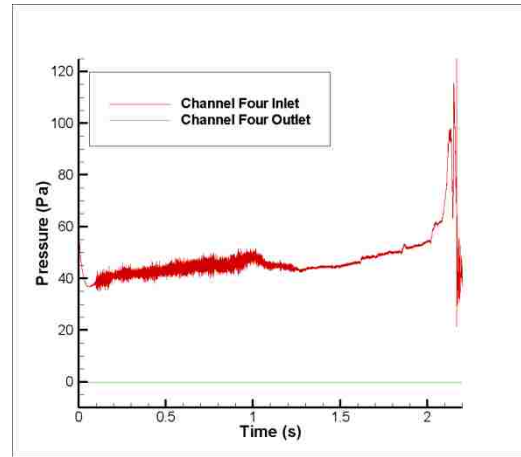


Fig. 6-6 (5) Pressure of fourth channel inlet and outlet

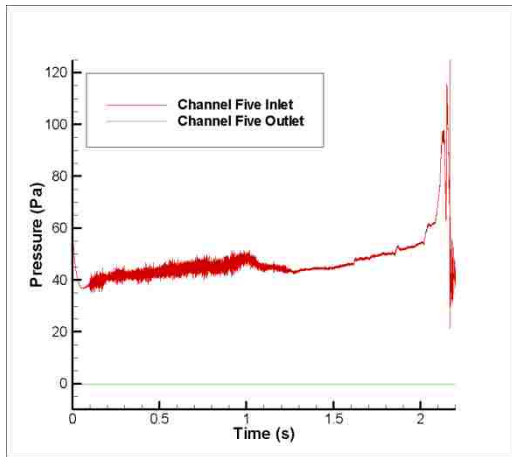


Fig. 6-6 (6) Pressure of fifth channel inlet and outlet

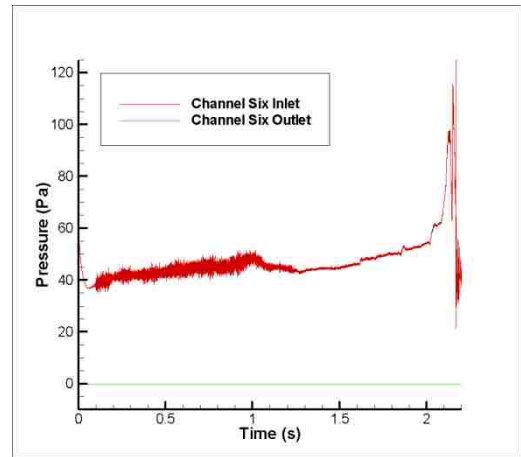


Fig. 6-6 (7) Pressure of sixth channel inlet and outlet

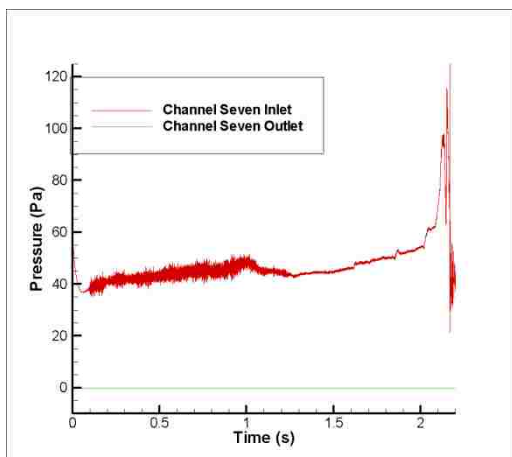


Fig. 6-6 (8) Pressure of seventh channel inlet and outlet

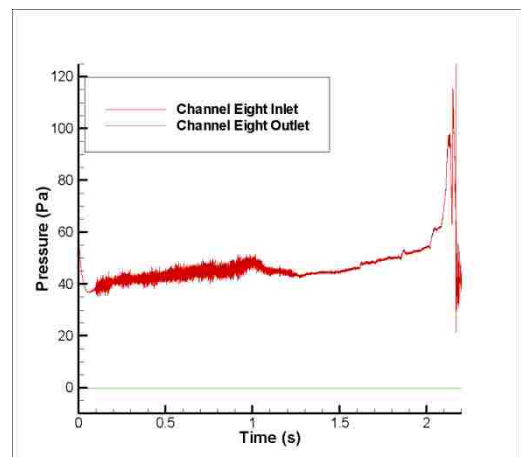


Fig. 6-6 (9) Pressure of eighth channel inlet and outlet

Fig. 6-6 Pressure of each sub-domain inlet and outlet

Fig. 6-6 shows the pressure of the inlet and outlet of each channel collected by UDF function of FLUENT. The inlet and outlet in each channel shares very similar pressure. In the first second period, fluctuations are observed centered with a gentle increasing curve from 40 Pa to 50 Pa. At the instant around $t = 1.1$ s when the CO_2 emerge in the channels, the centre line of the fluctuation decrease a little and the amplitude of fluctuation decrease too. After the instant around $t = 1.2$ s, the centre curve of the fluctuation increase slowly and forms four stages when the curve increase quickly and finally get 60 Pa. After $t = 2.1$ s, the gas moving out from the outlet channel and plug up the outlet as presented in last section, the amplitude of pressure fluctuation sharp increased. When the bubble moves out and the methanol could be discharged from outlet again, the pressure drops correspondingly. The peak of the pressure reaches 125 Pa and the trough reaches 20 Pa. After the drastic fluctuation of pressure, the amplitude regressions to the original level of fluctuation. The pressure at the outlet keeps at 0 (atmosphere).

6.4 Summary

In this numerical study, the general CO_2 distribution inside of a DMFC anode with a parallel design was investigated by tracking the gas-liquid interface using the VOF method.

(1) The CO_2 introduced from the back surface of porous layer accumulated in the corner of the porous layer first.

(2) The CO_2 starts emerging in the fourth, fifth and seventh channel, and gathered in the corner near outlet channel.

(3) With the CO_2 emerging from porous layer to the channel. Different orientation vortices are found in the channel depends on how the CO_2 blocks the paths of liquid flow under the land between each two channels.

(4) The quantitative analysis with CO_2 volume amount and pressure drop in the DMFC anode is presented. The CO_2 moving out process could be expressed from the CO_2 volume amount, and pressure changed accordingly.

(5) Although this numerical model is effective to analyze the CO_2 distribution in the whole domain, compare with the practical DMFC anode phenomena, there is a flaw for the bubbles generation process in the GDL because of the uniform porosity assumption. A successful different simplified numerical model should cater for this diversity. This improvement will discuss in following chapters.

Chapter 7 Interface phenomena in DMFC anode with innovative GDL-1 and static contact angle

7.1 Computational domain

In order to approaches available to achieve the bubbles generation process in channel as practical DMFC anode, an innovative GDL geometry is developed in this chapter. To optimal use of computer resources and save computing time, the geometry is designed to simulate part of the practical DMFC.

As shown in Fig. 7-1, a schematic of the computational domain that contains the anode with a parallel flow design and innovational GDL and a CL attached to it. CO₂ bubble assumed generated with constant rate from the back surface of the CL and flow in along the z-direction into CL domain. The Methanol solution inlet, outlet are shown in Fig. 7-1, two parallel channels (1.92 mm width, 1.5 mm depth, 1 mm rib width in between) with connected by inlet channel and outlet channel (1 mm width, 7.84 mm length) are applied. On the MEA side, a 0.1 mm thickness GDL was attached to the channel, small paths (0.3 mm × 0.3 mm × 0.1 mm) are used to represents the holes on GDL, the other part of GDL is designed a porous media with porosity of 0.2. A 0.1 mm CL is attached to GDL with porosity of 0.2.

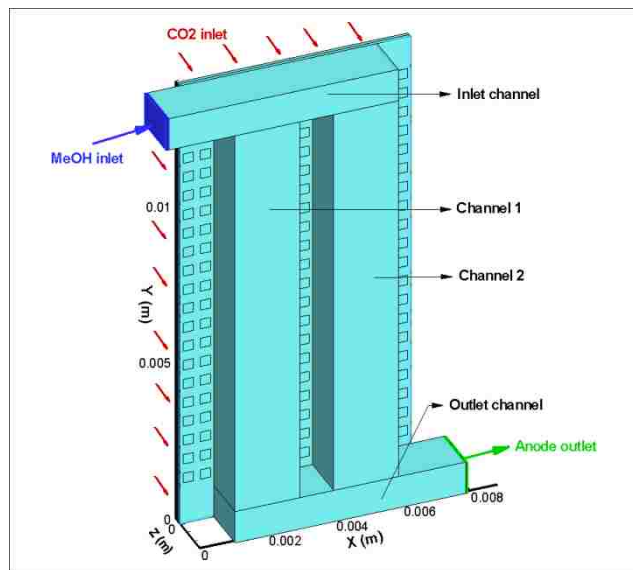


Fig. 7-1 Computational domain of a DMFC anode with parallel design with an innovation GDL

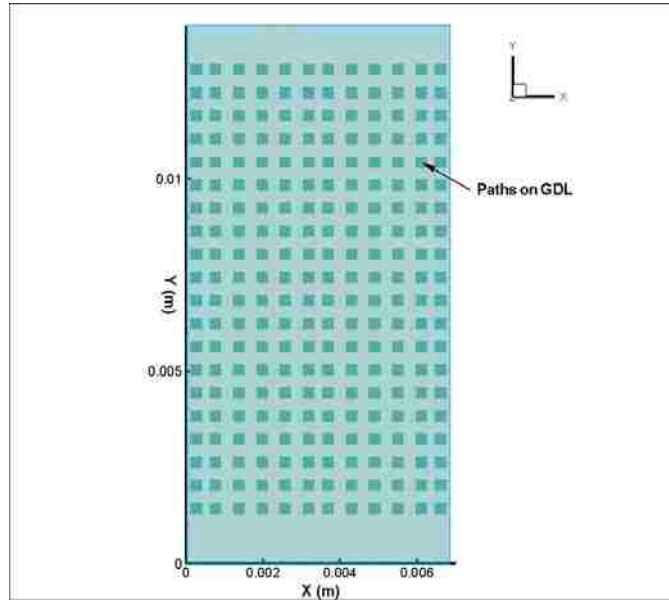


Fig. 7-2 Innovation gas diffusion layer (GDL)

7.2 Fluid properties and boundary conditions

In the experiment done by the Wang et al. [42], the methanol is preheated to 85 °C, and decrease 10 °C because heat loss in the fuel cell. So the methanol solution and CO₂ inside anode is assume to keep on 75 °C in the simulation. The detailed fluid property value and boundary condition are shown in Fig. 7-1. Accelerate model is adopt as 100 times accelerate of CO₂ generated.

Table 7-1 Parameters and properties used in the model

Property	Value
Cell temperature	75 °C
CO ₂ Density	1.52575 kgm ⁻³ [64]
MeOH Density	945.516 kgm ⁻³
CO ₂ viscosity	1.73 × 10 ⁻⁵ Pa·s
MeOH viscosity	0.000368233 Pa·s
Surface tension coefficient	0.06128 N/m
MeOH inlet mass flow rate	6.27801 × 10 ⁻⁵ kg·s ⁻¹
CO ₂ mass flow rate	7.27988 × 10 ⁻⁸ kg·s ⁻¹
Contact angle for the upper wall of channel	115°
Contact angle for the side wall of channel	115°
Contact angle for the other walls	110°

7.3 Mesh setup

The computation domain is meshed into 116,320 cells with a maximum volume of $1.575 \times 10^{-12} \text{ m}^3$ and a minimum volume of $3.33 \times 10^{-13} \text{ m}^3$ for each cell. The grid size measures approximately $1 \times 10^{-4} \text{ m}$ in both the X- and Y-directions, whereas the dimensions in the Z-direction are $1.5 \times 10^{-4} \text{ m}$ in the gas flow channel domain and $3.3 \times 10^{-5} \text{ m}$ in the porous layer domain.

7.4 Results and discussion

7.4.1 Validation with a practical DMFC anode



Fig. 7-3 (1)



Fig. 7-3 (2)

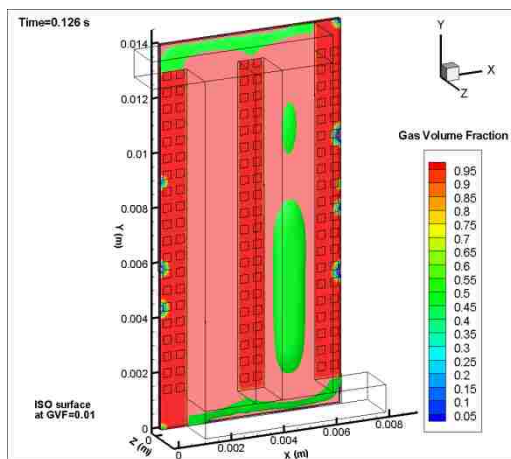


Fig. 7-3 (3)

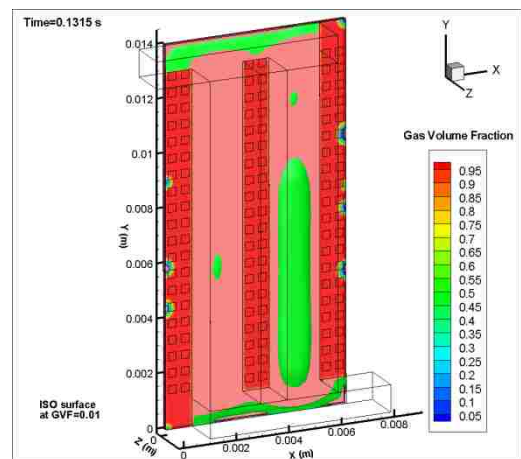


Fig. 7-3 (4)

Fig. 7-3 Comparison of numerical simulation (3–4) and experimental visualization (1–2)

The experiment results selected from the study of Wang et al. [42]

To validate this numerical model, the visualization experiment study by Wang et al. [42] is selected to compare the numerical and the experiment results. By this model with uneven gas diffusion layer, the simulation results are closer to the phenomena in experimental results. As shown in Fig. 7-3, there are bubbles in the middle of the channel with different sizes. And also, the bubbles emerged in the channels presented similar shape – gas slug along the channel with round heads on both sides.

7.4.2 General CO₂ flooding process

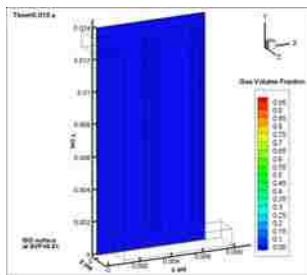


Fig. 7-4 (1-I)

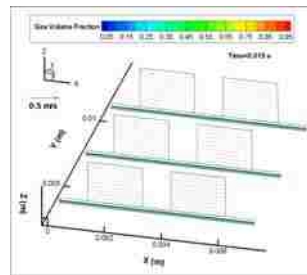


Fig. 7-4 (1-II)

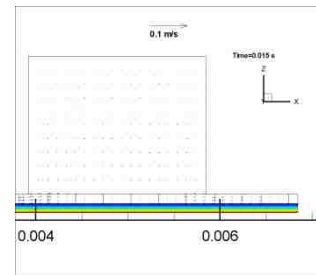


Fig. 7-4 (1-III)

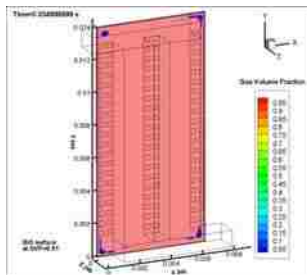


Fig. 7-4 (2-I)

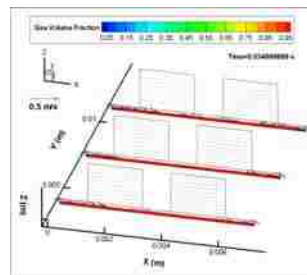


Fig. 7-4 (2-II)

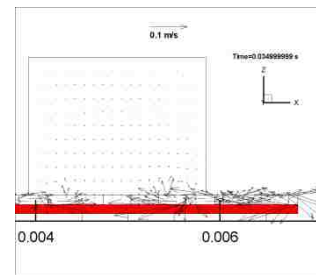


Fig. 7-4 (2-III)

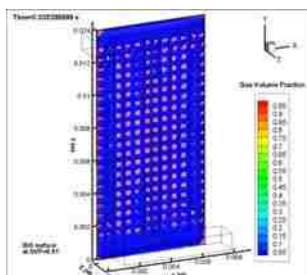


Fig. 7-4 (3-I)

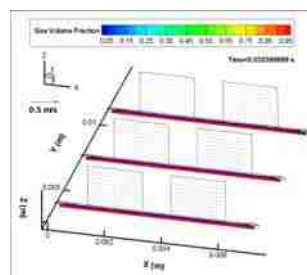


Fig. 7-4 (3-II)

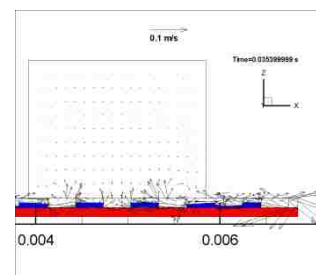


Fig. 7-4 (3-III)

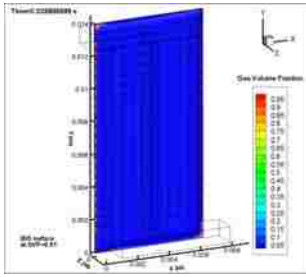


Fig. 7-4 (4-I)

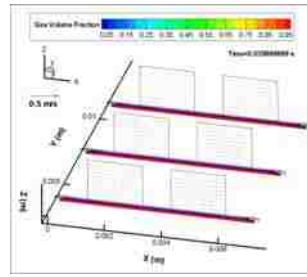


Fig. 7-4 (4-II)

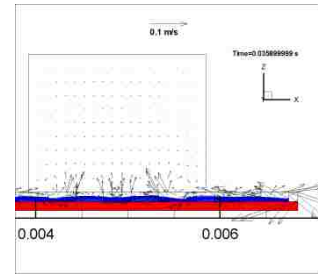


Fig. 7-4 (4-III)

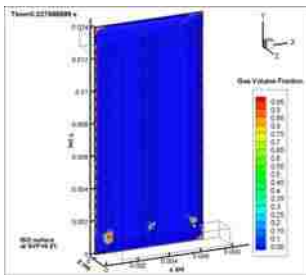


Fig. 7-4 (5-I)

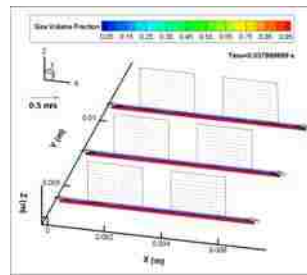


Fig. 7-4 (5-II)

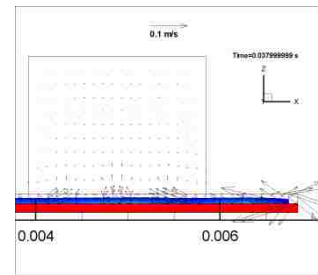


Fig. 7-4 (5-III)

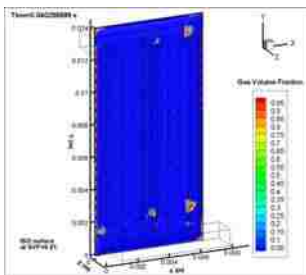


Fig. 7-4 (6-I)

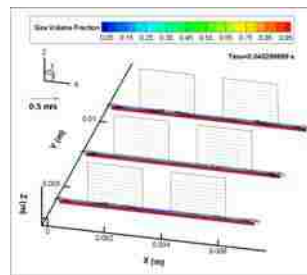


Fig. 7-4 (6-II)

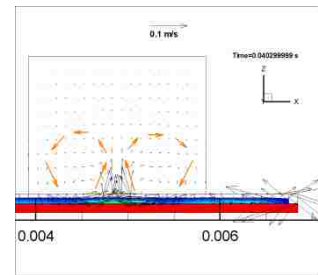


Fig. 7-4 (6-III)

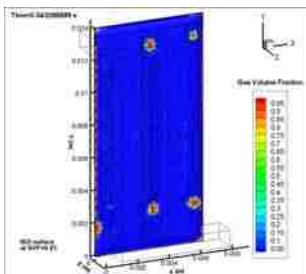


Fig. 7-4 (7-I)

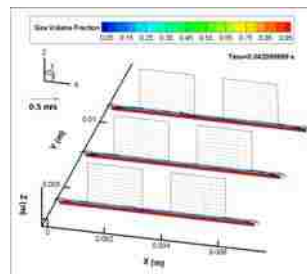


Fig. 7-4 (7-II)

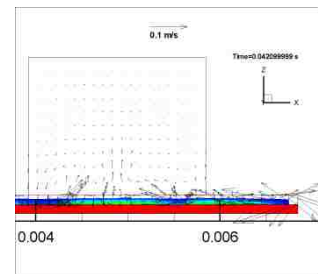


Fig. 7-4 (7-III)

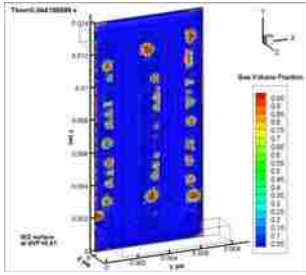


Fig. 7-4 (8-I)

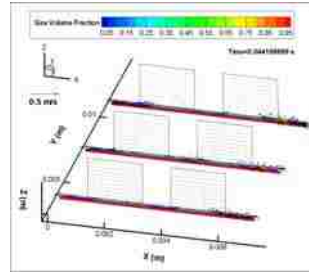


Fig. 7-4 (8-II)

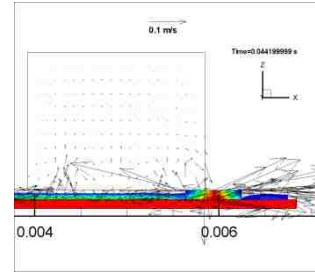


Fig. 7-4 (8-III)

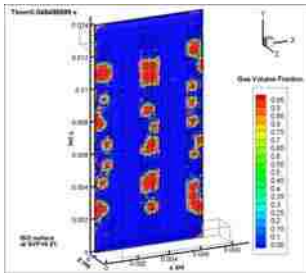


Fig. 7-4 (9-I)

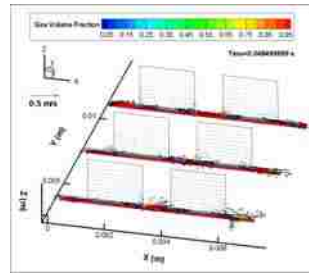


Fig. 7-4 (9-II)

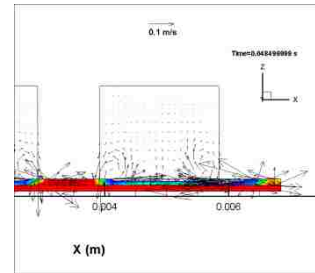


Fig. 7-4 (9-III)

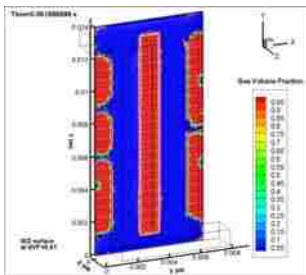


Fig. 7-4 (10-I)

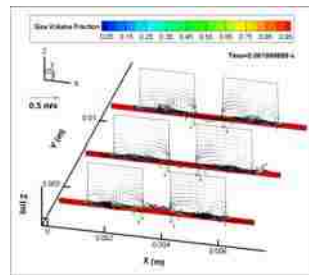


Fig. 7-4 (10-II)

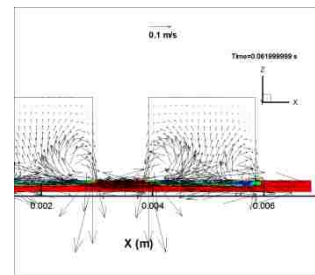


Fig. 7-4 (10-III)

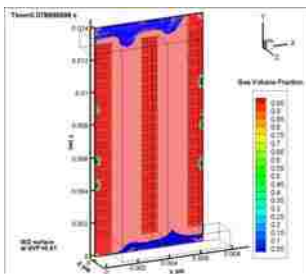


Fig. 7-4 (11-I)

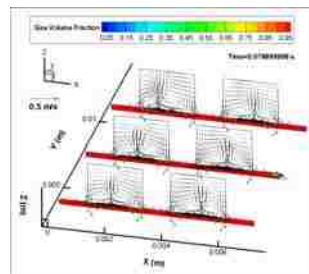


Fig. 7-4 (11-II)

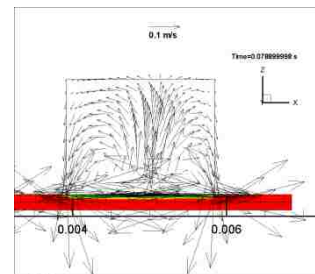


Fig. 7-4 (11-III)

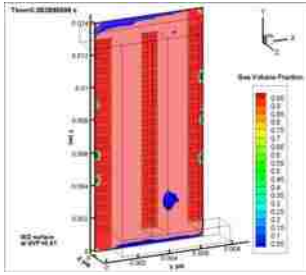


Fig. 7-4 (12-I)

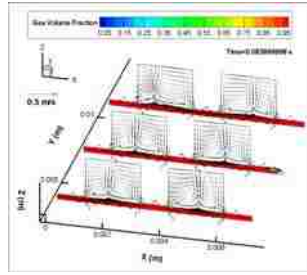


Fig. 7-4 (12-II)

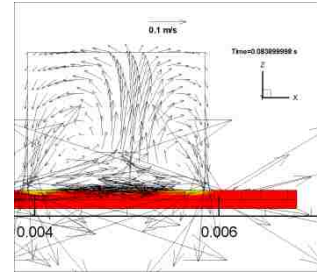


Fig. 7-4 (12-III)

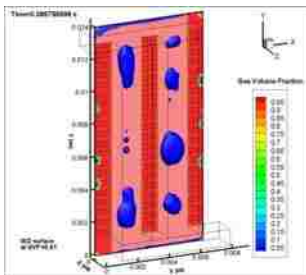


Fig. 7-4 (13-I)

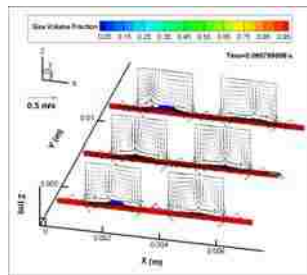


Fig. 7-4 (13-II)

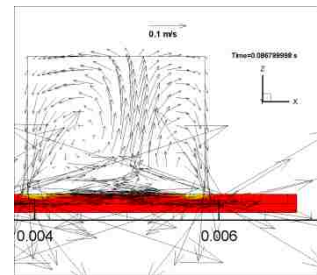


Fig. 7-4 (13-III)

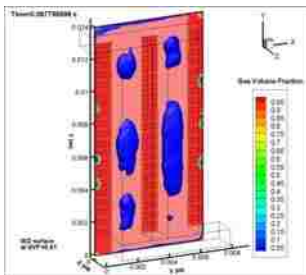


Fig. 7-4 (14-I)

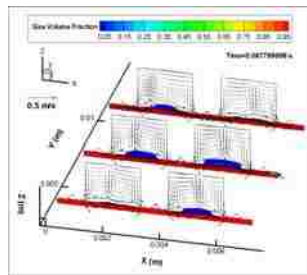


Fig. 7-4 (14-II)

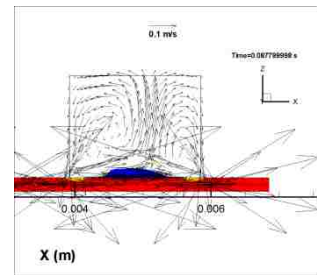


Fig. 7-4 (14-III)

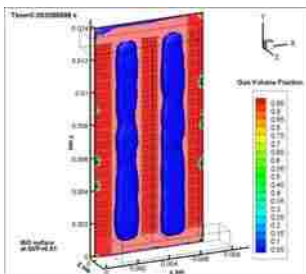


Fig. 7-4 (15-I)

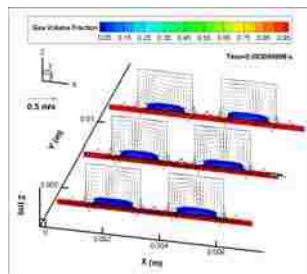


Fig. 7-4 (15-II)

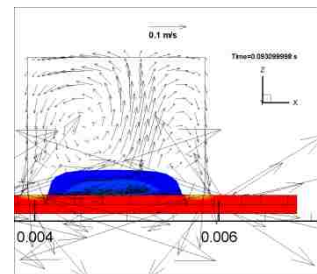


Fig. 7-4 (15-III)

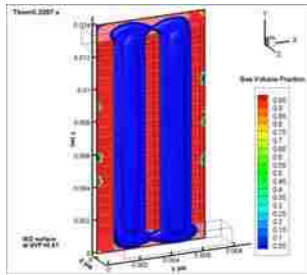


Fig. 7-4 (16-I)

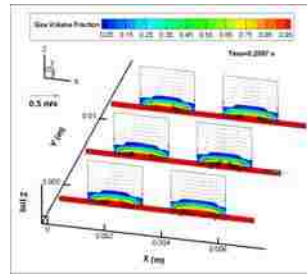


Fig. 7-4 (16-II)

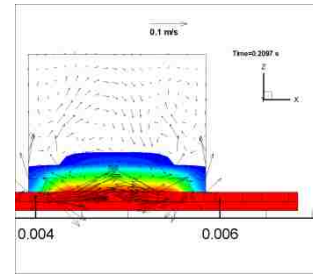


Fig. 7-4 (16-III)

Fig. 7-4 The general process of gas behavior shown with 3D isosurfaces (first column I) and selected cross-section (second column II), and the part of the cross-section has been enlarged to see the vector

As shown in Fig. 7-4 (1–16), CO₂ behaviors in the DMFC anode with a two-channel parallel flow field and the porous layer can be summarized as follows:

(1) CO₂ comes from back of the porous layer with a constant flow rate.

(2) As shown in Fig. 7-4 (1), with gas introduced to the catalyst layer uniformly, the volume fraction of gas diminish along z direction until the time point the gas fulfill the catalyst layer as shown in Fig. 7-4 (2).

(3) Gas emerges into GDL by squeeze into the holes first which forms several small bubbles inside the holes as shown in Fig. 7-4 (3). From the enlarged cross section shown in Fig. 7-4 (d-III), the gas bubbles in the holes tend to dilate by forcing the liquid out of the holes with strong velocities.

(4) The diversity of porosity and the stress from CO₂ follows the rolling of a great wave motion of interface with low volume fraction (volume fraction equal to 0.01) inside the GDL. Near the outlet of anode, three bubbles gathered separately in the GDL and touch the interface between GDL and land as shown in Fig. 7-4 (4-I).

(5) There are three columns holes in the GDL under each channel. The velocity vectors from gas in the holes orientated to the middle of channel.

(6) As shown in Fig. 7-4 (6-III), the gas bubbles in the middle column of holes grow quickly and moving fast toward the channel. Two reversed vortexes shapes on the cross-section. More bubbles formed and touch the interface under the land. And small bubbles float toward channel caused another round of wave.

(7) As shown in Fig. 7-4 (8-I), CO₂ three columns of gas bubbles gathered separately under the land and float around. These bubbles merge and grow bigger but keep in the GDL under land.

(8) The bubbles fulfill the GDL under land and try to squeeze into channel follows the vortexes. However, the stress comes from the liquid in the channel keep pushing them and stop CO₂ grows into channel until the GDL feed to full.

(9) The interface of two phases fluctuates near the interior between channel and GDL and cause strong velocity of two vortexes. Some gas with very low volume fraction float into channel and shakes rapidly.

(10) More bubbles with low volume fraction float into channel and shaking until all of them merged together and form two gas slugs in two channels as shown in Fig. 7-4 (15).

(11) Higher volume fraction gas phase pushing into channels smoothly and moving out from outlet channel.

Since this model assume CO_2 generated constantly, it is not appropriate after the too much CO_2 accumulated. In the operating fuel cell, CO_2 which has not been moved out efficiently will hinder the reaction and thus lower the reaction rate. Therefore, this model runs 0.2097 seconds as shown in last group of figures of Fig. 7-4.

7.4.3 Effect of the gravity

Fig. 7-5 shows the comparison of the specific phenomena of two cases with different gravity orientation at particular time point. In Fig. 7-5 (1), gas bubble inside gas diffusion layer touch the interface between porous layer and channel at similar location (under the land near outlet channel). The similar phenomena are continued until gas diffusion layer is fulfilled. As shown in Fig. 7-5 (3 - 4), the time gas breakthrough the interface and rush into channel in the case shown in right column is much earlier than happening in second column. For the time of the gas reach the outlet channel and released, the case in right column is also in the lead.

To summarize this, the gravity does not give big effect on the gas diffusion from catalyst layer to the gas diffusion layer but play a big role in the process of gas behaviors in the channel. And it is helpful for removing the gas if the gravity orientation is deviated from the outlet.

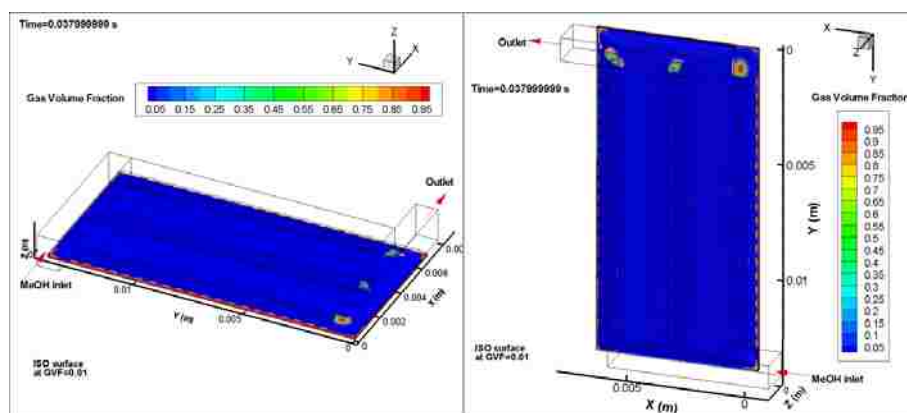


Fig. 7-5 (1) $t = 0.038$ s

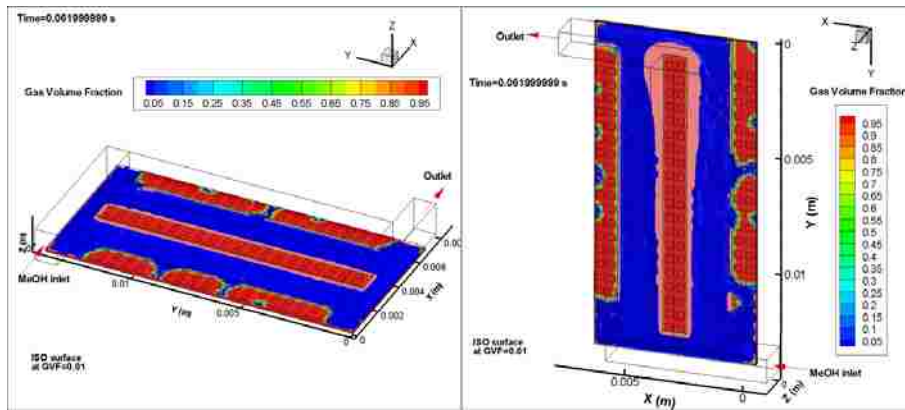


Fig. 7-5 (2) $t = 0.062$ s

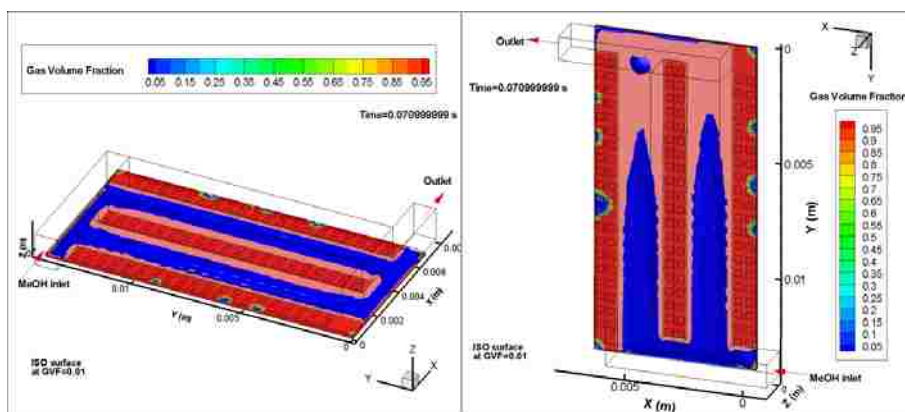


Fig. 7-5 (3) $t = 0.071$ s

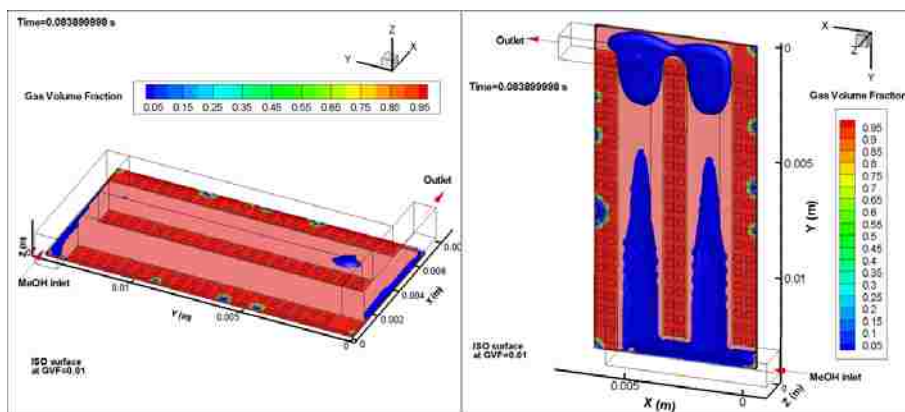


Fig. 7-5 (4) $t = 0.084$ s

Fig. 7-5 Comparison of emerging process of gas in two cases with same boundary condition but different gravity orientation:

Left column: gravity orientate to the direction of negative z axis.

Right column: gravity orientate to the direction of positive y axis.

7.4.4 The CO₂ bubble floating in GDL

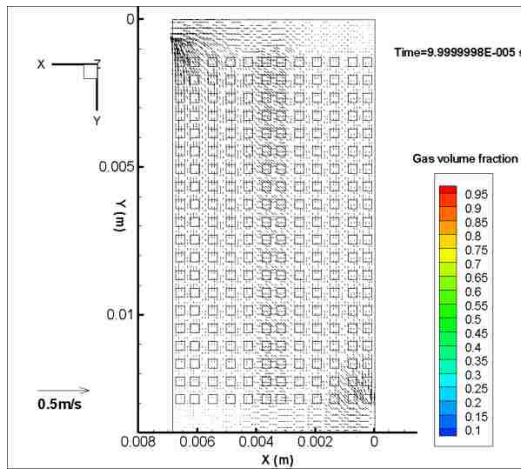


Fig. 7-6 (1)

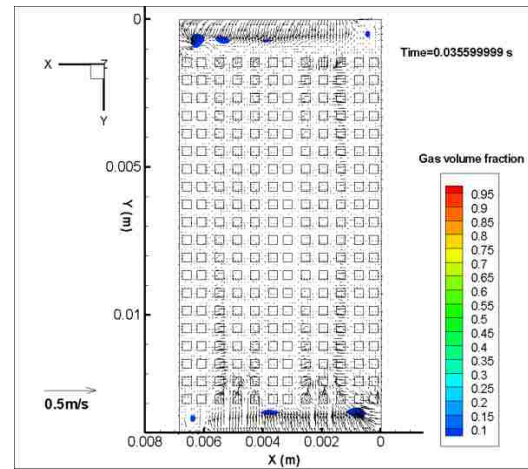


Fig. 7-6 (2)

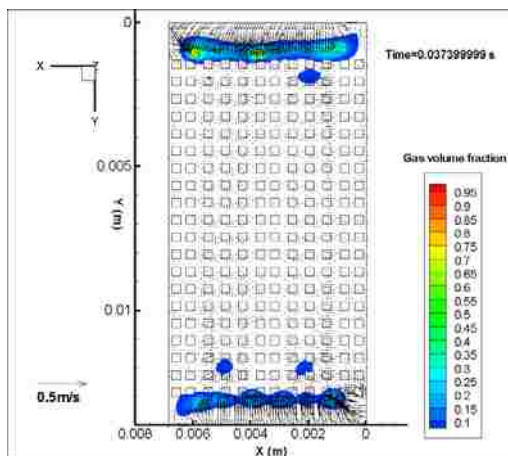


Fig. 7-6 (3)

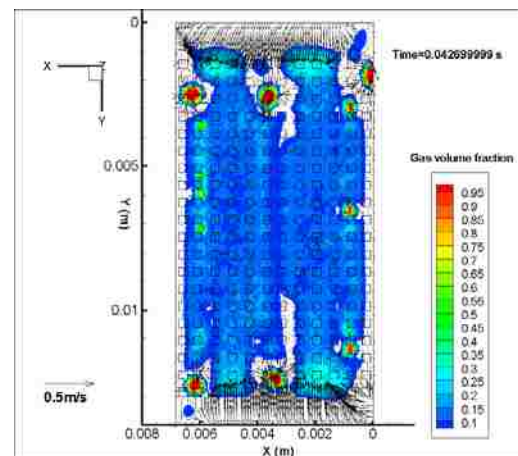


Fig. 7-6 (4)

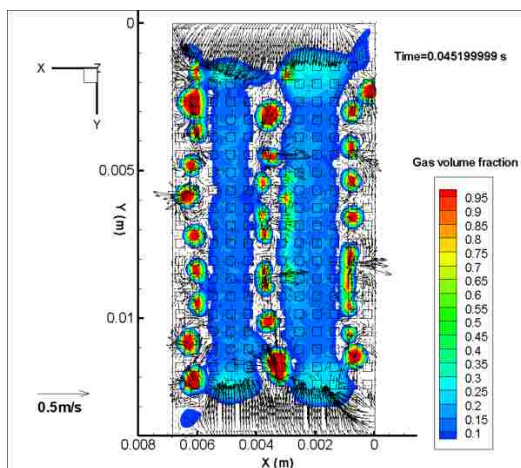


Fig. 7-6 (5)

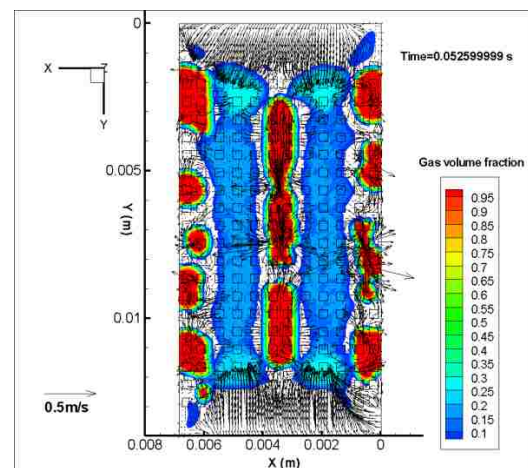


Fig. 7-6 (6)

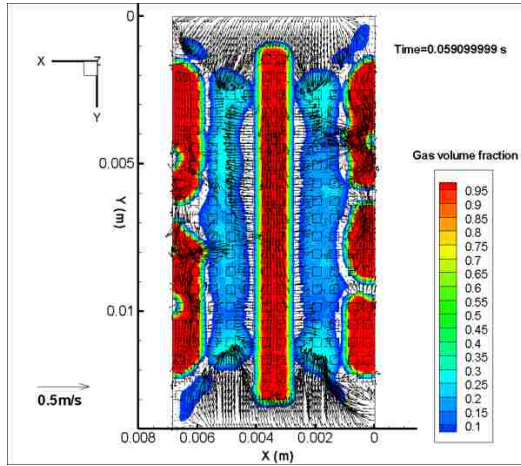


Fig. 7-6 (7)

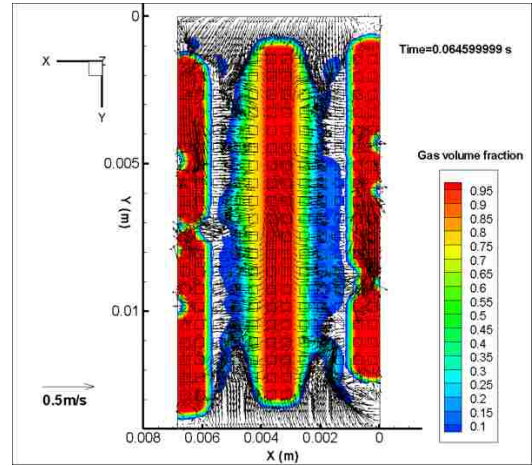


Fig. 7-6 (8)

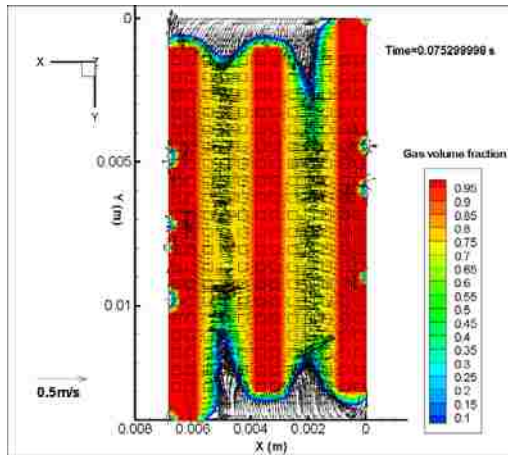


Fig. 7-6 (9)

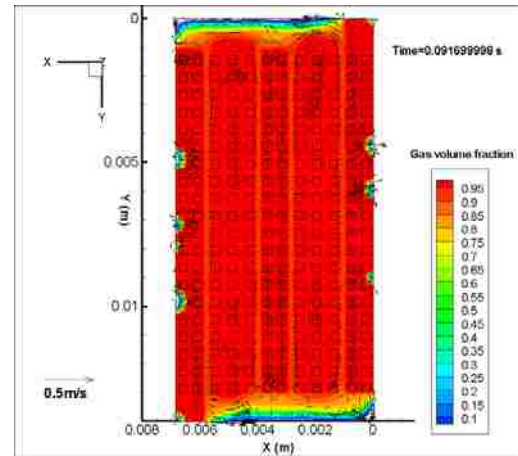


Fig. 7-6 (10)

Fig. 7-6 Gas volume fraction and velocity vector in the selected cross section in the porous layer

Figure 7-6 shows the time evolution of the motion of CO_2 in the anode GDL. The velocity field on the selected cross-section is shown in Fig. 7-6 (1) at the initial status of the simulation. It is noticed that the velocity is faster around the outlet. The walls of the inlet and outlet channel rebound the liquid, trying to move out, and result in higher velocity, pushing the gas bubbles to emerge under the end of the channels as shown in Fig. 7-6 (2). The gas joins together and shapes two gas slugs at the end of the channels, perpendicular to them, as shown in Fig. 7-6 (3). More gas emerges in the selected cross-section with a round shape. The emerging location all concentrates in the area under the land because of the strong flow momentum of the liquid methanol pushing the gas away from the channel.

It is noticed that these bubbles float around inside the GDL because of the uneven porosity and the impact from the liquid flow. With the stress from the liquid, the gas is merged together under the land until it is fulfilled. This results in two ditches on the surface of the gas in the

GDL. As shown in Fig. 7-6 (8 - 9), the gas squeezes from GDL under the middle land into channels. The gas and liquid struggle severe on the interface. After a period of time, more gas coming up fulfills the GDL and keeps this status.

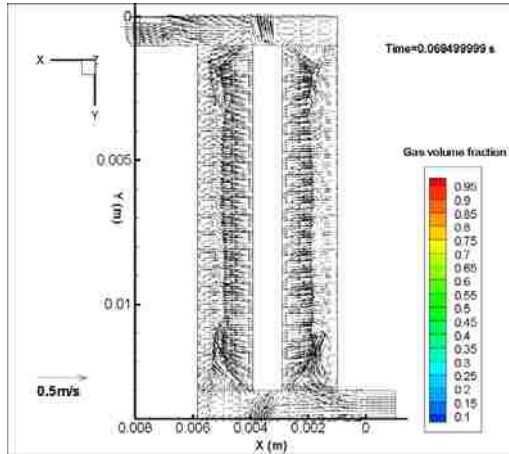


Fig. 7-7 (a)

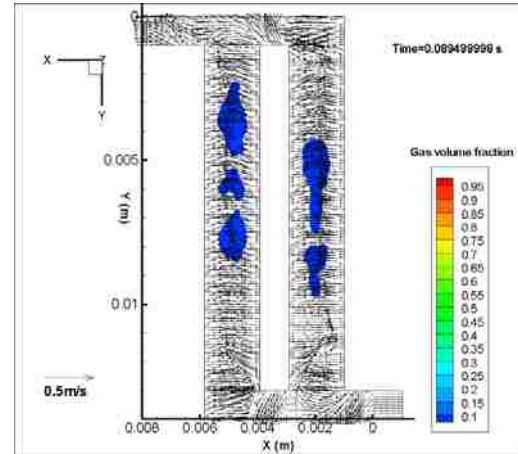


Fig. 7-7 (b)

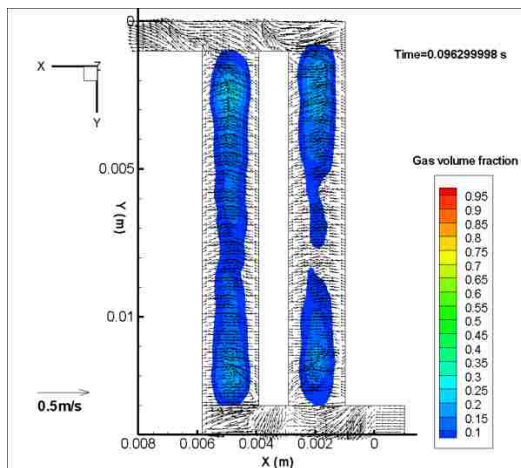


Fig. 7-7 (c)

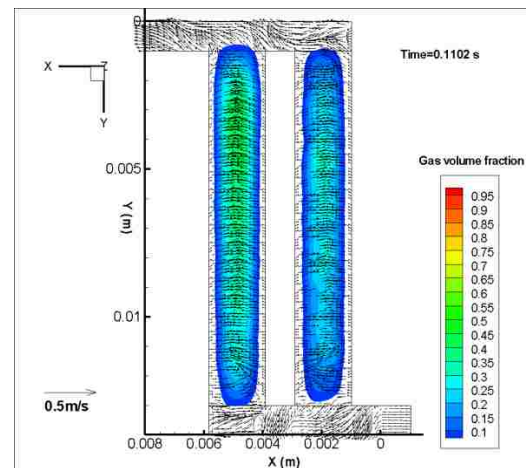


Fig. 7-7 (d)

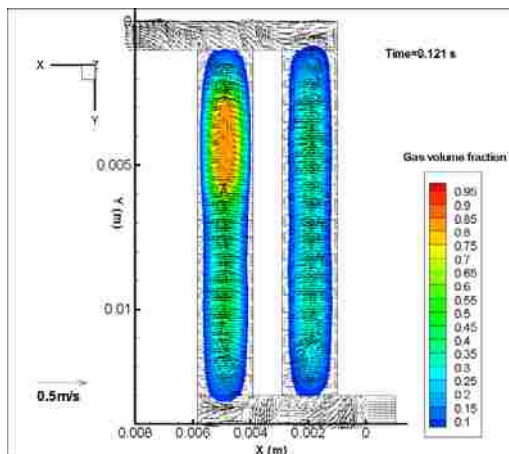


Fig. 7-7 (e)

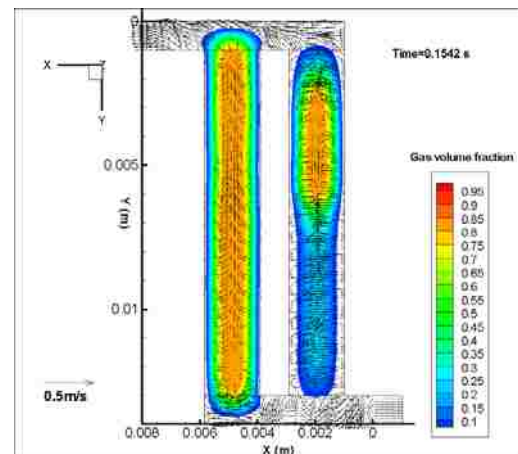


Fig. 7-7 (f)

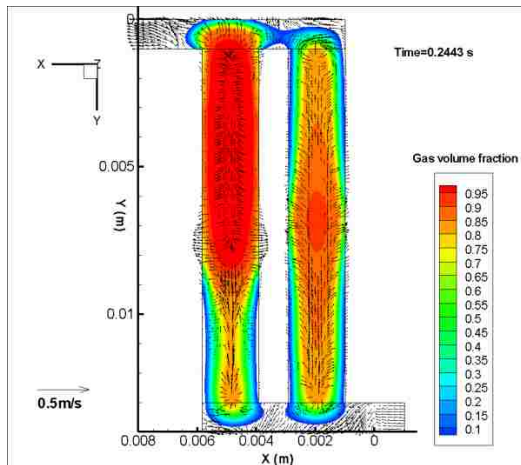


Fig. 7-7 (g)

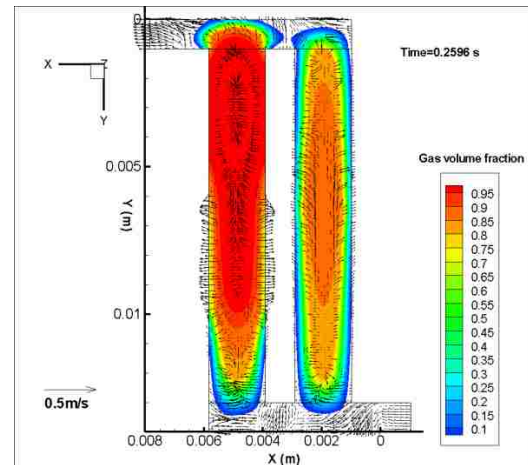


Fig. 7-7 (h)

Fig. 7-7 Gas volume fraction and velocity vector in the selected cross section in the porous layer

7.4.5 The emerging process of CO₂ in channels

Fig. 7-7 shows a series figures of the process of gas showing up in the selected cross-section in the channel which is near the interface between channels and GDL.

(1) Before the gas showing up, the velocity in the channels falls into chaos orient from two sides to the midcourt line.

(2) The first bubble with low volume fraction shows up in the channel near outlet. Although more bubbles with low fraction showing, the velocity field is not affected by the low volume fraction bubbles.

(3) High volume fraction emerging in the same location with the first bubble, especially the half channel near outlet as shown in Fig. 7-7 (e).

(4) This bubble grows longer along the channel while other bubble with high volume fraction shows up in the other channel.

(5) The head of the bubble extend to two sides because of the stress comes from the liquid which resist it grows longer as shown in Fig. 7-7 (g-h).

7.5 Summary

In this chapter, an innovation GDL is adopted without uniform porosity. The results are closer to the experimental visualization although there are still some flaws in the GDL assumptions.

(1) Bubbles generated in GDL under the land and moving around. Similar methanol vortexes in the channel are observed as what discussed in Chapter 6.

(2) The gravity does not give big effect on the gas diffusion from catalyst layer to the gas diffusion layer but play a big role in the process of gas behaviors in the channel. And it is helpful for removing the gas if the gravity orientation is deviated from the outlet.

(3) The CO₂ emerge in GDL in shapes of round bubbles and moving around in it.

(4) The bubbles emerge in the channel with low volume fraction first and shake strongly until gas slug with high volume fraction emerge.

(5) This innovation GDL still needs to improve because the disaccord of the average porosity with practical fuel cells. Improvement will be discuss in next chapter.

Chapter 8 Interface phenomena in DMFC anode with innovative GDL-2 and dynamic contact angle

8.1 Computational domain

In Chapter 7, there is a weakness of the GDL that the porosity is too big with the small paths exist compared with practical GDL in DMFCs. In this chapter, the gas diffusion layer is modified as shown in Fig. 8-1: (1) the number of small paths is reduced; (2) the porosity of other part of gas diffusion layer is decreased. The other properties of computational domain are same with the model in last chapter. The grids sizes do not changed neither.

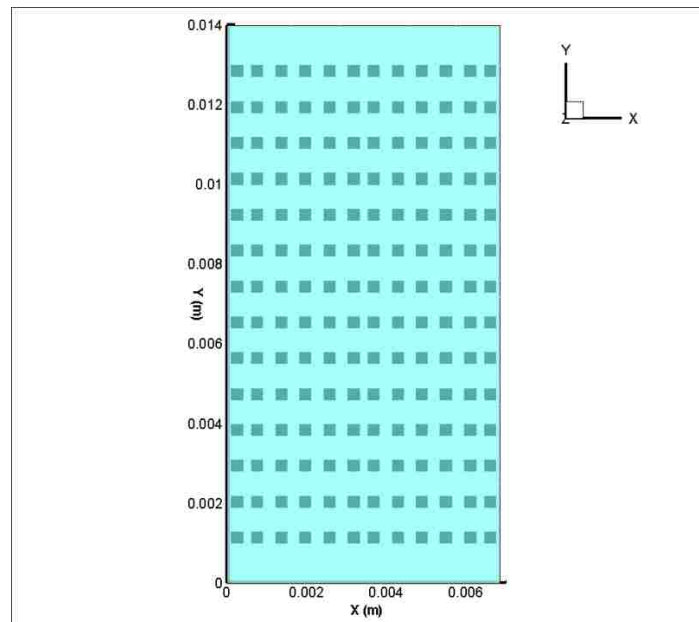


Fig. 8-1 Gas diffusion layer built in this model

8.2 Boundary condition

This model adopts the boundary condition from the experiment study of Liao et al. [58]. The operation temperature is 60°C. Accelerate model is adopt with assume all methanol introduce into the anode has been react and generate CO₂.

Table 8-1 Parameters and properties used in the model

Property	Value
Cell temperature	60 °C
CO ₂ Density	1.6155 kgm ⁻³ [64]
MeOH Density	957.083 kgm ⁻³
CO ₂ viscosity	1.66 × 10 ⁻⁵ Pa·s
MeOH viscosity	0.000454547 Pa·s
Surface tension coefficient	0.06224 Nm ⁻¹
MeOH inlet mass flow rate	0.000106364 kg·s ⁻¹
CO ₂ mass flow rate	3.63994 × 10 ⁻¹⁰ kg·s ⁻¹
Contact angle for the upper wall of channel	Dynamic contact angel with static contact angel of 115°
Contact angle for the side wall of channel	Dynamic contact angel with static contact angel of 115°
Contact angle for the other walls	Dynamic contact angel with static contact angel of 110°

8.3 Methodology of implementation of dynamic contact angle

Dynamic contact angle (DCA) is implemented in this model through the UDF code of FLUENT to the wall boundary conditions, which is developed based on the empirical expressions explored by Kistler [65] shown as followed.

$$\theta_D = f_{Hoff} \left[Ca + f_{Hoff}^{-1}(\theta_e) \right] \quad (17)$$

The dynamic contact angle θ_D is determined by the Hoffmann function f_{Hoff} defined in Equation (17), and varies according to the capillary number Ca and a shift factor $f_{Hoff}^{-1}(\theta_e)$ gained from the inverse of the Hoffmann function under equilibrium when the contact angle on the wall boundary is fixed, namely, static contact angle (SCA) [66].

$$f_{Hoff}(x) = \arccos \left\{ 1 - 2 \tanh \left[5.16 \left(\frac{x}{1 + 1.31x^{0.99}} \right)^{0.706} \right] \right\} \quad (18)$$

The capillary number Ca defined in Equation (18) shows a relationship between viscosity

μ and surface tension σ , affected by the contact line velocity which is extracted instantaneously from the model during iteration.

$$Ca = \frac{(Vel)\mu}{\sigma} \quad (19)$$

In this model, a corrected term $-0.01314932x$ is added to the original Hoffman function to improve the applicability. The revised Hoffman function is expressed as

$$f_{Hoff}^*(x) = \arccos \left\{ 1 - 0.013x - 2 \tanh \left[5.16 \left(\frac{x}{1 + 1.31x^{0.99}} \right)^{0.706} \right] \right\} \quad (20)$$

8.4 Results and discussion

8.4.1 Experiment validation of DMFC anode with a carbon cloth MEA



Fig. 8-2 (1)

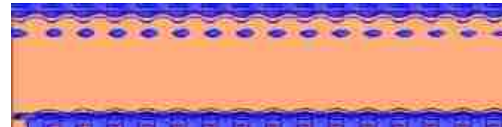


Fig. 8-2 (1)



Fig. 8-2 (2)

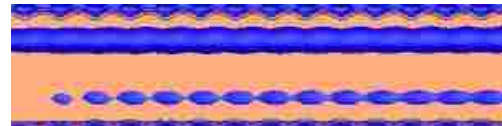


Fig. 8-2 (2)



Fig. 8-2 (3)

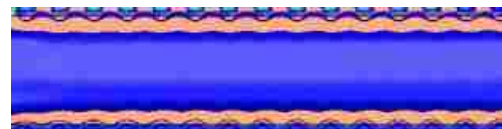


Fig. 8-2 (3)

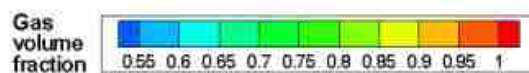


Fig. 8-2 Validation of simulation results with visualization study results of DMFC anode with a parallel design by Liao et al. [58]

This simulation result is validated by the visualization study results of DMFC anode with a parallel design by Liao et al. [58] which chose carbon cloth as GDL. The intersection of fiber bunches of carbon cloth forms orderly pores on GDL, which is similar with the improved GDL structure. As shown in Fig. 8-2, the similar results are observed:

- (1) The small bubbles form on one side of the channel as shown in Fig. 8-2 (1);
- (2) Some of the small bubbles merging together and more forming at the other area of the channel as shown in Fig. 8-2 (2);
- (3) Finally, the channel will fulfilled with a gas slug as shown in Fig. 8-2 (3).

Therefore, the mainly phenomenon of this model is reasonable to discuss the effect from the dynamic contact angle.

8.4.2 CO₂ behavior inside parallel DMFC anode with and without dynamic contact angle effect

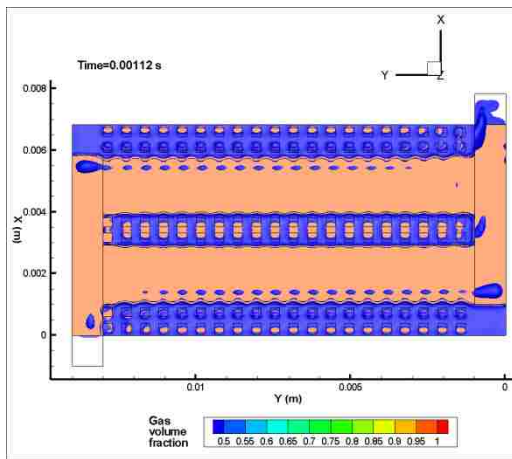


Fig 8-3(1 - SCA)

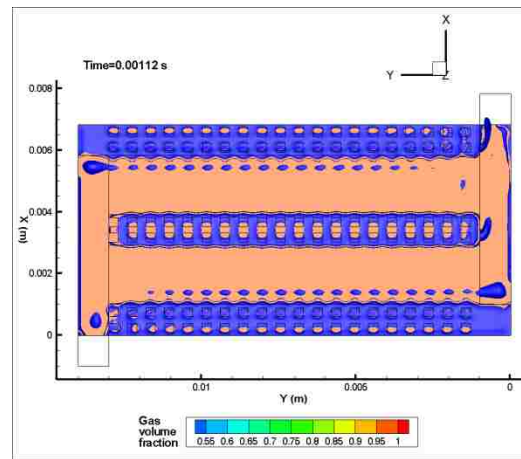


Fig 8-3 (1 - DCA)

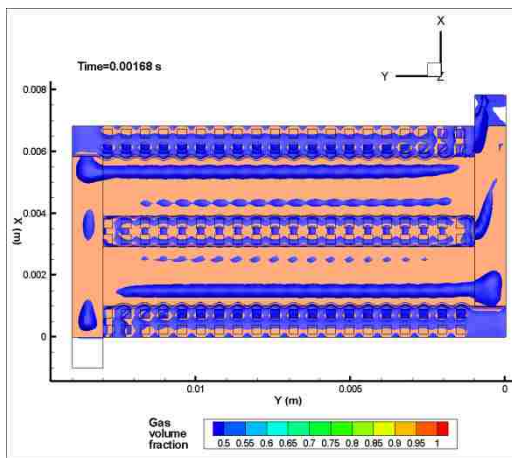


Fig 8-3 (2 - SCA)

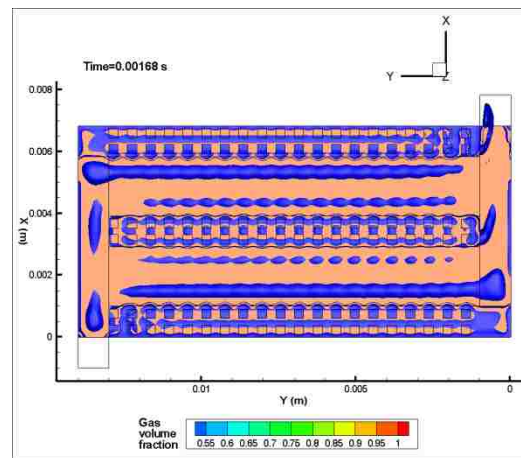


Fig 8-3 (2 - DCA)

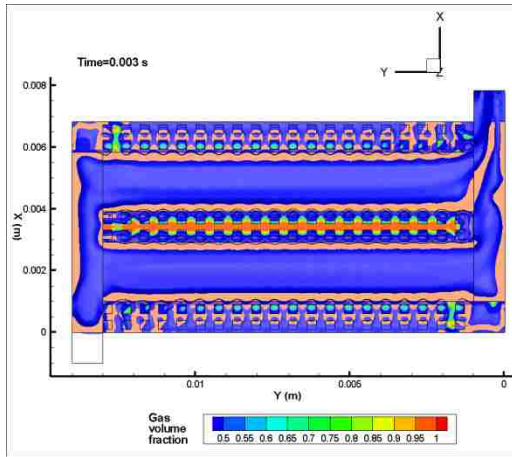


Fig 8-3 (3 - SCA)

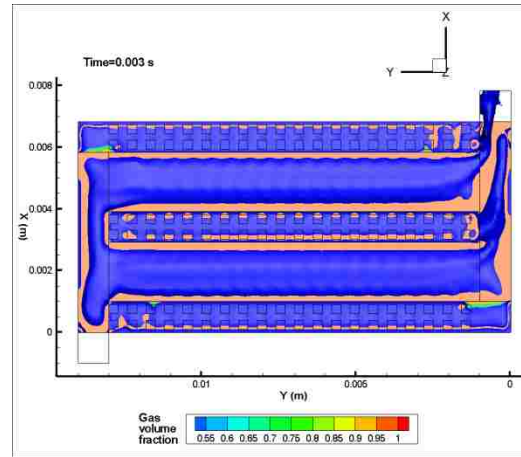


Fig 8-3 (3 - DCA)

Fig. 8-3 General process of gas CO₂ flooding process with and without dynamic contact angle considered

Fig.8-3 (1 - 3) shows three group of comparison of simulation model with dynamic contact angle and static contact angle. The mainly phenomenon of the two cases are similar.

- (1) As shown in Fig.8-3 (1), both the gas bubbles in two cases emerging in the channels in the outskirts side of the channel above the small paths of GDL.
- (2) As shown in Fig.8-3 (2), both the gas bubbles floating out before merge together and the small bubbles emerging in the other side of the channels above the small paths. However, the bubbles in the case with dynamic contact angle are a little bigger than in the other case.
- (3) As shown in Fig.8-3 (3), gas slugs form in the channels in both cases but the gas distribution in the porous layer in two cases are different. To explore the differences, the gas CO₂ distribution in porous layer is discussed in followed sections.

8.4.3 General process of emerging process of gas bubbles behavior in porous layer with static contact angle and dynamic contact angle

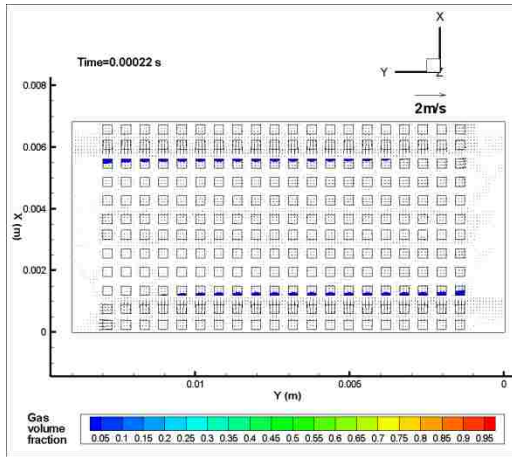


Fig. 8-4 (1 - SCA)

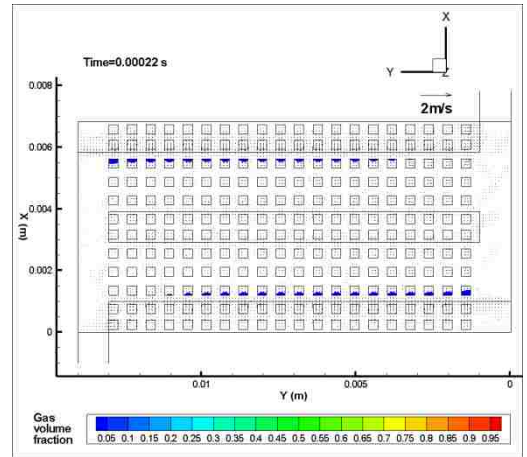


Fig. 8-4 (1 - DCA)

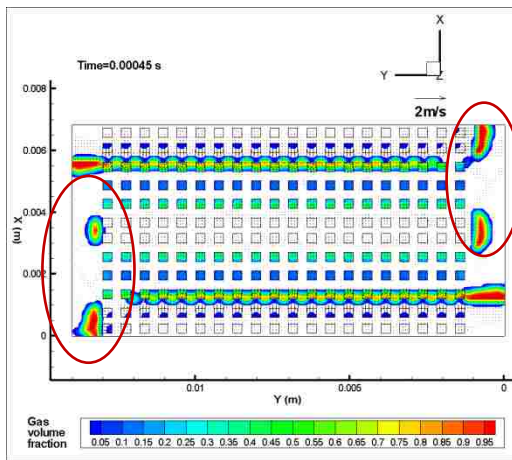


Fig. 8-4 (2 - SCA)

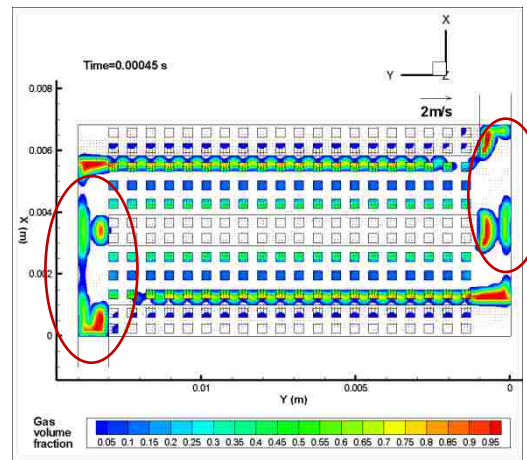


Fig. 8-4 (2 - DCA)

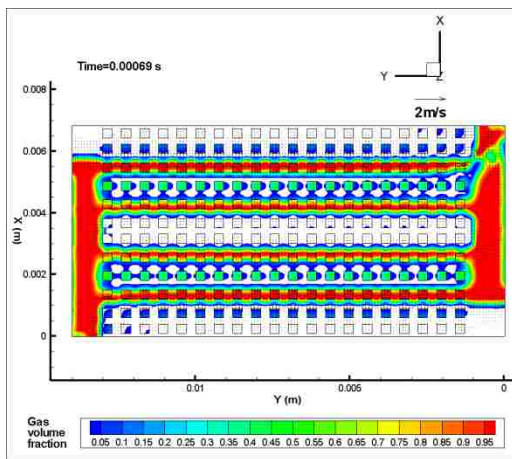


Fig. 8-4 (3 - SCA)

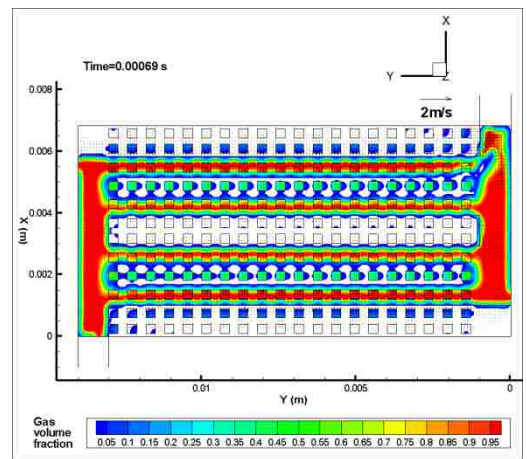


Fig. 8-4 (3 - DCA)

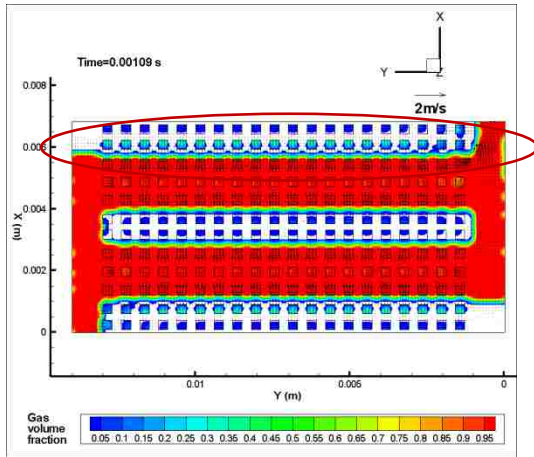


Fig. 8-4 (4 - SCA)

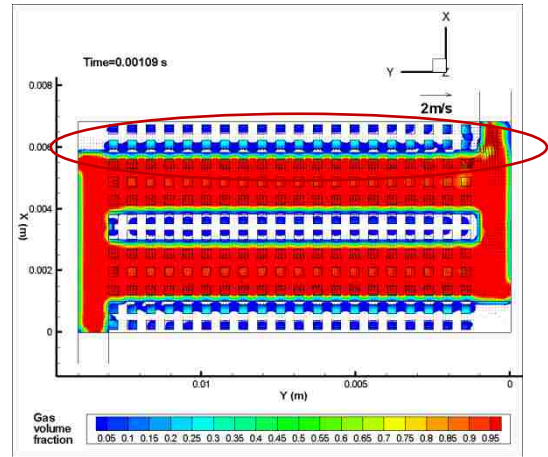


Fig. 8-4 (4 - DCA)

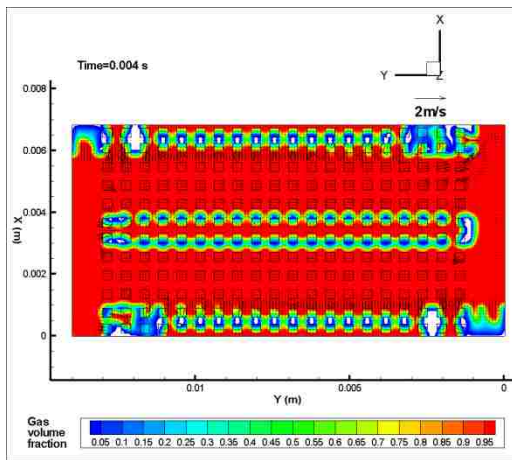


Fig. 8-4 (5 - SCA)

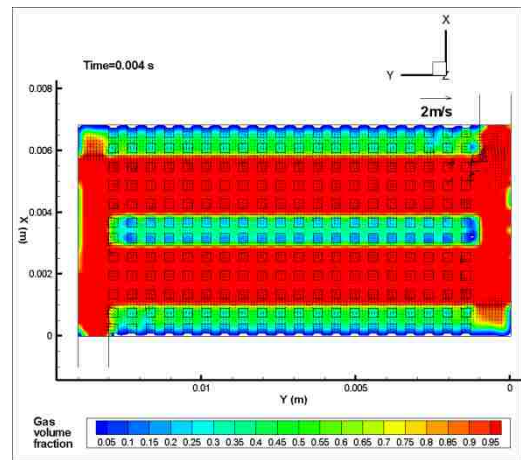


Fig. 8-4 (5 - DCA)

Fig. 8-4 Comparison of emerging process of CO₂ of two cases with static contact angle (left column) and with dynamic contact angle (right column) on cross-section of Z = - 0.00005 m in GDL

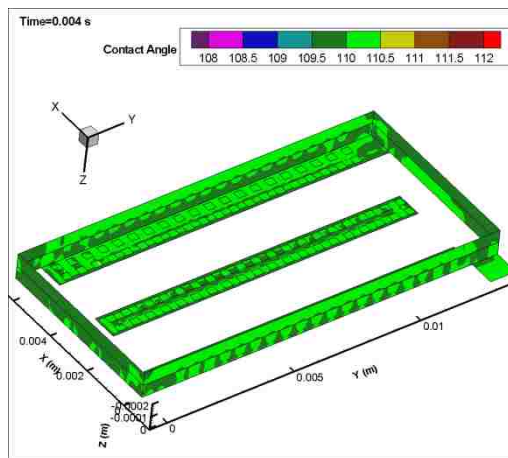


Fig. 8-5 The contact angle of wall around the GDL and CL in the case with DCA

To understand the fundamental processes of both CO₂ and liquid methanol flowing through

the anode with a parallel design with or without consider of dynamic of contact angle, the velocity field and gas volume fraction are shown in Fig. 8-4. The figures in the left column are results from the case with static contact angle, and the right column of figures shows the case with dynamic contact angle considered. The detailed process is presented below:

(1) The gas CO₂ emerges in the selected cross-section in the small paths on GDL under the channel outskirts in both dynamic and static contact angle simulation (Fig. 8-4 (1)).

(2) As shown in Fig. 8-4 (2), more gas CO₂ emerges in the small holes on GDL and most gas accumulate in the holes under the channels outskirts and inlet and outlet channels. The gas distribution in the inlet and outlet channel is different in the case with DCA where more gas emerges.

(3) Gas accumulated and merges in the GDL and forms rules graphics under channels along the walls. The two cases share the same phenomenon except the small area near the outlet as shown in Fig. 8-4 (3).

(4) The gas CO₂ fulfills the GDL under channels and fills the holes at the other area of the GDL. The bubbles inside other area of GDL merge easily in the case with DCA as shown in Fig. 8-4 (4).

(5) After 0.004 s, the gas distribution on the selected cross-section is more smoothly in the case with DCA but forms a series of leak in the case with SCA.

To understand the difference caused by the DCA, the contact angle of the wall around the GDL and CL are shown in Fig. 8-5 where the reference static contact angle of these walls are 110° . As shown in Fig. 8-5, the contact angle range from 109.15° to 111.43° on this instant. The contact angle changes to lower than 110 with the gas CO₂ attaching make the wall accommodate more gas attached. With dynamic velocity field change, the contact angle goes to higher angle in some area near the interface where the wall tends to repel the gas.

8.4.4 CO₂ volume amount inside computational domain

Fig. 8-6 shows the volume amount of CO₂ in each sub-domain of computational domain. The gas CO₂ volume amount in the catalyst layer could be divided to two phases: an accumulation phase and emerging phase. In the accumulation phase, the gas introduced from back surface accumulates in the catalyst layer; the gas amount in the CL is increase linearly; and the volume amount in the paths of GDL increased at later stage of accumulation phase. After a certain period, the gas CO₂ starts to emerge in the channel, which called emerging phase here. Before the emerging phase, the gas amount in channels is almost zero. While in this phase, the value increases approximately linearly in channel one and two. The gas amount in the inlet and outlet channel increase a little but keeps low.

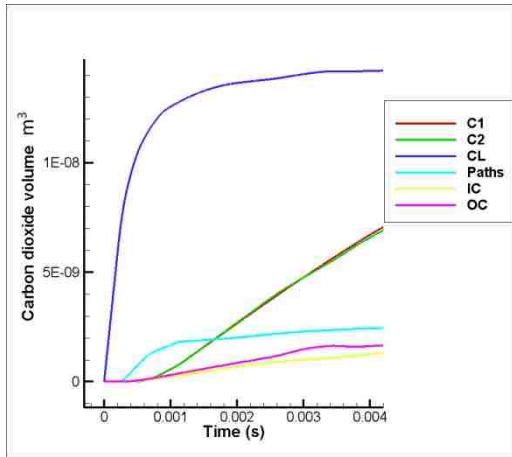


Fig. 8-6 (SCA)

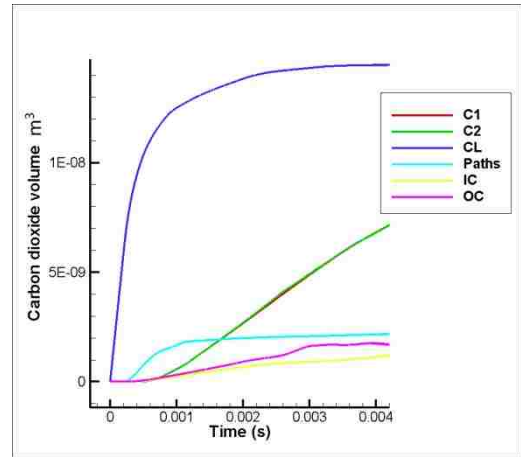


Fig. 8-6 (DCA)

Fig. 8-6 Gas CO₂ volume amount inside each sub-domain

(C1: Channel 1, C2: Channel 2, CL: catalyst layer, IC: inlet channel, OC: outlet channel)

8.4.5 Pressure drop of computational domain

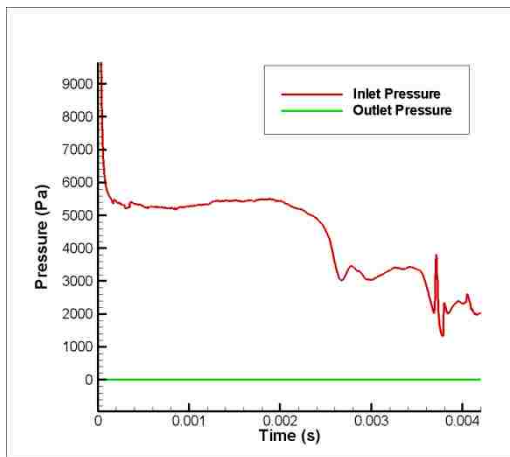


Fig. 8-7 (SCA)

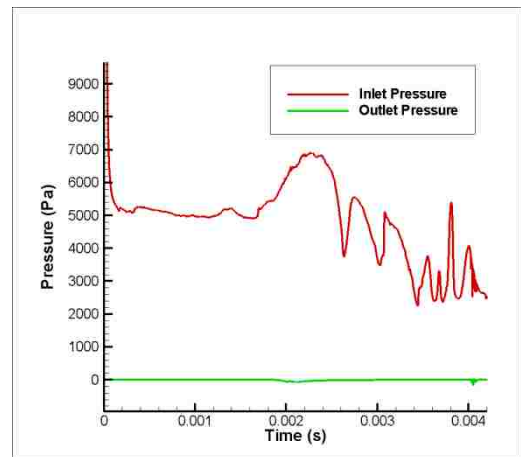


Fig. 8-7 (DCA)

Fig. 8-7 Pressure at Methanol inlet and anode outlet

Fig. 8-7 shows the pressure change curve at the methanol inlet and anode outlet. As introduced before, the pressure at outlet is assumed to keep at atmosphere pressure. Therefore, the outlet pressure curve keeps in 0. The pressure at the methanol inlet varies greatly with sustaining wave. In the case without DCA, the pressure drops from 0.002 s when the gas emerged in the channel covered the interface between channel and porous layer. And almost the same time, the gas CO₂ starts to drain out from the outlet channel. This time point also could find in the case with dynamic contact angle. However, in DCA case, the pressure increase quickly from 1.6 ms and arrive the highest pressure at 2.1 ms. After this instant, the inlet pressure in both cases starts to decrease and Frequently vibration with the droplet drain out process at the outlet channel. During this draining out process, the frequency of fluctuation of pressure curve in the DCA case is more stability than the SCA case.

8.5 Summary

(1) The feature of the liquid water movement in the channel is approximately the same in the experiment result and the numerical result.

(2) The CO₂ emerge in the channel at the peripheral of the channels above the small paths in the GDL in the form as small bubbles. Later, these bubbles merge together and gas flooding happen in the channel.

(3) The results show that the assumption of geometry with small paths in row on GDL is effective to simulate the GDL made with carbon cloth.

(4) The dynamic contact angle will cause difference between simulation results, but do not change the general process of two phase flow phenomena in DMFC anode.

Chapter 9 Conclusions

In the previous chapters Volume of Fluid (VOF) method has been employed to explore PEMFC modeling conducted by software package FLUENT 6.3.26. User defined function (UDF) written by C language is adopted to calculate the pressure and liquid or gas amount. Different geometries and simplified simulation domain designs have been explored. The following conclusions can be drawn from this investigation:

In Chapter 4, a three-dimensional, unsteady, multi-phase numerical modeling of the liquid water flooding process in the flow field of a DHFC cathode with a porous layer is presented. The results indicate that the general liquid water flooding process inside of this type of cathode design can be classified into three phases, and the details of liquid water behavior during this flooding process can be well understood and explained using the air-liquid interaction. Also, a liquid water avalanche phenomenon was discovered in this type of cathode design.

In chapter 5, bubble behavior in a serpentine channel with T-junction break-up procedure is modeled and compared with experiment results in order to validate the VOF algorithm application in DMFC flow field. The results from numerical model and experiment results are similar. Different viscosity and surface tension effect is studied numerically. With increase of viscosity, the bubble slug is become shorter. And with lower surface tension effect, some deformations happened in gas-liquid interface.

In chapter 6, the numerical model is applied to a DMFC anode with parallel design. Some assumptions with regard to accuracy, simplicity and optimal use of computer resources are introduced from DHFC model. The results show that this numerical model is effective to track the gas-liquid distribution in the DMFC anode with parallel design. However, another difficulty emerged in CO₂ bubbles generation process in porous layer for the gas CO₂ with lower density and momentum is impressionable with the porosity distribution in GDL. A successful different simplified numerical model should cater for this diversity.

In Chapter 7 - 8, two different GDLs are developed to approaches to achieve this object, and the results are validated by experimental results. The GDL with small paths (uneven porosity) could better simulate the two phase flow phenomena in DMFC anode. Besides, effects of dynamic contact angle are considered in Chapter 8. There are some differences between cases with static contact angle and with dynamic contact angle but the general processes are similar.

References

- [1] O'Hayre R, Cha SW, Colella W, Prinz F. Fuel cell fundamentals. Hoboken, NJ Wiley; 2005.
- [2] Matthew. M. Mench, Fuel Cell Engines, John Willey & Sons, 2008.
- [3] W Yang, Mathematical modeling of two-phase mass transport in liquid-feed direct methanol fuel cells, Doctoral dissertation, The Hong Kong University of Science and Technology, 2010.
- [4] I. S. Hussaini, Experimental study of transient dynamics of PEM Fuel Cells, Doctoral dissertation, The Pennsylvania State University.
- [5] X. Li, Imran Sabir. Review of bipolar plates in PEM fuel cells: Flow-field designs. *Hydrogen Energy* 30 (2005) 359-371.
- [6] H. Yang, T.S. Zhao, Q. Ye, In situ visualization study of CO₂ gas bubble behavior in DMFC anode flow fields, *J. Power Sources* 139 (2005) P 79–90
- [7] Y. Yang and Y. Liang, A Consise Two-phase Flow Model for Direct Methanol Fuel Cell Performance Modeling, IEEE PEDS, 2005
- [8] F. Liu, G. Lu, and C. Y. Wang, Low Crossover of Methanol and Water Through Thin Membranes in Direct Methanol Fuel Cells, *J. Electrochemical Society*, 153, 3, A543-A553, 2006
- [9] S. Matar and H. Liu, Effect of cathode catalyst layer thickness on methanol cross-over in a DMFC, *Electrochimica Acta* Vol.56, Issue 1, 15 Dec 2010, P 600-606
- [10] R. Chen, T. S. Zhao, Mathematical modeling of a passive-feed DMFC with heat transfer effect, *J. Power Sources* 152 (2005) 122-130
- [11] P. Alotto, M. Guarnieri, and F. Moro, Optimal design of micro direct methanol fuel cells for Low-Power Applications, *IEEE Transactions on Magnetics*, Vol.45, NO. 3, Mar 2009
- [12] H. Bahrami, A. Faghri, Water Management in a Passive DMFC Using Highly Concentrated Methanol Solution, *J. Fuel Cell Science and Technology* Apr 2011, Vol.8, 021011-1
- [13] Y. Tian, Go. Sun, Q. Mao, S. Wang, H. Liu, Q. Xin, In situ analysis on water transport in a direct methanol fuel cell durability test, *Journal of Power Sources* 185 (2008) 1015-1021
- [14] J. Yi, T. V. Nguyen. An along-the-channel model for proton exchange membrane fuel cells. *J. Electrochem. Soc.*, 145 (1998) Issue 4, P1149-1159.
- [15] A. Kazim, H. T. Liu and P. Forges. Modelling of performance of PEM fuel cells with conventional and interdigitated flow fields. *J. Applied Electrochemistry* 29, 1409 (1999).
- [16] C. Marr, X. Li. Composition and performance modeling of catalyst layer in a proton exchange membrane fuel cell. *J. Power Sources* 77, 17 (1999).
- [17] S. Shimpalee, S. Dutta, W. K. Lee, J.W. Van Zee. Effect of humidity on PEM fuel cell performance part II – numerical simulation. Proceedings of ASME IMECE, Nashville, TN,

HTD 364-1(1999) 367-374.

[18] Z. H. Wang, C. Y. Wang, K. S. Chen. Two-phase flow and transport in the air cathode of proton exchange membrane fuel cells. *J. Power Sources* 94 (2001) 40-50.

[19] E. Hontanon, M. J. Escudero, C. Bautista, P. L. Garcia-Ybarra, L. Daza. Permeability and flow-field configuration: influence on the performance of a PEMFC. *J. Power Sources* 86 (2000) 363.

[20] P. T. Nguyen, T. Berning and N. Djilali. Computational model of a PEM fuel cell with serpentine gas flow channels. *J Power Sources* 130 No. 1-2 (2004) 149-157.

[21] J. S. Yi, T. V. Nguyen. Multi-component transfer in porous electrodes of proton exchange membrane fuel cells using the interdigitated gas distributors. *J. Electrochem. Soc.* 146, (1999) 38.

[22] L. You, H. Liu. A two-phase flow and transport model for the cathode of PEM fuel cells. *J. Heat Mass Transfer* 45 (2002) 2277-2287.

[23] S. Um, C. Y. Wang, and K.S. Chen. Computational fluid dynamics modeling of proton exchange membrane fuel cells. *J. Electrochemical Society*, 147(12) (2000) 4485-4493.

[24] S. W. Cha, R. O'Hayre, S. J. Lee, Y. Saito, F. B. Prinz. The scaling behavior of flow patterns: a model investigation. *J. Power Sources* 134 (1) (2004) 57.

[25] I. S. Hussaini, C. Y. Wang, Measurement of relative permeability of fuel cell diffusion media. *J. Power Sources* 195 (2010) 3830-3840.

[26] X. Zhu, P. C. Sui, and N. Djilali, Dynamic behavior of liquid water emerging from a GDL pore into a PEMFC gas flow channel. *J. Power Sources* 172 (1), pp. 287-295 (2007).

[27] J. G. Pharoah, K. Karan, and W. Sun, On effective transport coefficients in PEM fuel cell electrodes: Anisotropy of the porous transport layers. *J. Power Sources*, 161 (2006) 214-224

[28] X. Zhang, D. T. Song, Q. P. Wang, C. Huang, and Z. S. Liu, Influence of anisotropic transport properties of the GDL on the performance of PEMFCs. *ECS Transactions*, 16 (2) (2008) 913-923

[29] P. P. Mukherjee, C. Y. Wang, and Q. Kang, Mesoscopic Modeling of Two-phase Behavior and Flooding Phenomena in Polymer Electrolyte Fuel Cells, *Electrochimica Acta*, 54 (2009) 6861-6875.

[30] K. Jiao, B. Zhou, and P. Quan, Liquid water transport in straight micro parallel channels with manifolds for PEM fuel cell cathode. *J. Power Sources* 157 (2006), 226-243.

[31] K. Jiao, B. Zhou. Effects of electrode wettabilities on liquid water behaviors in PEM fuel cell cathode. *J. Power Sources* 175 (2008) 106-119.

[32] P. Quan, B. Zhou, A. Sobiesiak, Z. Liu. Water behavior in serpentine micro-channel for proton exchange membrane fuel cell cathode. *J. Power Sources* 152 (2005) 131-145.

[33] Anh D Le, Biao Zhou. Fundamental understanding of liquid water effects on the performance of a PEMFC with serpentine-parallel channels. *Electrochimica Acta* 54 (2009) P 2137-2154.

- [34] A. D. Le, B. Zhou, H. R. Shiub, C. I. Leeb, W.C. Chang. Numerical simulation and experimental validation of liquid water behaviors in a proton exchange membrane fuel cell cathode with serpentine channels. *J. Power Sources* 195 (2010) P 7302-7315.
- [35] K. Jiao, B. Zhou. Accelerated numerical test of liquid behavior across gas diffusion layer in proton exchange membrane fuel cell cathode. *J. Fuel Cell Science and Technology* 5(2008) 041011.
- [36] N. Mendez-Sanchez, T. J. Cutright, and P. Qiao. Accelerated weathering and biodegradation of E-glass polyester composites. *Int. Biodeter. Biodegrad.* 54 (2004) P 289–296.
- [37] M. J. LuValle. An approximate kinetic theory for accelerated testing. *IIE Trans.*, 31(1999) P 1147-1156.
- [38] R. T. Magari. Estimating degradation in real time and accelerated stability tests with random Lot-to-Lot variation: A simulation study. *J. Pharm. Sci.* 91[3] (2002) P 893-899.
- [39] H. Shyur, E. A. Elsayed, and J. T. Luxhoj, Naval Res. A general model for accelerated life testing with time-dependent covariates. *Logistics Quart* 46 (1999) 303-321.
- [40] H. Shyur, E. A. Elsayed, and J. T. Luxhoj, A general hazard regression model for accelerated life test. *Ann. Operat. Res.* 91 (1999) P 263-280.
- [41] M. Hicks, R. Atanasoski, Presentation. 3M MEA durability under accelerated testing. *Fuel Cells Durability Conference*, Washington, DC, Dec. 8 - 9. (2005).
- [42] G. Q. Lu, C. Y. Wang, Electrochemical and flow Characterization of a direct methanol fuel cell, *Journal of Power Sources* 134 (2004) P 33–40
- [43] C. W. Wong, T. S. Zhao, Q. Ye, and J. G. Liu, Transient Capillary Blocking in the Flow Field of a Micro-DMFC and Its Effect on Cell Performance, *Journal of The Electrochemical Society*, 152 (8) A1600-A1605 (2005)
- [44] A. A. Kulikovsky, Model of the flow with bubbles in the anode channel and performance of a direct methanol fuel cell, *Electrochemistry Communications* 7 (2005) 237-243
- [45] A. A. Kulikovsky, Bubbles in the anode channel and performance of a DMFC: Asymptotic solutions, *Electrochimica Acta* 51 (2006) 2003-2011
- [46] Z. H. Wang and C. Y. Wang, Mathematical modeling of liquid-feed direct methanol fuel cells, *J. Electrochemical Society*, 150 (4) A508-A519 (2003)
- [47] J. Ge, H. T. Liu, A three-dimensional two-phase flow model for a liquid-fed direct methanol fuel cell, *J. Power Sources* 163 (2007) P 907-915
- [48] K. Fei, T. S. Chen, C. W. Hong, Direct methanol fuel cell bubble transport simulations via thermal lattice Boltzmann and volume of fluid methods *J. Power Sources* 195 (2010) 1940-1945
- [49] K. Jiao, B. Zhou, Innovative gas diffusion layers and their water removal characteristics in PEM fuel cell cathode, *J. Power Sources* 169 (2007) 296-314
- [50] K. Tuber, D. Pocza, C. Hebling, Visualization of water buildup in the cathode of a

transparent PEM fuel cell, *J. Power Sources* 124 (2003) 403-414.

[51] S. Ge, C. Y. Wang, Cyclic voltammetry study of ice formation in the PEFC catalyst layer during cold start, *J. Electrochemical Society* 154 (10) (2007) B998-B1005

[52] T. A. Trabold, J. P. Owejan, D. L. Jacobson, M. Arif, P. R. Huffman, In situ investigation of water transport in an operating PEM fuel cell using neutron radiography: Part 1-Experimental method and serpentine flow field results *International. J. Heat and Mass Transfer* 49 (2006) 4712-4720.

[53] D. Spornjak, A. K. Prasad, S. G. Advani, In situ comparison of water content and dynamics in parallel, single-serpentine, and interdigitated flow fields of polymer electrolyte membrane fuel cells, *J. Power Sources* 195 (2010) 3553-3568.

[54] S. Tsushima, K. Teranishi, S. Hirai, Magnetic resonance imaging of the water distribution within a polymer electrolyte membrane in fuel cells, *Electrochemical and Solid-State Letters* 7 (2004) A269-A272.

[55] W. M. Yan, S. C. Mei, C. Y. Soong, Z. S. Liu, D. Song, Experimental study on the performance of PEM fuel cells with interdigitated flow channels. *J. Power Sources*, 160 (2006) 116

[56] B. R. Fu, C. Pan, Bubble growth with chemical reactions in microchannels, *International Journal of Heat and Mass Transfer* 52 (2009) 767-776

[57] R. Xiong, J. N. Chung, Bubble generation and transport in a microfluidic device with high aspect ratio, *Experimental Thermal and Fluid Science* 33 (2009) 1156-1162

[58] Q. Liao, X. Zhu, X. Zheng, Y. Ding, Visualization study on the dynamics of CO₂ bubbles in anode channels and performance of a DMFC, *J. Power Sources* 171 (2007) 644-651

[59] H. Yang, T. S. Zhao, Q. Ye, In situ visualization study of CO₂ gas bubble behavior in DMFC anode flow fields, *J. Power Sources* 139 (2005) 79-90

[60] *Fluent 6.3 Manual*, Fluent Inc. (2006).

[61] D. B. Kothe, W. J. Rider, S. J. Mosso, J. S. Brock, J. I. Hochstein, Volume tracking of interfaces having surface tension in two and three dimensions, *AIAA* 96-0859.

[62] S Kang, B Zhou, C Cheng, H Shiu, C Lee, Liquid water flooding in a proton exchange membrane fuel cell cathode with an interdigitated design, *Int. J. Energy Res.* (2011), DOI: 10.1002/er.1858

[63] Wikipedia, http://en.wikipedia.org/wiki/Surface_tension

[64] <http://www.peacesoftware.de/einigewerte/co2.html>

[65] S. F. Kistler, Hydrodynamics of wetting, in *Wettability*, edited by J. C. Berg (Marcel Dekker, New York, 1993) p. 311.

[66] S. Sikalo, H. D. Wilhelm, I.V. Roisman, S. Jakirlic, and C. Tropea, Dynamic contact angle of spreading droplets: Experiments and simulations, *Physics of Fluids* 17-062103 (2005) p. 1-13.

VITA AUCTORIS

Simo Kang was born in 1985 in Liaoning, China. She graduated from Dalian University of Technology in 2009 with double degrees of Bachelor of Science in Mechanical Engineering and Bachelor of Commerce in International Economics and Trade. Since 2009 she is pursuing a M.A.Sc degree in Mechanical Engineering at the University of Windsor and hopes to graduate in Summer 2011.